Childhood to Adolescence: Dust and Gas Clearing in Protoplanetary Disks

Thesis by

Joanna M. Brown

In Partial Fulfillment of the Requirements

for the Degree of

Doctor of Philosophy

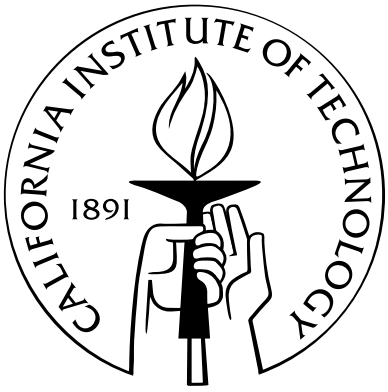

California Institute of Technology

Pasadena, California

2007

(Defended November 19, 2007)

To my parents, for always supporting me, and to my brother, as he begins his graduate school adventures

Acknowledgements

Many people have contributed to this thesis. I would like to thank the following people:

- My advisor, Geoff Blake, for his enthusiasm and for encouraging me to explore new ideas throughout grad school.
- The c2d team, particularly the IRS portion, for helpful scientific discussion and enjoyable meetings. Getting to know all of you has been one of the highlights of graduate school. In particular, I'd like to thank Kees Dullemond for the use of his model and patiently explaining how to use it. Also, Jackie Kessler-Silacci provided me with a gentle introduction to graduate school and remained helpful throughout.
- Anneila Sargent and Ewine van Dishoeck for leading by example and showing how successful women can be in astronomy. Also, a big thank you to Ewine for many edits of the paper which became Chapter 2 and providing the impetus to actually finish it.
- Stuartt Corder for long discussions about data analysis and going on observing runs to the CSO, even when he didn't want to.
- Other members of the Blake group, particularly Colette Salyk, Adwin Boogert and Klaus Pontoppidan, for helpful collaboration and Colette and Adwin for maintaining the NIRSPEC M-band spectral database.
- Charlie Qi for being my 'inside man' at the SMA.
- The observatory staff at CARMA, Keck, the SMA, and the CSO, who made collecting the data for this thesis possible. Also, my fellow CARMA observers who made going to Cedar Flat fun.
- CARMA and the Spitzer c2d Legacy Project for funding this work.
- My roommate, Liz Ottesen, whose life has meshed with mine for the last five and a half years. Little did we know that a random assignment by the housing office would work out so incredibly well.
- My family for always supporting me. My father who patiently listened as I wrote this thesis and throughout graduate school, my mother for keeping me connected to a life outside of astronomy, and my brother for understanding that there is a time and place for distractions.

Abstract

Disks are ubiquitous around young stars. Over time, disks dissipate, revealing planets that formed hidden by their natal dust. Since direct detection of young planets at small orbital radii is currently impossible, other tracers of planet formation must be found. One sign of disk evolution, potentially linked to planet formation, is the opening of a gap or inner hole in the disk. In this thesis, I have identified and characterized several cold disks with large inner gaps but retaining massive primordial outer disks. While cold disks are not common, with $\sim$5% of disks showing signs of inner gaps, they provide proof that at least some disks evolve from the inside-out. These large gaps are equivalent to dust clearing from inside the Earth's orbit to Neptune's orbit or even the inner Kuiper belt. Unlike more evolved systems like our own, the central star is often still accreting and a large outer disk remains.

I identified four cold disks in Spitzer 5-40 μm spectra and modeled these disks using a 2-D radiative transfer code to determine the gap properties. Outer gap radii of 20-45 AU were derived. However, spectrophotometric identification is indirect and model-dependent. To validate this interpretation, I observed three disks with a submillimeter interferometer and obtained the first direct images of the central holes. The images agree well with the gap sizes derived from the spectrophotometry. One system, LkHα 330, has a very steep outer gap edge which seems more consistent with gravitational perturbation rather than gradual processes, such as grain growth and settling. Roughly 70% of cold disks show CO v=1$\rightarrow$0 gas emission from the inner 1 AU and therefore are unlikely to have evolved due to photoevaporation. The derived rotation temperatures are significantly lower for the cold disks than disks without gaps. Unresolved (sub)millimeter photometry shows that cold disks have steeper colors, indicating that they are optically thin at these wavelengths, unlike their classical T Tauri star counterparts. The gaps are cleared of most $\sim$100 μm sized grains as well as the $\sim$10 μm sized grains visible in the mid-infrared as silicate emission features.

Contents

List of Figures

List of Tables

Chapter 1

Introduction

Circumstellar disks around pre-main sequence stars are known to be the birth sites of planets. In the earliest stages of star formation, dense molecular clouds collapse via their own gravity, most likely against the support provided by magnetic fields, forming protostellar cores. The initial dust enshrouded protostellar cores continue to contract and flatten into disks in order to conserve angular momentum. The phase with which this thesis is particularly concerned is toward the end of the star formation process – the dissipation of these disks before the stars reach the main sequence, when planetary systems may first be revealed. Direct detection of young planets that orbit close to their parent stars, such as those found by radial velocity surveys, seems unlikely at this time due to observational difficulties caused by obscuring dust and small spatial scales. Therefore, planetary formation processes remain largely unconstrained by observation. Properties of the more easily observable circumstellar disks must be studied to determine the protoplanetary environment and constrain formation scenarios of planets.

Dust in protoplanetary disks causes excess emission above that expected from the stellar photosphere at near-IR to mm-wavelengths (see Figure 1.1b). The physical conditions in these young disks are comparable to those inferred for the early stages of our own solar system, with sizes of tens to hundreds of astronical units (AU; i.e., the distance between the Sun and the Earth) and masses of $\lesssim 0.1 M_{\odot}$ (Beckwith 1996, Mundy et al. 2000). At the other end of the expected evolutionary sequence are less massive debris disks, which are older and exhibit weaker infrared (IR) excess emission that is thought to arise from grains generated by the collisions of planetesimals after the primordial dust has coagulated or dissipated (Aumann et al. 1984, Rieke et al. 2005), and most likely after the original gas content of the disk has been significantly depleted. Less is understood about how disks transition from the birth of planets to the violent adolescence of debris disks.

Significant evolution in proto-planetary bodies must occur in the transition stage between opti-

cally thick circumstellar disks and the tenuous debris disks. Knowledge of how disks dissipate is thus vital for our understanding of planetary system evolution. Studies have shown that the dissipation timescale for large ensembles of disks from a variety of young star clusters extends to some 3-10 Myr, but that the transition phase for any individual disk must be a small fraction of the overall lifetime (Hillenbrand 2006, Bertout et al. 2007) – making the identification of a sample of this important, short-lived phase difficult. One indicator of intermediate systems is the presence of an inner hole or gap, suggesting that the inner disk has evolved while the outer disk has not. The presence of gaps may indicate that planets have already formed in the disks and cleared the material around their orbits. Such systems can therefore strongly constrain models of planet formation, especially the role of gap formation and disk-planet interactions in various planet migration scenarios that lead to the creation of "hot Jupiters" found to orbit much older systems (Marcy et al., 2005).

Transitional disks therefore provide the possibility of directly observing how disks dissipate and the effects of this dissipation on planet formation. Classical T Tauri (CTTs) star disks, which retain a large amount of dust and gas, are too optically thick to detect the protoplanets in their midst. At the other extreme, systems cleared of their dust and gas contain already formed planets, and it is too late to study the nascent phase. Transitional disks, where dust clearing has begun, are systems which balance the requirements of observability and youth, but few are known at present. The method of dust dissipation (e.g. dust dissipation at equal rates throughout the disk vs. accelerated growth and dissipation in the inner disk region) has implications for viable scenarios of planet formation at different disk radii. It is easier to trace dust dissipation through SED fitting than gas dissipation where different species and temperatures must be observed in many different spectral lines. However, the dust is not the main component of the disk, and it is not clear how tightly gas and dust evolution is coupled. Thus, gas dissipation must be considered as a separate, although closely related, problem of equal importance to dust dissipation.

1.1 Definitions of transitional disks

In this thesis, transitional disks, also called cold disks, are defined as disks with cleared inner regions but substantial outer disks, which contain significant reservoirs of gas and dust. The first step is identifying these rare transitional systems. At infrared wavelengths, spectral energy distrubtions (SEDs) trace the dust temperature structure and it is assumed that temperature is primarily linked to radius with material close to the star being hotter. Because there is a large scale temperature gradient

across the disk, the opening of a gap causes a reduction in flux at specific wavelengths in the SED (see Figure 1.1). However, dust at disk radii between 1 and 100 AU emits most strongly between 2 and 100 μm, where ground based observations are largely blocked by the Earth's atmosphere. Observations with IRAS provided an initial sample of disks lacking mid-IR excess emission arising from $\sim$few 100 K dust, which was interpreted as a sign of dust deficient inner holes (Strom et al., 1989). Further examples and some infrared spectra (e.g. HD 100546, Bouwman et al. 2003) were obtained of a few Herbig Ae/Be stars with the ISO satellite (Waelkens et al. 1994; van den Ancker et al. 1997). The launching of the Spitzer Space Telescope in 2003 again provided access to the mid-IR wavelengths, but with much improved sensitivity compared to IRAS and ISO. The Spitzer cameras can robustly detect young stellar objects down to the hydrogen burning limit in nearby clouds, and not surprisingly a number of new transitional disks around Sun-like stars have been found (Calvet et al. 2002, Forrest et al. 2004, Brown et al. 2007).

Mid-IR spectrophotometry is the diagnostic most widely used to search for the presence of disk gaps with low dust content (e.g. Koerner et al. 1993, Calvet et al. 2002). Spectroscopy has typically been required to identify a gap as the wavelength coverage of broad band photometry limits sensitivity to dust emission at certain disk radii, because the wavelength differences between photometric channels correspond to many tens of AUs of disk radii. While spectra help greatly in analyzing individual objects, the significant amounts of observing time required means that likely targets must be initially identified from large area mapping surveys.

One of the most commonly used indicators of transitional disks is a side product of the infrared slope (parameterized as α) classification system proposed by Lada & Wilking (1984). Using Spitzer data, Lada et al. (2006) revisited this schema and found that their sample split into two major categories, flared disks with $\alpha >$ -1.8 and photospheric disks with α = -2.56. However, a few objects fit into a third category characterized by -2.56 $< \alpha <$ -1.80 and were defined as transitional or anemic disks. Other schema include a combination of disk mass and accretion rate (Najita et al., 2007). The IR procedure used to identify transitional disks in the *c2d* Spitzer Legacy Science program, from which most of the sources studied in this thesis are taken, will be presented in Chapter 2. Since many different physical processes cause disk dissipation (see Section 1.4), identification methods have a large impact on which objects are labeled transitional and which processes are actually being traced.

Submillimeter and millimeter resolved imaging provides a definitive method of identifying central holes. However, subarcsecond resolution is required to image the holes and requires significant

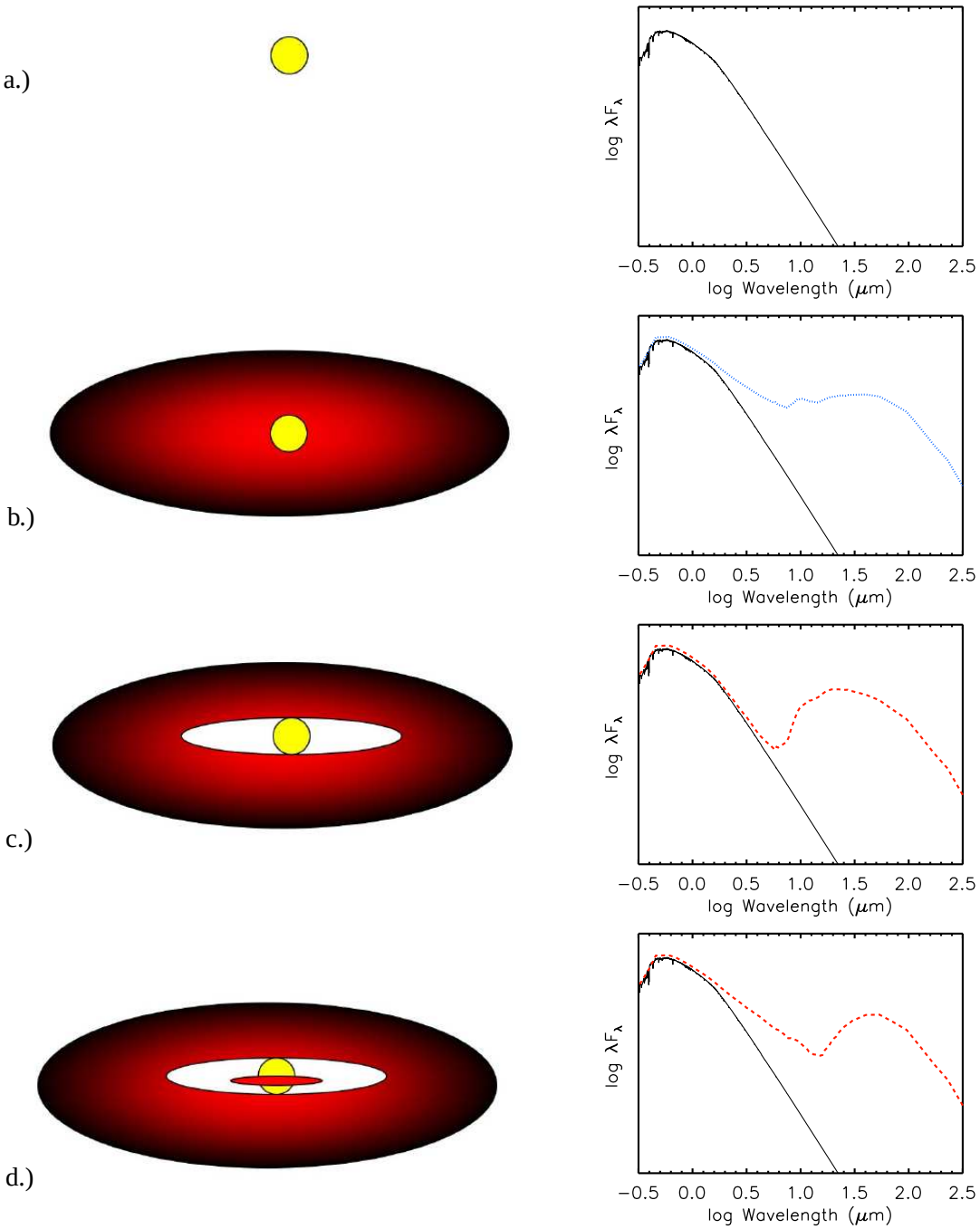

Figure 1.1 a.) The central star produces an SED similar to a blackbody. b.) A disk reprocesses the stellar light to longer wavelengths. c.) A hole in the disk results in the SED being photospheric at shorter wavelengths and then a steep increase in flux. d.) A gap in the disk results in the flux being greater than the photospheric flux at shorter wavelength but a dip in the SED and a steep increase in flux reveal the gap's presence.

observing time. In general, this method is used to follow-up transitional disk identified through other means (Chapter 3, Hughes et al. 2007), although occasionally inner disk holes have been discovered in the millimeter (Piétu et al., 2006).

Submillimeter surveys are sensitive to the larger outer disk and its evolution. Searches for transitional disks in the submillimeter favor discovery of disks where large grains have formed (Beckwith & Sargent 1991, Andre & Montmerle 1994). For the $\sim$100 μm grains to which these wavelengths are particularly sensitive, if the grain population is larger on average, then more flux will be emitted at longer wavelengths, resulting in a flatter submillimeter slope. Conversely, if substantial reservoirs of small grains remain, more flux will be emitted at shorter wavelengths and the slope will steepen. However, such searches require optically thin disks and do not trace small warm grains in the inner regions. While these transitional disks may have evolved, grain growth will not necessarily lead to the central hole characteristic of cold disks.

1.2 The structure of disks

Determination of the physical conditions and internal structure of the disks is crucial to determining which transport/dissipation processes are dominant. A wide range of conditions exist in circumstellar disks which exhibit both strong radial and vertical gradients. Radially, gas and dust near to the star are hotter than material at greater distances. In addition, for so-called passive disks, in which the energy liberated by accretion is small compared to that of the central stellar luminosity, it is essential to understand the properties of the central star because it drives the evolution of the entire system. The radiation field from the star influences both the physical and chemical properties of the disk, creating very different environments around high and low mass pre-main sequence (PMS) stars. The vertical structure in passive disks is stratified with a temperature gradient from the hotter surface layers to the colder midplane, because the disk interior is shielded from stellar and interstellar radiation by the surface layers, in which an active gas-phase chemistry is stimulated by the input of energy. Dust grains can gravitationally settle towards the midplane, making conditions even more diverse. Heating by stellar light in the near-surface layers evaporates the volatile ices in the disk and excites gas phase molecules. Far-ultraviolet photons can drive an ice chemistry and can excite small dust grains (PAH molecules) as well. In hydrostatic equilibrium the disks have a flared geometry with increasing radius, exposing a greater fraction of the disk to the radiation, than in the flat disk case.

Since the range of physical conditions varies greatly throughout the disk, it is important to observe disks at different wavelengths. Spatially unresolved observations across the range of wavelengths at which the disks emit yield (somewhat model dependent) constraints on the physical dust properties of the disk. To study inner disk conditions, it is possible to observe the dust in the near-infrared and to detect molecular transitions of appropriate energy, such as the CO (v=1→0) rovibrational band at 4.7 μm. To observe the cold, outer portions of the disk and enveolpe, it is necessary to study the dust via its (sub)millimeter emission and the gas in lower-energy pure rotational transitions, such as the CO J=1-0 line at 3 mm.

1.3 Formation of planets

To date, over 250 exosolar planets have been discovered (Udry & Santos, 2007). Searches for planets have mainly been undertaken via the radial velocity technique, where stellar photospheric absorption lines are monitored over long time intervals to look for the minute shifts of the radial velocity that arise from the gravitational pull of the planet (Marcy et al., 2005). This technique, unfortunately, only gives sin(i) times the mass of the companion [$Msin(i)$] and no information on the inclination angle of the system is obtained. In order to solve this degeneracy between inclination and mass, large scale searches have been undertaken for transiting planets, in which case sin(i)$\approx$1, where the planet occludes a fraction of the star causing the flux to drop (Udalski et al., 2002).

One of the most interesting early discoveries of the radial velocity searches was the so called "hot Jupiters" – Jupiter-mass planets close in to the central star and hence hot. The structure of our solar system lends itself to an orderly picture of planet formation with circular orbits and with small rocky planets in the inner few AU and massive gas giants in the outer system. However, many of these new planetary systems are very unlike our own with highly elliptical orbits and no mass segregation. The clues to these differences are likely to lie in the early stages of formation, before the systems settle into dynamical equilibrium. Both radial velocity and transit techniques for finding new planets come with inherent biases, with the former biased towards higher mass, closer in planets, particularly on short observational timescales. Transit searches are obviously dependent on inclination for the planet to pass in front of the star in our line of sight, limiting the fraction of planets observable this way but are also biased towards larger sized planets. Purpose-built instruments, like Kepler, will survey vast numbers of stars to ensure large enough statistics to detect many transiting planets, potentially down to terrestrial masses at orbital radii of $\sim$1 AU.

Astrometry, where the movement seen in the radial velocity method is tracked through minute shifts in the position rather than stellar lines, is likely to become a popular method for finding planets in the near future. This method does not have the mass-inclination degeneracy allowing accurate mass determination nor is it inclination dependent for discovery. Masses have been determined for several known exosolar planets using the Hubble Space Telescope Fine Guidance Sensors (Benedict et al. 2002, 2006, McArthur et al. 2004).

Two main theories of planet formation have arisen. The first is the core-accretion scenario, where planetesimals grow to several Earth masses and accrete the surrounding gas creating gaps in the disk (Pollack et al., 1996). However, timescale estimates for this process range over a few x 10 Myrs (e.g. Bodenheimer et al. 2000), while loss of gas from the disk proceeds on timescales of $\sim$3-5 Myr (IR - Strom et al. 1989, mm - Beckwith et al. 1990). Thus, the timescales required to form Jupiter mass gas planets by core-accretion are very long and not in agreement with circumstellar disk evolutionary timescales. Recent suggestions to solve this discrepancy include gas drag (e.g. Rafikov 2004) and 'dead zones' of low turbulence (e.g. Matsumura & Pudritz 2005) to produce Jovian planets in timescales of a million years.

The second prominent theory is gravitational instability, where density perturbations cause build up of matter and accelerate planet formation (Boss 2001, for a recent review see Durisen et al. 2007). While this is an attractive theory due to the ability to generate potential planets in $<$1 Myr old systems, several theoretical questions remain about its validity. Gravitational instability theory is based on the rapid formation of self-gravitating clumps, resulting in planets within $\sim$1000 years. The clumps must form in suitable locations, and in order for planets to form the clumps must survive and continue to contract after formation. Contraction is dependent on the disk midplane cooling in order for gravitational forces to overcome the internal thermal pressure.

The region of planet formation is also uncertain. Planets could migrate toward the star via disk-planet interactions (Lin et al., 1996) or could have formed in-situ (Bodenheimer et al., 2000). Migration scenarios are viewed as more likely and are closely tied to the gas evolution as migration stops when the gas has dissipated. These scenarios inevitably have very different initial conditions and outcomes for planet formation.

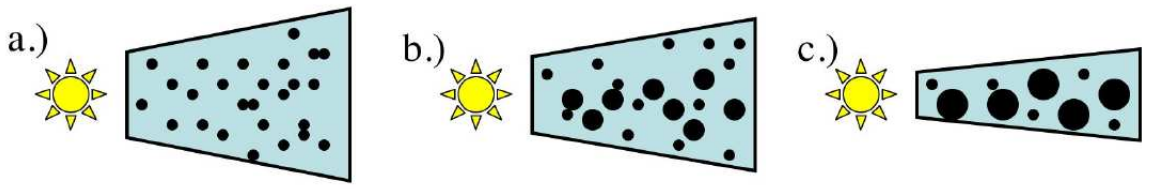

Figure 1.2 An overview of dust coagulation and planetesimal formation in disks. a.) Small dust grains are abundant and the disk has large scale height. b.) Grains begin to coagulate and grow, with large grains settling to the midplane. c.) Large dust grains have continued to grow and settled to the midplane. Some small grains are present even if coagulation is efficient due to collisions and fragmentation of the larger grains.

1.4 Dissipation of protoplanetary disks

It has become clear through large studies of different young clusters that, while the individual ages and timescale for disk evolution vary, overall stars lose their disks within a few Myr (Haisch et al. 2001, Hillenbrand 2006). Many different evolutionary processes have been proposed to occur in disks, of which physical clearing of the disk by planet formation is one of the most exciting scenarios. When a planet's Roche lobe is greater than the disk height, a gap forms around the planet's orbital radius (Lin & Papaloizou, 1986). However, the gap must be maintained in viscous disks, with the viscosity being less than the tidal torque so the gap does not close in less than an orbital timescale. Once a gap has formed, accretion onto the protoplanet should slow dramatically. Numerical simulations have shown the Jupiter-mass planets can clear inner holes on timescales shorter than the viscous or planet migration timescales (Varnière et al., 2006). More recent simulations have suggested that planets below Jovian mass can allow some gas to accrete inward, but stop dust grains (Rice et al., 2006).

Another possibility involves the growth of dust grains to beyond sizes where they emit efficiently. Grain growth and dust settling should naturally occur in protplanetary disks as material flattens into a disk with increased densities (see Figure 1.2). Signs of grain growth have been seen at many wavelengths including the 10 and 20 μm amorphous silicate features (Kessler-Silacci et al., 2006) and in the (sub)millimeter (Rodmann et al., 2006). Dust settling changes the disk geometry and can be seen in the SED (Dullemond & Dominik, 2005).

Finally, photoevaporation is expected to significantly impact the disk gas, particularly in low mass disks (Clarke et al. 2001, Alexander et al. 2006). This physical process occurs when the pho-

toevaporation rate driven by the ionizing flux from the central star matches the viscous accretion rate, resulting in an inner hole. In the simplest model, the predicted size of the inner hole is given by $R_g = GM_*/c_s^2$, where $T \sim 10^4$ K and sound speed $c_s \sim 10$ km/s, typical of photodissociation and HII regions, and leads to predicted hole radii of 13-18 AU for 1.5-2 $M_\odot$ stars. A more rigorous examination of the gas dynamics reveals that this equation overestimates the inner hole size (Liffman, 2003). Further, models of Herbig Ae stars (M_*=2.5 $M_\odot$) that combine photoevaporation with viscous evolution and differential radial motions of dust and gas predict that the inner disk clears quickly but leaves gas-poor dust rings at 10-100 AU (Takeuchi et al., 2005).

Disks can also be destroyed by photoevaporation from the ambient UV field rather than from UV radiation from the central star. This is particularly likely in OB associatiations, like Orion, where the diffuse UV field is dramatically enhanced. Preferential photoevaporation of the gas could leave the dust more prone to gravitational instabilities and hence promote planetesimal formation (Throop & Bally, 2005).

In order to improve our understanding of planet formation, all these different pieces must be explored and reconciled, for knowledge of the process and timescales of dust and gas dissipation is crucial to understanding disk evolution and planet formation. Jovian planets must obviously form while gas and dust are still present.

Transitional disks have a key role to play in this exploration, and the number of known transitional disks has dramatically increased since Spitzer was launched. Here, four newly discovered cold disks around F and G stars are presented in Chapter 2. The Submillimeter Array (SMA) interferometer was used to collect spatially resolved images of three of the new cold disks and confirm the interpretation of the SEDs as disks with large inner holes (Chapter 3). Keck NIRSPEC high spectral resolution echelle data (Chapter 4) provide information about the gas content, in this case traced by CO, of the inner disk region and complement the dust constraints provided by Spitzer. The Caltech Submillimeter Observatory (CSO) SHARCII camera provides a quick method of examining the cold dust and determining the Rayleigh-Jeans slope of the thermal dust blackbody to look for grain growth (Chapter 5). Finally, the Combined Array for Research in Millimeter Astronomy (CARMA) was used to search for cold gas and measure disk sizes and inclination angles (Chapter 6).

Chapter 2

Discovering cold disks with Spitzer

(Adapted from Brown et al. 2007, ApJ, 664, L107)

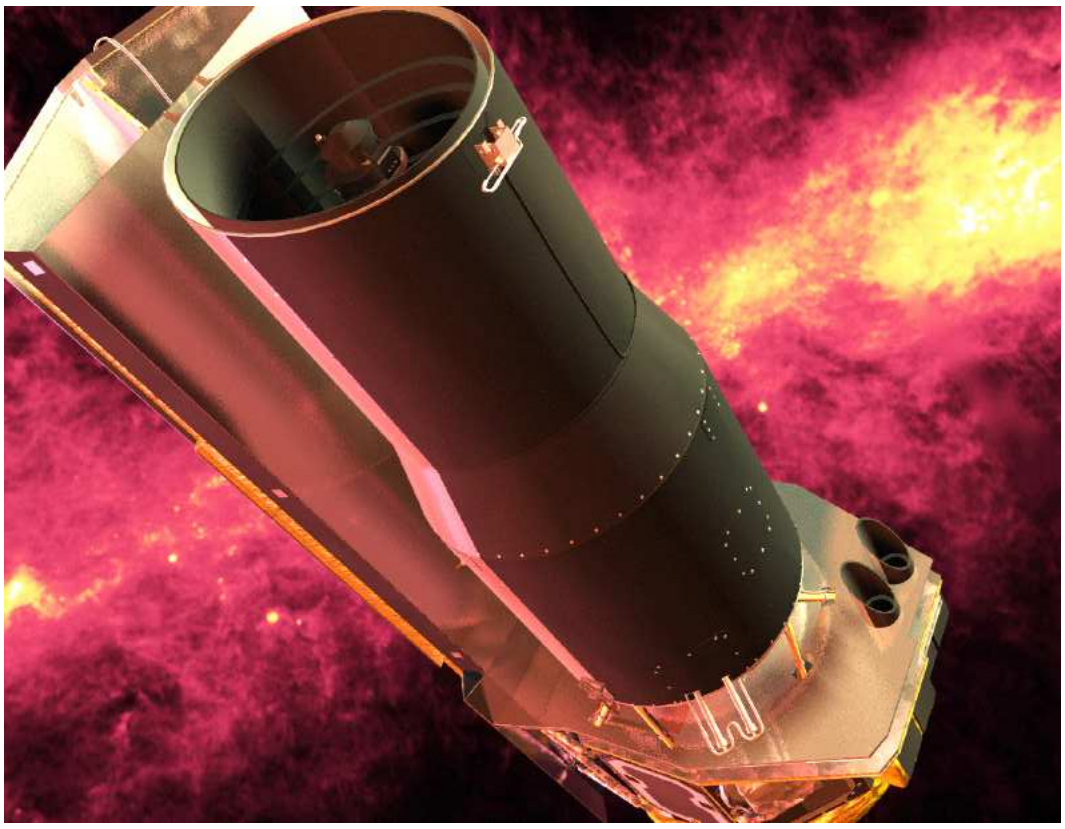

Abstract

I have identified four circumstellar disks with a deficit of dust emission from their inner 15-50 AU. All four stars have F-G spectral type and were uncovered as part of the *Spitzer Space Telescope* "Cores to Disks" Legacy Program Infrared Spectrograph (IRS) first look survey of $\sim$100 pre-main sequence stars. Modeling of the spectral energy distributions indicates a reduction in dust density by factors of 100-1000 from disk radii between $\sim$0.4 and 15-50 AU, but with massive gas-rich disks at larger radii. This large contrast between the inner and outer disk has led us to use the term 'cold disks' to distinguish these unusual systems. However, hot dust [0.02-0.2 $M_{\rm moon}$] is still present close to the central star ($R \leq$0.8 AU). The 30/13 μm flux density ratio is introduced as a new diagnostic for identifying cold disks. The mechanisms for dust clearing over such large gaps are discussed. Though rare, cold disks are likely in transition from an optically thick to an optically thin state, and so offer excellent laboratories for the study of planet formation.

2.1 Introduction

The evolutionary processes transforming massive, gas-rich circumstellar disks into tenuous, gas-poor debris disks are still not well understood. During this crucial interval, planets form and the remaining disk material is accreted or dispersed. The path by which this transition proceeds remains uncertain. Do disks clear uniformly throughout via grain growth and settling, or is the process accelerated in the inner regions forming gaps (e.g. Alexander et al. 2006)? Evidence of dust clearing should be visible in the infrared (IR) spectral energy distribution (SED). The *Spitzer Space Telescope*, with its wide wavelength coverage and increased sensitivity, is starting to reveal a new population of disks with unusual SEDs.

Lack of mid-IR excess emission from disks has been interpreted as a sign of dust clearing since the first disk SEDs were observed with IRAS (Strom et al., 1989). Further examples and some spectra (e.g. HD 100546, Bouwman et al. 2003) were obtained of a few Herbig Ae/Be stars with the ISO satellite. Here, we designate disks with this characteristic missing mid-IR emission as 'cold disks' due to the lack of emission from warm dust. These SEDs morphologically fall between the SEDs of classical optically thick disks, which show excess emission throughout the IR, and debris disks characterized by very weak far-IR excesses, leading them to be considered as transitional objects between the two classes.

Spitzer spectra are particularly important to characterize the sharp rise, since they cover the critical 8-30 μm range. The earliest example discovered with Spitzer was CoKu Tau 4, which was modelled with an inner hole of 10 AU radius (Forrest et al. 2004, D'Alessio et al. 2005). Three additional T Tauri stars, TW Hya, GM Aur and DM Tau (Calvet et al., 2002, 2005), have been identified as also containing cleared inner regions. One of the most exciting proposed explanations for these cold disks is that a planet has cleared a gap in the disk and thus that these inner holes may trace the presence of planetary systems (Varnière et al., 2006).

In this chapter, I present Spitzer spectra of four young stars of F-G spectral type that show a deficit of dust emission from the inner 15-50 AU of the disk yet strong excesses longward of 20 μm. These cold disk sources were identified in the first look survey of the Cores to Disks (c2d) Spitzer Legacy Project (Evans et al., 2003), comprising $\sim$100 young ($<$ 10 Myr old) stars, mainly T Tauri K and M stars, with circumstellar disks. All four sources are characterized by a steep, $\sim$10$\times$ rise in flux beginning at 15 μm, indicating a sudden change in disk properties at a specific radius in a manner similar to that seen in the T Tauri transitional disks. Such objects are rare but provide an

important window into disk evolution and planet formation processes.

2.2 Observations

2.2.1 Sample properties

T Cha is a G8 PMS star at a Hiparcos distance of only 66^{+19}_{-12} pc, much closer than the estimated distances to the Chammaeleon I (160 $\pm$15 pc) and II (178$\pm$18 pc) star formation regions (Whittet et al., 1997) and has been associated with the "Cha-Near" moving group (Zuckerman & Song, 2004). The strong variability of the Hα line profile from pure emission to inverse P Cygni on a time scale of one day or less led Alcalá et al. (1993) to classify T Cha as a 'weak-line' YY Ori star. YY Orionis stars are a subset of T Tauri stars, characterized by strong UV continua and substantial photometric and spectroscopic variability on short time-scales as well as inverse P Cygni line profiles indicative of mass accretion onto the star (Walker, 1972). The system inclination is proposed to be sufficiently large that the edge of the disk can produce variable absorption that leads to significant optical variability.

HD 135344B is an 8 Myr old F4 star in Lupus that lies only 20 arcseconds from its A-type companion HD 135344A. The two stars are likely not physically associated. The dust disk around HD 135344B has been spatially resolved in UV scattered light (Grady et al., 2005) and the mid-IR (Doucet et al., 2006). A close ($0\farcs32$ separation) binary system lies $5\farcs8$ to the southwest (Augereau et al., 2001).

LkHα 330 is a G3 star near the IC 348 region of Perseus, which is a sparse cluster with stars between few to ten million years old (Strom et al., 1974). LkHα 330 has not been well studied. The distance to Perseus is an unresolved problem with values ranging from 200 to 350 pc. A distance of 250 pc is assumed following the c2d convention.

SR 21 (a.k.a. Elias 2-30) is a 3 Myr old binary, with a separation of $6\farcs4$, in the core of the ρ Ophiucus cloud (Prato et al., 2003). The primary has a spectral type of G2.5, while the companion has spectral type M4. A recent VLT/NACO AO survey found no other companions (Correia et al., 2006). Interestingly, Prato et al. (2003) found that the two companions were not coeval within their limits, although large uncertainties remain. The disks of the two components are closely aligned indicating that the stars are likely gravitationally bound (Jensen et al., 2004).

2.2.2 Data collection

The Spitzer Space Telescope, launched in 2003, has three instruments, the InfraRed Array Camera (IRAC; 3.6, 4.5, 5.8, and 8.0 μm), the Multiband Imaging Photometer (MIPS; 24, 70, and 160 μm), and the Infrared Spectrometer (IRS, 5-40 μm). The 5-35 μm spectra presented here were taken with IRS (Houck et al., 2004) using both the low (R=160, λ_{SL}:5.2-14.5μm, λ_{LL}:14.0-38.0μm) and high (R=600, λ_{SH}:9.9-19.6μm, λ_{LH}:18.7-37.2μm) resolution modules. Spectra were extracted from the Spitzer Science Center (SSC) Basic Calibrated Data (BCD) images, generated by pipeline S13. For the low resolution spectra, the SSC pipeline full aperture extraction was used. For the high resolution modules, the c2d extraction, based on a combined sinc fitting of the spectral trace to account for bad pixels and background emission, was used (see Lahuis 2006 for further details[1]).

MIPS SED spectra, also taken as part of the c2d project, are included in the SEDs for all four cold disk sources. For each source, the BCDs were coadded using MOPEX. The coadded images were extracted with IRAF, using an optimized extraction with a 3 or 5 column aperture.

2.3 Distinguishing characteristics

The large ($\sim$100 object) c2d IRS first look sample allows comparison between the four cold disk sources and the remaining systems to identify trends that might be diagnostic of their evolutionary state. Although this sample is not completely unbiased, none of these sources was selected based on prior knowledge of the gap. The small number of cold disk sources ($<$ 5% identified), both in the c2d sample and in the literature, suggests that this condition is rare either due to rapid evolutionary timescales undergone by all stars or due to an unusual condition unique to a small sample of stars.

The four cold disk sources are clearly differentiated from the majority of the c2d star+disk systems by the $\sim$10 fold increase in IR flux between 10 and 30 μm. To characterize this increase in dust emission, we have used the 30/13 μm flux ratio (see Figure 2.1). These wavelengths have been chosen to avoid strong silicate features, while including the full increase in continuum emission. The majority of the sample has emission that increases by a factor of 2.3 $\pm$ 1.4 between 13 and 30 μm, while the transitional disks rise by factors of 5-15.

Interestingly, out of a sample comprised of predominantly low-mass stars, the cold disk sources are all of intermediate mass with spectral types of F and G (see Figure 2.2). The majority of K and M stars and the higher mass A and B stars have low 30/13 μm ratios. However, there are only a

[1]Lahuis et al. 2006 is available at: http://ssc.spitzer.caltech.edu/legacy/c2dhistory.html

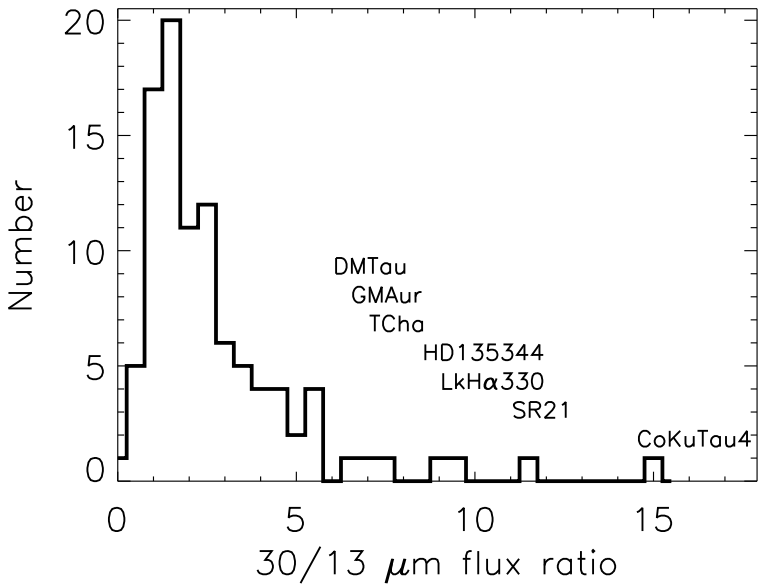

Figure 2.1 Spitzer IRS 30/13 μm flux ratios for the c2d first look disk sample, along with those of DM Tau, GM Aur and CoKu Tau 4. The cold disks have much larger 30/13 μm ratios than does the majority of the sample. Outliers are labeled.

handful of A and B stars in our sample, so it is difficult to draw any significant conclusions about such systems.

All four cold disk sources show polycyclic aromatic hydrocarbon (PAH) features, particularly at 11.3 μm. Such emission is uncommon in the c2d sample with only $\sim$10% of the disks displaying PAH features and none of the embedded sources (Geers et al. 2006, see their Figure 5 for blow-ups of the PAH bands). The presence of PAH features may be enhanced in these cold disks because the lack of dust in the inner disk lowers the mid-IR continuum flux, creating a stronger line-to-continuum ratio and thus facilitating detection.

The four disks are also characterized by weak to non-existent 10 μm amorphous silicate features. LkHα 330 is the only one that shows an unambiguous, though low contrast, 10 μm feature. The spectrum of HD 135344B includes the wavelength region of the full 10 μm band but shows no silicate feature. The spectra of SR 21 and T Cha begin at 10 μm in the c2d database, but appear to have only weak silicate emission, if any. The broader 20 μm silicate feature is harder to isolate from continuum dust emission, particularly with the sharp rise in the SED beyond 15 μm, but some 20 μm emission does seem to be present. This feature traces colder regions of the disk than does the 10 μm feature, and thus indicates the presence of amorphous silicates further out in the disks.

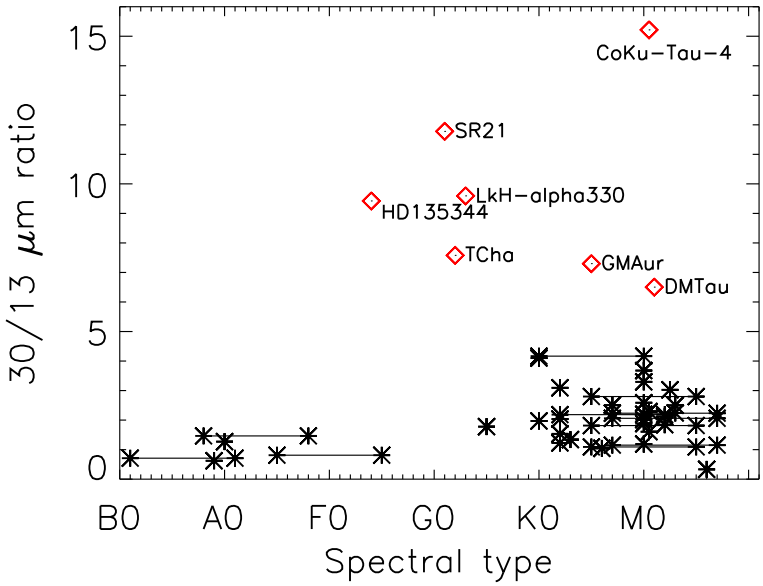

Figure 2.2 Spectral types of the c2d first look survey compared to the Spitzer IRS 30/13 μm ratios. The bars represent the range of values presented in the literature rather than error bars. The four cold disks are the majority of F/G stars in this sample.

The Hα equivalent width is often used as a tracer of accretion. Different dividing lines between non-accreting weak-line T Tauri stars (wTTs) and classical T Tauri stars (cTTs) have been proposed, but it makes little difference to the classifications in these cases. SR 21 (0.54 Å in absorption, Martin et al. 1998) and T Cha (2-10 Å, Gregorio-Hetem et al. 1992, Alcala et al. 1995) are nominally wTTs, although T Cha is highly variable and close to the cutoff. LkHα 330 (11-20 Å, Fernandez et al. 1995, Cohen & Kuhi 1979) and HD 135344B (17.4 Å, Acke et al. 2005) are clearly cTTs (see Figure 2.3).

2.4 Modeling

Modeling is necessary in order to interpret the SEDs in terms of the physical structure of the disk. In particular, can a disk model with a gap accurately reproduce the SEDs, including the steep rise between 13 and 30 μm? Is such a fit possible without resorting to a gap?

The disks were modeled with the 2-D radiative transfer code RADMC (Dullemond & Dominik, 2004). RADMC is a 3-D axisymmetric continuum radiative transfer code based on the Monte Carlo algorithm of Bjorkman & Wood (2001). Since the azimuthal direction is considered uniform, the code is essentially two dimensional. A ray-tracing program, RADICAL/RAYTRACE, is used to

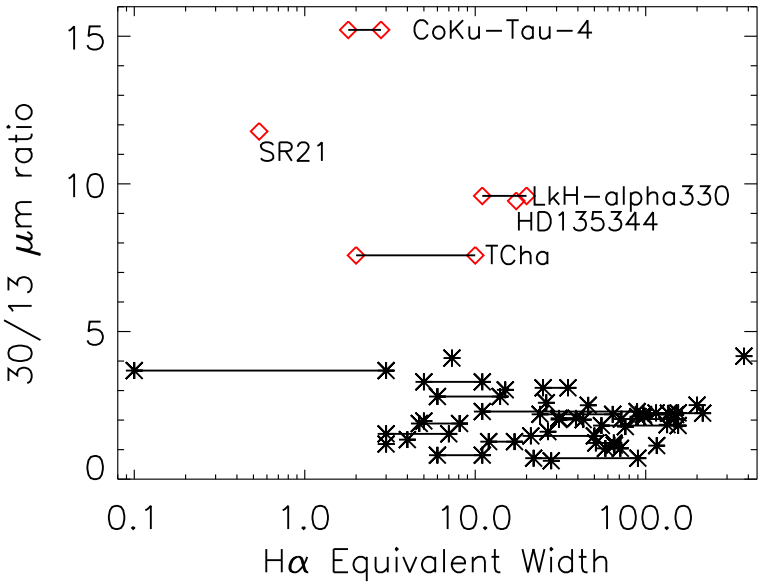

Figure 2.3 Log of Hα equivalent width of the c2d first look survey compared to Spitzer IRS 30/13 μm ratio. The bars represent the range of values presented in the literature rather than error bars. The values for most of the sample can be found in Kessler-Silacci et al. (2006).

produce spectra and images at different inclination angles without rerunning the full radiative transfer. Pascucci et al. (2004) present the results of benchmark tests of both RADMC and RADICAL against other state-of-the-art 2-dimensional disk codes. The disk structure, including temperature and density profiles, are user defined and, in this case, follow a modified Chiang & Goldreich (1997) setup.

The steep factor of 10 rise in flux between 13 and 30 μm prevents these disks from being fit well by conventional disk models. I adapted the modeling code to introduce a very wide gap with an inner radius, $R_{\rm Gap,in}$, near 1 AU and an outer radius, $R_{\rm Gap,out}$, near 30 AU (see Table 2.1 for specific values). In order to model the steep change in emission associated with $R_{\rm Gap,out}$, grid refinement is introduced at $R_{\rm Gap,out}$ to avoid problems with extremely optically thick grid cells as well as the inner dust rim, $R_{\rm Disk,in}$. A physical reduction in dust density is only one possible scenario which could result in this SED shape (see §5).

Input parameters for these models include the stellar mass, M_*, radius, R_*, and effective temperature, $T_{\rm eff}$. Kurucz models are used for the stellar photospheres. Where possible, values for stellar and disk properties are taken from the literature (see Table 2.1). The Siess et al. (2000) pre-main sequence stellar tracks were used to check that the parameters were consistent. The effects of modest

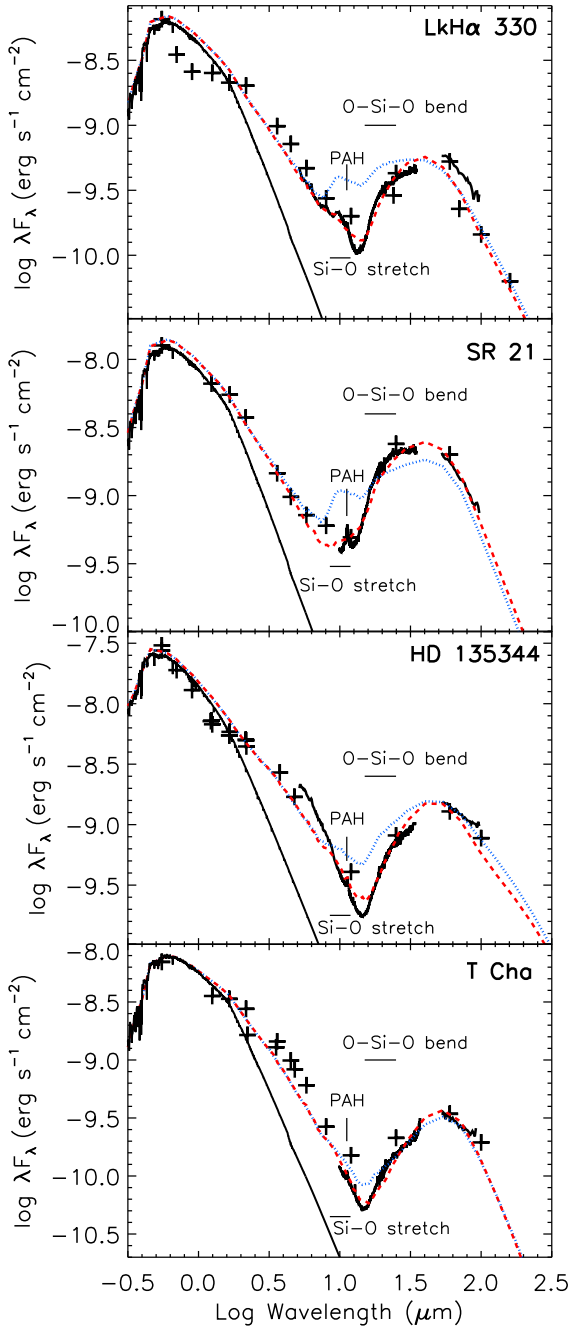

Figure 2.4 Spitzer IRS and MIPS spectra of the four cold disk sources reported here. The dashed line is the best fit star+disk model with a gap (see Table 2.1) and the dotted line is the equivalent model with no gap. JHK photometry is from 2MASS. IRAS photometry and our Spitzer photometry is shown in the mid- to far-IR. Optical and submillimeter photometry is from the literature (Alcalá et al. 1993; Andre & Montmerle 1994; Fernandez & Eiroa 1996; Henning et al. 1993; Osterloh & Beckwith 1995).

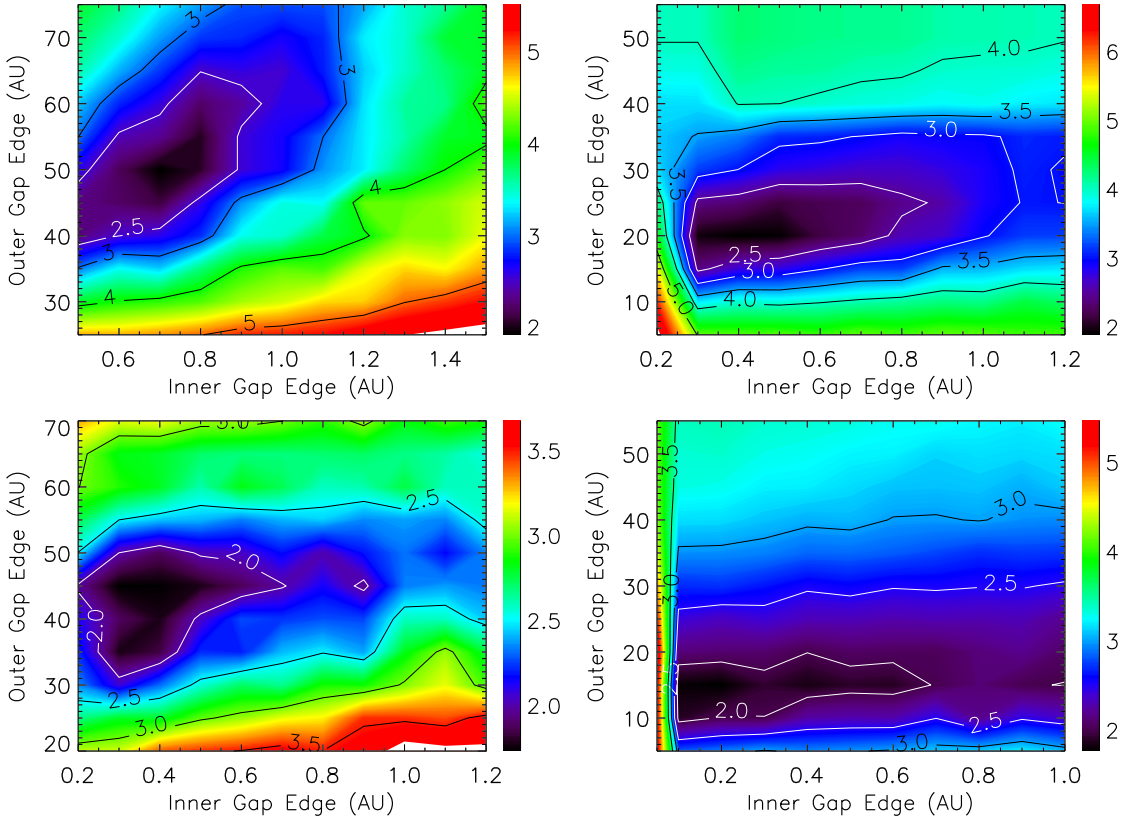

Figure 2.5 Chi squared contour maps of 2-D disk model fits to the SEDs with different inner and outer gap radii (clockwise from top left: LkHα 330, SR 21, T Cha and HD 135344).

Table 2.1. Model parameters

Source	Spectral Type	A_v (mag)	Distance (pc)	M_* ($M_\odot$)	$T_{\rm eff}$ (K)	L_* ($L_\odot$)	$R_{\rm Disk,in}$ (AU)	$R_{\rm Gap,in}$ (AU)	$R_{\rm Gap,out}$ (AU)	$M_{\rm Dust,small}$ ($10^{-6}\,M_\odot$)	$M_{\rm inner}$ ($M_{\rm lunar}$)	$H_{\rm p}(R_{\rm disk})/R_{\rm disk}$
LkHα 330	G3[a]	1.8[a]	250[b]	2.5[c]	5800	16	0.27	0.8	50	5	0.24	0.15
SR 21	G2.5[d]	9[d]	160	2.5[d]	5800	24	0.25	0.45	18	15	0.10	0.17
HD 135344B	F4[e]	0.5[f]	84[e]	1.8	6600[e]	6.8	0.18	0.45	45	5	0.10	0.13
T Cha	G8[g]	1.5[g]	66[h]	1.5[g]	5600	1.4	0.08	0.2	15	3	0.025	0.11

[1] *a* - Cohen & Kuhi (1979), *b* - Enoch et al. (2006), *c* - Osterloh & Beckwith (1995), *d* - Prato et al. (2003), *e* - Dunkin et al. (1997), *f* - Malfait et al. (1998), *g* - Alcalá et al. (1993), *h* - Wichmann et al. (1998)

differences in the stellar properties on the mid-IR portions of the SED are small. For example, a 100 K change in $T_{\rm eff}$ results in a change in $R_{\rm Gap,out}$ of 2-3 AU. Optical and (sub)millimeter photometry is often not simultaneous and is dereddened using the extinction law of Draine (2003).

The disks are assumed to be flared with surface height H such that $H/R \propto R^{2/7}$, as in Chiang & Goldreich (1997). The models do not calculate the hydrostatic equilibrium self-consistently and here the pressure scale height is set at the outer disk edge, $R_{\rm disk}$, which is assumed to be 300 AU for all the models. H/$R_{\rm disk}$ values slightly lower than predicted by hydrostatic equilibrium are needed to fit the outer disks of both HD 135344B and T Cha, leading to a smaller silicate feature even in the models with no gap. This could indicate dust settling in the outer disk, which might be expected from the older ages (8-10 Myr vs 2-3 Myr) infered by the Siess et al. (2000) tracks. The dust composition is set in all models to have a silicate:carbon ratio of 4:1. The grain sizes range from 0.01 to 10 μm, with a power-law index of -3.5 and a dust mass of $M_{\rm Dust,small}$. The upper size limit of 10 μm is large compared to interstellar grains (Mathis et al., 1977), but was necessary to account for the lack of any 10 μm amorphous silicate feature. This indicates a skewing of the size distribution, likely through grain growth. No crystalline silicates are included. A midplane layer of 2 mm grains containing 90% of the total dust mass, with the remaining 10% in $M_{\rm Dust,small}$, has been added to account for the (sub)millimeter slope (as in Dullemond & Dominik 2004, see also Chapter 5). The inner edge of the disk, $R_{\rm Disk,in}$, was set at the radius where the dust sublimation temperature of $T_{\rm dust}$ $\sim$ 1500 K is reached. A slightly puffed-up inner rim was included, with $H/R_{\rm Disk,in}$ being set at 0.03, just above the hydrostatic equilibrium value. The disk inclinations are not well constrained, so $i \sim 30^\circ$ was used arbitrarily for SR 21 and LkHα 330. Resolved imaging later confirmed that the estimated inclinations were approximately correct (see Chapter 3). T Cha is more edge-on so $i \sim$

75° was adopted (Alcalá et al., 1993), and HD 135344B is more face-on with $i \sim 10°$ (Dent et al., 2005). However, until the disk is nearly edge-on and begins to obscure the central star, varying the inclination produces little effect on the gap properties.

The optimal size of the gap necessary to fit the mid-IR is found by minimizing the χ^2 of the fit (see Figure 2.5). $R_{\rm Gap,out}$ is tightly constrained by the steep rise at 13 μm, while $R_{\rm Gap,in}$ is less well constrained. The dust density in the gap was reduced by 10^{-6} compared to the equivalent models with no gaps, and the minimum reductions needed were factors of 10-100.

All of our sources have 1-10 μm excesses which require 0.02-0.24 $M_{\rm moon}$ of dust between $R_{\rm Disk,in}$ and $R_{\rm Gap,in}$, a fraction of only 10^{-7} to 10^{-6} of the total refractory dust mass available in the standard disk models. This matter is optically thick to the stellar light at the midplane. If we remove *all* material from the disk inward of $R_{\rm Gap,out}$, then the near-IR fluxes are underpredicted. These excesses clearly show that at least some dust must be close to the star (see Figure 1.1 for a sample SED of a completely cleared hole). We model the 1-10 μm excess by keeping the inner disk intact and only inserting a gap from $R_{\rm Gap,in}$ to $R_{\rm Gap,out}$, where $R_{\rm Gap,in} > R_{\rm Disk,in}$. For T Cha, this results in a particularly small, hot dust region inside the gap which would have a very short lifetime, of order thousands of years at most, without a continual influx of material.

2.5 Discussion

I have identified four cold disks around F and G type stars with unusually steep flux increases between 10 and 30 μm , whose SEDs can only be modelled with wide gaps of inner radii of 0.2-0.8 AU and outer radii 15-50 AU. These gaps are generally larger than those inferred for the four lower mass and luminosity T Tauri stars with similar 30/13 μm ratios found previously, which have outer gap radii of 10-24 AU. Another difference is that these F and G sources have small 1-10 μm excesses which demand that hot dust exists between the inner edge of the gap and the star, i.e. the disks studied here have gaps rather than holes. The statistics on sources of different spectral types are still too small to conclude whether the earlier spectral type stars having larger gaps and 1-10 μm excesses is a general trend or peculiar to our sources, and whether this extends to Herbig Ae/Be stars.

Dust clearing related to planet formation would be one of the most exciting explanations for the observed SEDs. Models have shown that Jovian mass planets are capable of opening and maintaining gaps in disks (Bryden et al. 2000,Varnière et al. 2006). However, most models focus on

gaps with maximum extent $\sim$10 AU, and little work has been done on creating the tens of AU sized gaps seen here. There is also the possibility of the disk being disrupted and the dust cleared by a stellar or brown dwarf companion. HD 135344B and SR 21 are part of multiple star systems but the companions are all outside of the modeled disk extent. However, this does not prevent gravitational disturbance of the disk material. Although no companions are currently known within the modeled $R_{\rm disk}$, close binaries ($<$50 AU) cannot be ruled out for any of the sources.

Another proposed scenario for quickly clearing the inner disk region is photoevaporation (Clarke et al. 2001, Alexander et al. 2006). This physical process occurs when the photoevaporation rate driven by the ionizing flux from the central star matches the viscous accretion rate, resulting in an inner hole. The predicted size of the inner hole is given by $R_{\rm g} = GM_*/c_{\rm s}^2$, with $T \sim 10^4$ K, the temperature of typical photodissociation regions, to give $c_s \sim 10$ km/s, leads to predicted hole radii of 13-18 AU for 1.5-2 $M_\odot$ stars, although a more rigorous examination of the gas dynamics revealed that this equation overestimates the inner hole size (Liffman, 2003). However, models of Herbig Ae stars (M_*=2.5 $M_\odot$) that combine photoevaporation with viscous evolution and differential radial motions of dust and gas predict that the inner disk clears quickly but leaves gas-poor dust rings at 10-100 AU (Takeuchi et al., 2005). The accretion rates for all four cold disks, with the possible exception of SR 21, are too high to make this scenario likely, as is the detection of molecular gas inside of $R_{\rm Gap,out}$ (see Chapter 4).

An alternative to physically removing the dust is to let it grow beyond the size at which it efficiently radiates as a blackbody so that it no longer emits strongly in the mid-IR (Tanaka et al., 2005). There is general evidence for grain growth in disks from both mid-IR and millimeter data (Kessler-Silacci et al. 2006, Rodmann et al. 2006). The lack of strong 10 μm amorphous silicate features also points to grains having grown beyond interstellar sizes. There has been much recent modeling work on clearing disks through grain growth. Dullemond & Dominik (2005) found that cold disk SEDs could be produced by dust coagulation but the timescales were too fast. Replenishment of the dust was necessary to match observed lifetimes of the disks. If replenishment processes such as fragmentation occur preferentially in the innermost region due to higher temperatures and densities (Kenyon & Bromley, 2004), this might be sufficient to produce the fraction of a lunar mass of dust needed close to the star. Rice et al. (2006) invoke dust filtration by an embedded planet whereby large grains pile up at the outer edge of the gap while small grains and gas pass through, thus accounting for both the hot small dust grains needed to fit the near-IR and the high mass accretion rates. The high spatial resolution of ALMA should be able to test these scenarios by searching for

and imaging the emission from (sub)millimeter to centimeter sized grains.

Chapter 3

Testing the dust clearing hypothesis: resolved imaging with the SMA

Abstract

Mid-infrared spectrophotometric observations have revealed a small sub-class of circumstellar disks with spectral energy distributions (SEDs) suggestive of large inner gaps with low dust content. However, such data provide only an indirect and model-dependent method of finding central holes. Imaging of protoplanetry disks would provide an independent check of SED modeling. We present here the direct characterization of three 27-40 AU radii inner gaps, in the disks around LkHα 330, SR 21 and HD 135344B. We obtained 340 GHz (880 μm) dust continuum images using the Submillimeter Array (SMA). The large gaps are fully resolved by the SMA observations and mostly empty of dust with less than 1 - 7.5 $\times$ 10^{-6} $M_{\odot}$ of solid dust particles inside the holes. Gas (as traced by accretion markers and CO M-band emission) is still present in all the inner disks. In the LkHα 330 and HD 135344B disks, the outer edges of the gap rise steeply – features in better agreement with the underlying cause being gravitational perturbation than a more gradual process such as grain growth. Importantly, the good agreement of the spatially resolved data and spectrophotometry-based model lends confidence to current interpretations of SEDs with significant dust emission deficits as arising from disks with inner gaps or holes. Further SED-based searches can therefore be expected to yield numerous additional candidates that can be examined at high spatial resolution.

3.1 Introduction

Knowledge of how disks dissipate is vital for our understanding of planetary system formation. Studies have shown that the transition period lasts at most ∼3-5 Myr (e.g. Strom et al. 1989; Beckwith et al. 1990), making the identification of a sample of this important, short-lived phase difficult. One indicator of intermediate systems is the presence of an inner hole or gap indicating that the inner disk has evolved while the outer disk has not. The presence of gaps may indicate that planets have already formed in the disks and cleared the material around their orbits. Such systems can therefore strongly constrain models of planet formation, especially the role of gap formation and disk-planet interactions in various planet migration scenarios that lead to the creation of "hot Jupiters" found to orbit much older systems (Marcy et al., 2005). It is therefore essential to search for other types of evidence that either support or reject the gap hypothesis.

In theory, an inner gap in a proto-planetary disk can be identified from a depressed SED at wavelengths of 1-15 μm, as the absence of hot dust close to the star results in flux coming solely from the stellar photosphere, rather than disk surface emission. To date, such emission "deficits" are the tool most widely used to infer the presence of gaps (Chapter 2, Calvet et al. 2002, Forrest et al. 2004), but spectrophotometric signatures are indirect and notoriously difficult to interpret as multiple physical scenarios can result in the same SED. Additional constraints and detailed models are therefore required to distinguish between the possible physical scenarios that are consistent with the observed fluxes.

The relatively new field of submillimeter interferometry provides access to the small scales involved. Submillimeter imaging is optimal for transitional disk studies as the sources are intrinsically stronger than at longer centimeter and near-millimeter wavelengths. Flux dilution over several beams suppresses the contamination of weak extended emission from nearby molecular cloud material. Long baselines and good (u,v) coverage are vital to provide the high resolution/high dynamic range imaging needed to resolve the gaps. Because submillimeter observations trace optically thin emission in the Rayleigh-Jeans regime, the data are exquisitely sensitive to the mass surface density profile in the disk.

Here I present some of the first direct evidence supporting the gap hypothesis in the form of 340 GHz (880 μm) continuum maps resolving the inner disk holes in the disks around LkHα 330, SR21 and HD 135344. Details about the sources are presented in Section 2.2.1. We first present the relevant observational details before turning to a discussion of the results and their implications for

Table 3.1. Summary of SMA observations

Source	R.A.	Dec.	Beam size	DSB T_{sys}	Observation dates
LkHα 330	03:45:48.28	+32:24:11.8	$0\farcs28$x$0\farcs33$	210-870 K	2006 November 11, 19
SR 21	16:27:10.28	-24:19:12.7	$0\farcs42$x$0\farcs30$	350-1000 K	2007 June 2
HD 135344B	15:15:48.43	-37:09:16.22	$0\farcs47$x$0\farcs25$	280-850 K	2007 May 27, June 7

SED-driven searches for gaps in circumstellar disks.

3.2 Observations

Mid-IR spectrophotometry of LkHα 330, SR 21 and HD 135344B was acquired as part of the Spitzer "From Cores to Disks" (c2d) Legacy Science project (see Chapter 2). Out of a sample of over 100 spectra in the c2d first look program, only 5 disks showed SED features characteristic of an inner hole (Brown et al., 2007). Those disks visible from the northern hemisphere - LkHα 330, SR 21 and HD 135344B - have been targeted for high spatial resolution follow-up imaging at mm-wavelengths.

Dust emission measurements were acquired with the Submillimeter Array (SMA) using the very extended configuration of seven of the 6 meter diameter antennas, which provided baselines ranging in length from 80 to 590 meters. Double sideband (DSB) receivers tuned to 341.165 GHz provided 2 GHz of bandwith/sideband, centered at an Intermediate Frequency (IF) of 5 GHz. Calibration of the visibility phases and amplitudes was achieved with observations of 3C111, typically at intervals of 25 minutes. Measurements of Uranus and Titan provided the absolute scale for the flux density calibration and the uncertainties in the flux scale are estimated to be 15%. Table 3.1 lists the observed source position, the synthesized beam size, DSB system temperatures and the observation dates. Due to their southern position relative to the SMA, HD 135344B and SR 21 have higher system temperatures and more elongated beams than LkHα 330. The data were calibrated using the MIR software package (`http://cfa-www.harvard.edu/~cqi/mircook.html`), and processed with Miriad (Sault et al., 1995).

Table 3.2. Summary of SMA images

Source	F_{total} (mJy)	RMS Noise (mJy)	R_{hole} (AU)	R_{disk} (AU)	F_{hole} (mJy)	M_{hole} (10^{-4} $M_\odot$)	Inclination (°)	Null (nsec)
LkHα 330	59.8	2.3	40	125	2.3	1.3	40	700-800
SR 21	217	3.7	27	140	16.7	7.5	20	700
HD 135344B	314	4.5	37	125	6.7	1.1	20	500

3.3 Data

3.3.1 Image plane

The SMA images clearly resolve the size, orientation and radial structure in all three disks (see Figures 3.1, 3.2 and 3.3). The parameters found directly from the data are summerized in Table 3.2. The total fluxes, $F_{\rm total}$, were found and the S/N range from 25-75 for the three disks (Table 3.2, columns 2 and 3). The hole radii, $R_{\rm hole}$, were measured directly in the images (column 4) and are in good agreement with the SED determined values (see Chapter 2). The outer disk edge, $R_{\rm disk}$, is also resolved. Due to the lower optical depths in the outer disk, this high resolution imaging is likely not sensitive to the outer reaches of the disk, so the radii in column 5 are lower limits. For all the disks, upper limits on the integrated flux within the hole, $F_{\rm hole}$, was derived (column 6). The SR 21 hole is smaller than those in the other disks, so the beam deconvolution will be less sensitive to the hole flux and this is reflected in a higher flux value. In the LkHα 330 image, the flux within the hole is below the 1 sigma noise level of 2.3 mJy. Using the flux to disk mass conversion of Beckwith et al. (1990), which implicitly assumes a gas to dust ratio of 100 (see Section 5.3.3 for further details), limits on the amount of mass in the hole on the order of 10^{-4} $M_\odot$ were calculated (column 7). In the case of LkHα 330, the significant intensity contrast between the inner and outer disk indicates a large mass surface density contrast – even for mm-sized grains. The boundary between hole and outer disk is very abrupt with the flux dropping 25% in less than 10 AU and 50% in less than 20 AU.

3.3.2 (u,v) plane

With a sufficiently sharp transition, aperture synthesis observations should detect a null in the flux versus (u,v)-distance, as opposed to the smooth drop off in flux associated with power-law mass

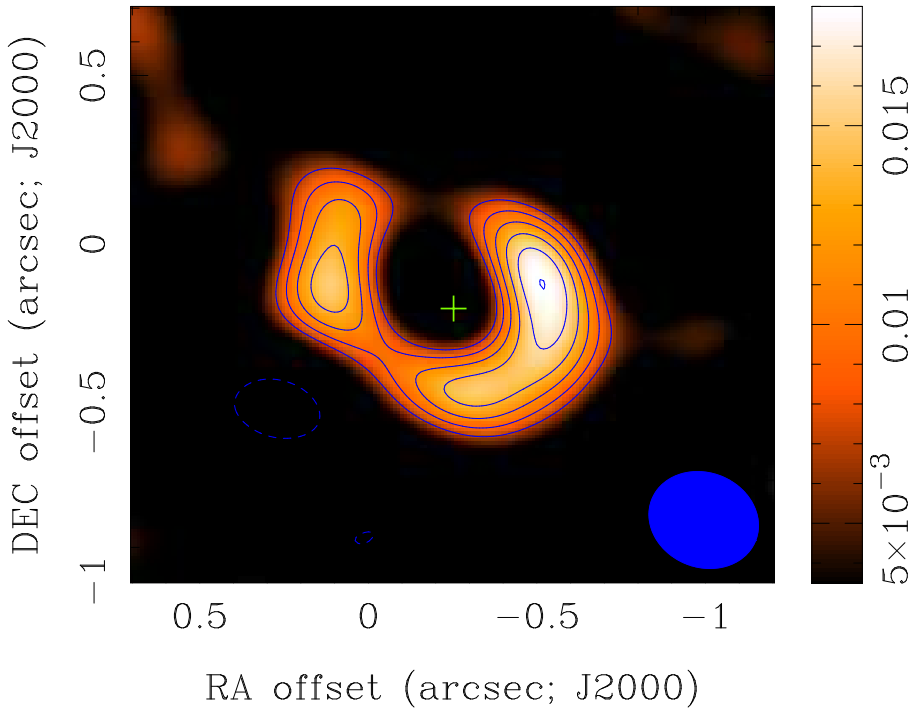

Figure 3.1 The 340 GHz dust continuum image of LkHα 330 from the SMA interferometer clearly shows an inner hole of approximately 40 AU radius. The beam of 0.″28x0.″33 is plotted in the bottom right corner

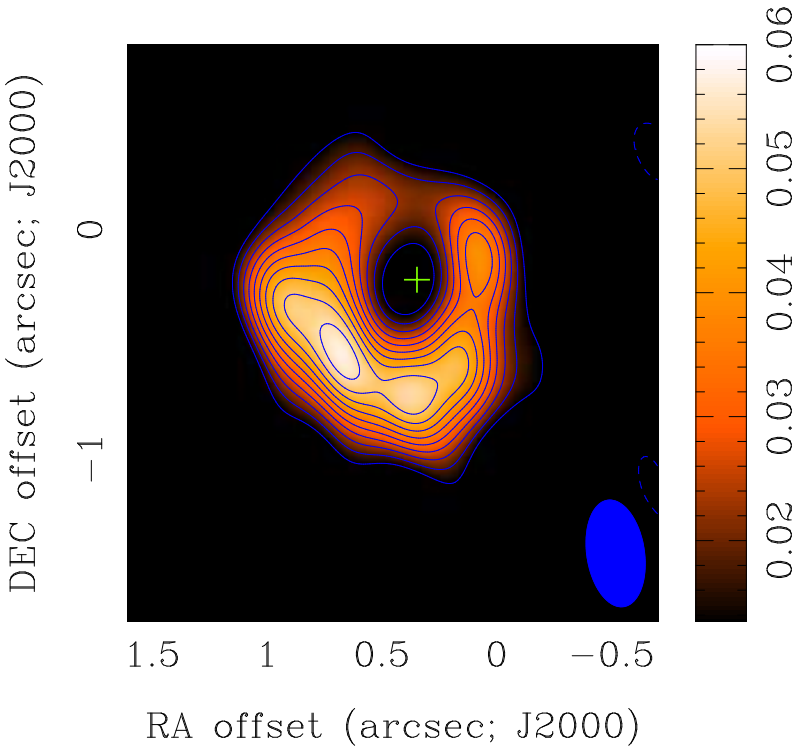

Figure 3.2 The 340 GHz dust continuum image of HD 135344B with a well defined 37 AU hole. The 0.″47x0.″25 beam in the lower right corner is elongated due to this source's -37° degree declination.

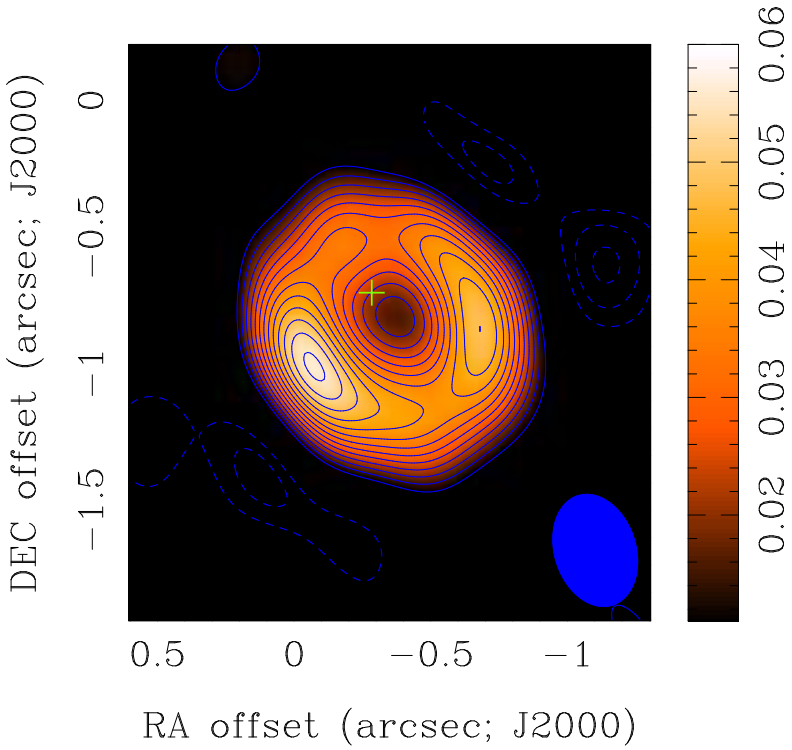

Figure 3.3 The 340 GHz dust continuum image of SR 21 N, which has the smallest hole of this sample with a radius of 20 AU.

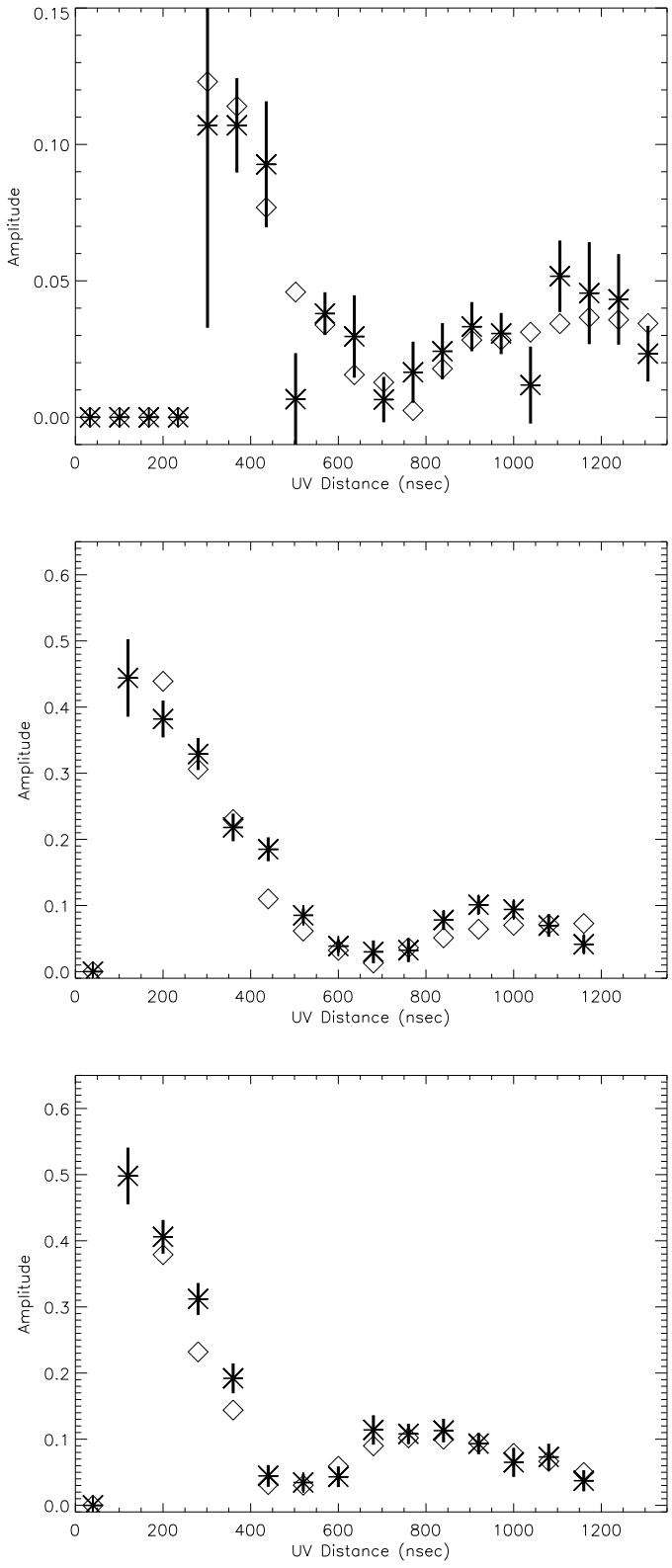

Figure 3.4 Amplitude vs (u,v) distance for, from top to bottom, LkHα 330, SR 21 and HD 135344. The data are marked with stars and the model with diamonds. One sigma error bars are included on the data points.

surface density profiles that characterizes most classical T Tauri star disks (Andrews & Williams 2007b, see also Figure 3.7 for the effects of different sized holes on the (u,v) diagram). A visibility domain analysis also provides a more straightforward means of assessing the uncertainties in any fits, as the data have not been affected by Fourier transforming and non-linear deconvolution. The visibility data were averaged in concentric annuli such that $R = \sqrt{u^2+v^2}$. All three disks do indeed show nulls (see Figure 3.4) and the values are listed in Table 3.2

3.3.3 Spectral energy distributions

To ensure a consistent picture, it is important that the SEDs are in agreement with the SMA images. The total 880 μm flux from the SMA observations was included in the photometry to check the overall flux in relation to other measurements (see stars in Figure 3.5). The integrated fluxes do fit well with the other submillimeter measuements. Fits to the optical through millimeter-wave SED yield estimated gap outer radii for all three disks between 20 and 40 AU (see Chapter 2 or Brown et al. 2007), which are also in agreement with the images.

3.4 Modeling

I used the 2-D radiative transfer model RADMC (Dullemond & Dominik, 2004) as adapted to include a density reduction simulating a gap to simultaneously model the resolved images (see Figure 3.6), the data in the (u,v) plane (see Figure 3.4), and the SEDs (see Figure 3.5). This model assumes a passive disk, which merely reprocesses the stellar radiation field. In order to fit the missing dust emission, the model was adapted to reduce the dust density in a specific region to create a gap in the disk. The resulting image was resampled in Miriad using the same (u,v) plane distribution as the SMA data so the two are directly comparable (see Figure 3.6).

In the model, the disk is assumed to be flared such that the surface height, H, varies with radius, R, as $H/R \propto R^{2/7}$, as in Chiang & Goldreich (1997). Following Chapter 2, the models do not calculate the hydrostatic equilibrium self-consistently, and the pressure scale height is anchored at 0.17 at the outer disk edge, in this case 300 AU. The dust composition is set to a silicate:carbon ratio of 4:1 with only amorphous, rather than crystalline, silicate included. The grain sizes range from 0.01 μm to 10 cm with a power-law index of -3.5 and a total disk mass, including both gas and dust, of 0.017 $M_\odot$ (Osterloh & Beckwith, 1995). The inner edge of the disk, $R_{\rm Disk,in}$, was set at approximately the radius where the dust sublimation temperature is 1500 K.

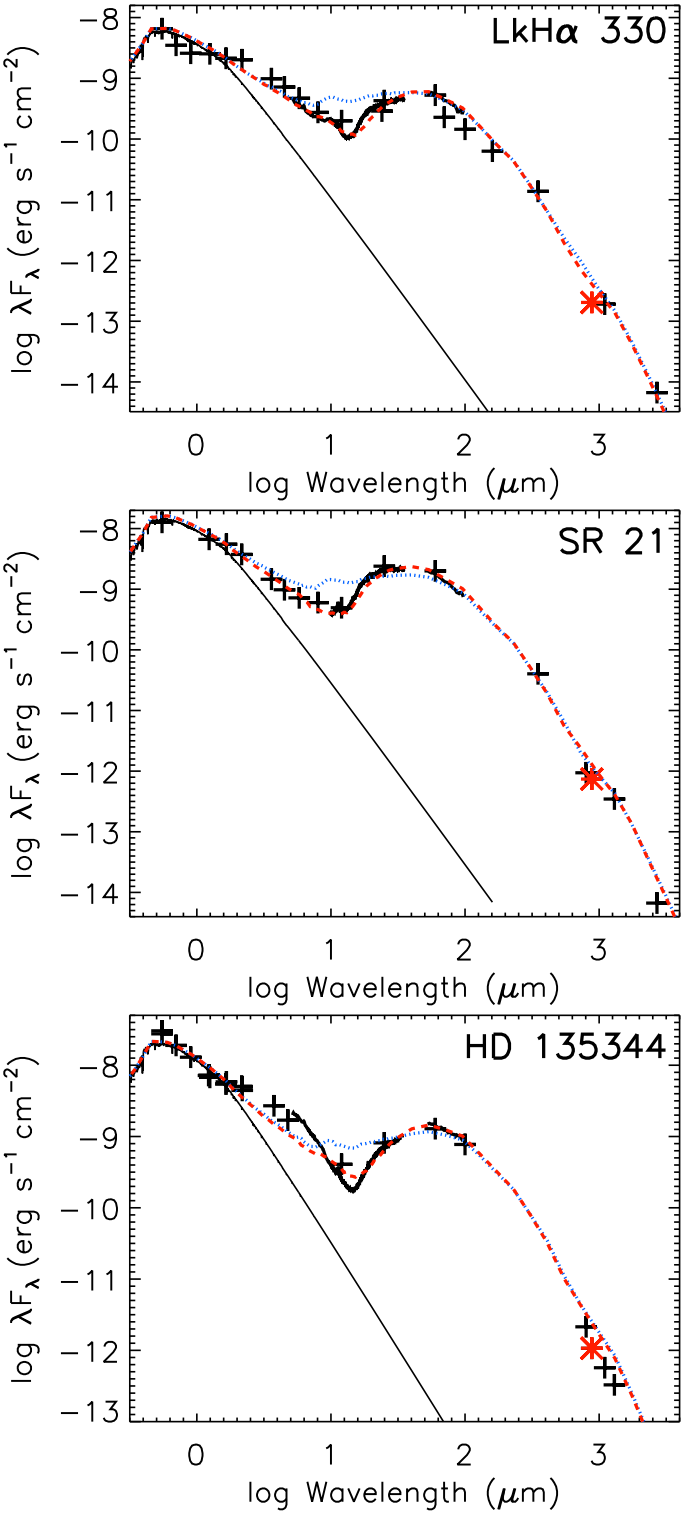

Figure 3.5 Model fits to the SEDs of LkHα 330 (top), SR 21 (middle) and HD 135344B (bottom). The models used to fit the images (dashed red line) are overlaid on the photometry (crosses) and IRS spectra (black line), confirming that the models fit the SEDs as well as the images. The dotted blue line is the equivalent model with no hole and the solid black curve is the stellar photosphere. The SMA total fluxes have been placed in the SED as a red star and are all consistent with previous photometry.

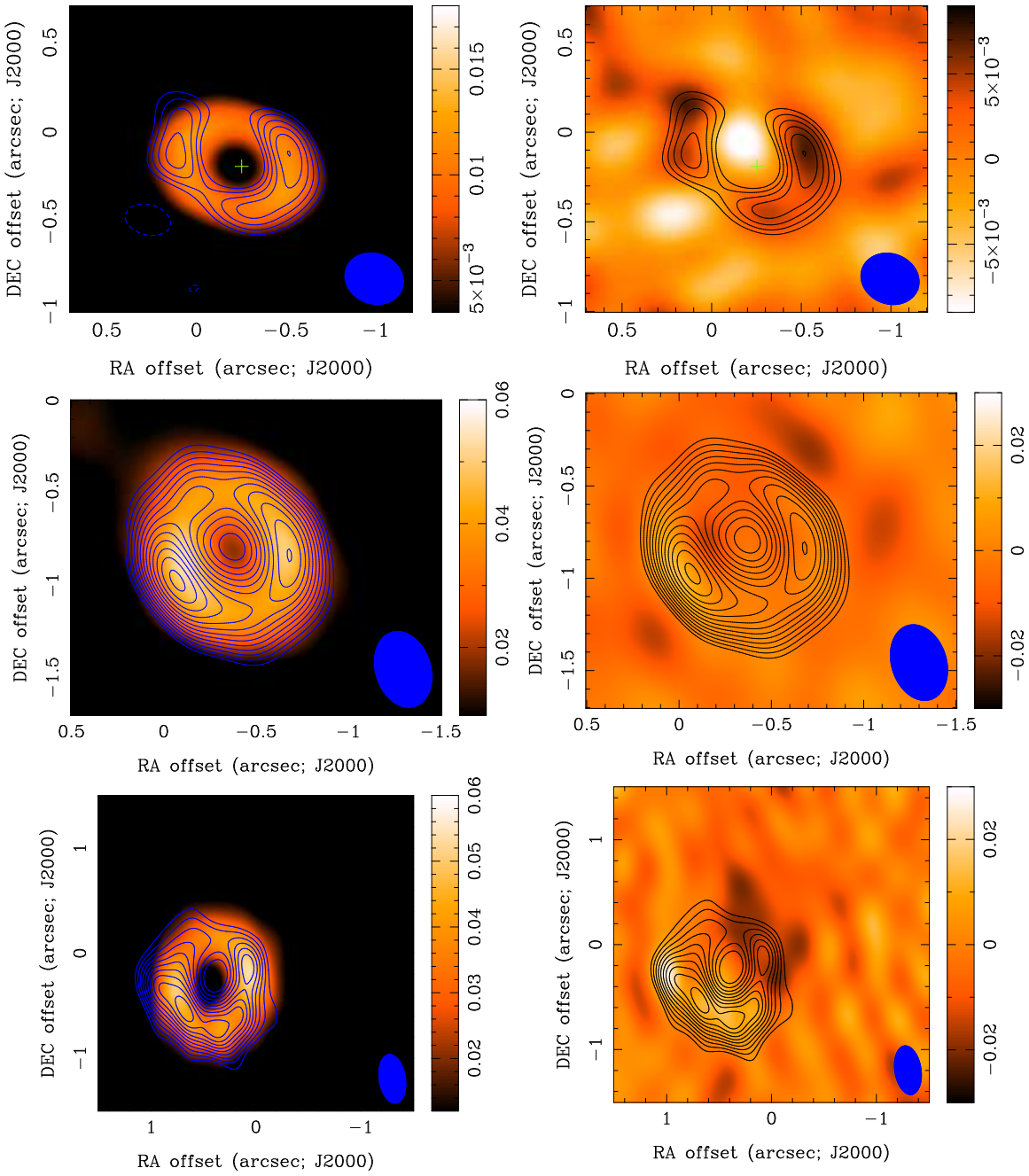

Figure 3.6 On the left are the models of LkHα 330 (top), SR 21 (middle) and HD 135344B (bottom) in color overlaid with 1-sigma contours from the data, beginning at 3-sigma. The beams are in the lower right corners. The model determines the hole radii to be 40 AU for LkHα 330, 27 AU for SR 21 and 37 AU for HD 135344B. On the right are the residuals when the model is subtracted from the data. Dark regions are areas where the model underproduces flux and light regions are areas where the model overproduces flux. The scales are set such that the extremes of the residual contours are 50% of the peak flux.

The gap is represented in the model by three parameters: both an inner and an outer gap radius and a density reduction factor. The best fit model was found by performing a χ^2 minimization on the inner and outer gap radii to find the best fit to the SED (see Brown et al. 2007 for more detail). This model was then compared to the image to check the validity of the SED interpretation. The SED best fit model matched the image remarkably well, lending confidence to current SED interpretation and modeling. Both the image and the SED indicate that the gap in the LkHα 330 disk has an outer radius of 40 AU. HD 135344B has a hole radius of 37 AU, while SR 21 has the smallest hole with a radius of 27 AU. The SMA images places no constraint on the inner gap radius, but the SEDs require an inner boundary on the gaps of $\sim$1 AU. Within our solar system, this gap corresponds to the area between Earth's orbit and distances just beyond Pluto's orbit.

3.4.1 Gap edge

In order to investigate the abruptness of the transition, a gap edge was introduced so that the density reduction rises logarithmically over a range of radii, $R_{\rm Edge}$, around the outer gap radius. Figure 3.7 shows the effects of different values of $R_{\rm Edge}$ on the amplitude seen at different (u,v) distances and also illustrates that the effect of this parameter is different from making the hole larger or smaller. The boundary between hole and outer disk is very abrupt in LkHα 330. This modeling confirms that the data are consistent with a step function. The transition region between the hole and the outer disk can be no larger than 5 AU. Such a steep transition is more consistent with gravitational instability than a more gradual process such as dust settling and coagulation.

On the other hand, both HD 135344B and SR 21 have much shallower slopes in density reduction. Gap edges of up to 15 AU adequately fit the data. This indicates a more gradual change in the disk structure which is less consistent with a steep wall as in D'Alessio et al. (2005).

3.4.2 Density contrast

The LkHα 330 hole is largely empty of dust, and the intensity contrast between the hole and the outer disk is large, indicating a similarly large mass surface density contrast. The best fit models for all three disks have density reductions of 1000 within the hole. In the LkHα 330 disk, this corresponds to 3.1×10^{-5} $M_\odot$ of material, compared to less than 1.3×10^{-4} $M_\odot$ derived from the image. For comparison, the model without the hole contains some 0.01 $M_\odot$ of material within the same region. SR 21 and HD 135344, with their more gradual gap edges, have less well defined

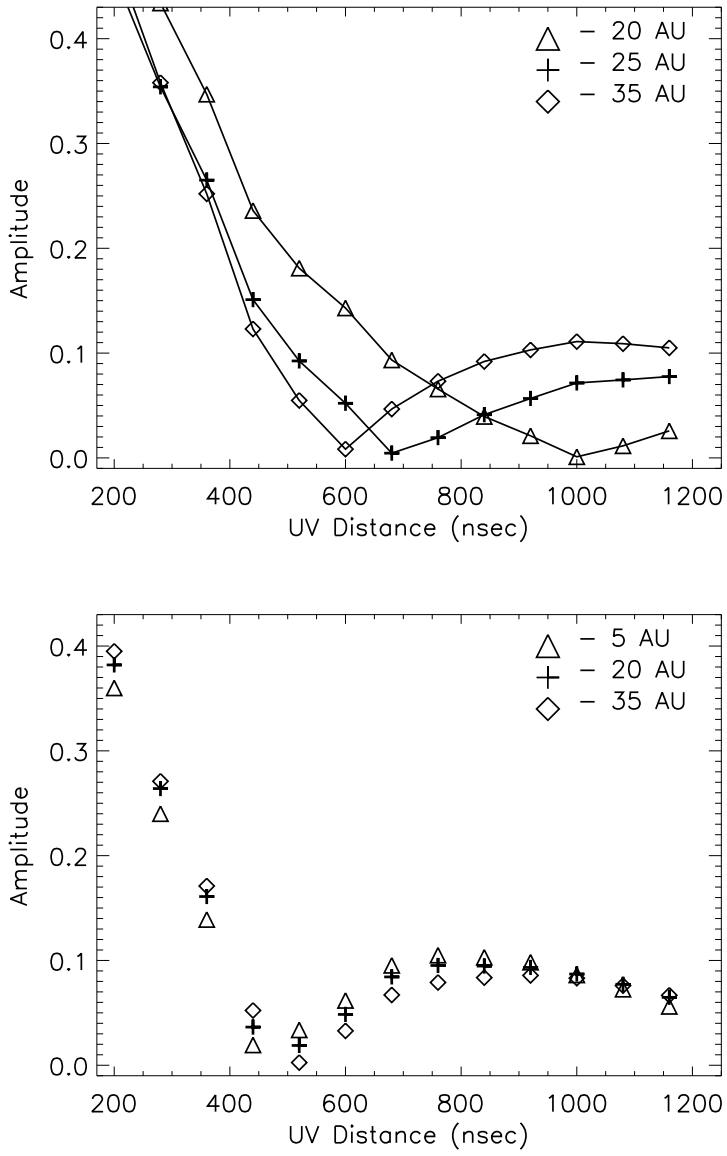

Figure 3.7 (top) Changes to the (u,v) amplitude with a variety of hole outer radii. (bottom) Effects of different sizes of R_{Edge} on the (u,v) amplitude diagram of a disk with a 37 AU hole. The effect of R_{Edge} is different than making the hole larger or smaller.

density contrasts and more material within the holes. Limits on the amount of material in the hole are 3.9 $\times$ 10^{-5} $M_{\odot}$ and 6.8 $\times$ 10^{-5} $M_{\odot}$, respectively. All the models still require a ring of matter close to the star needed to fit the near-IR excess.

3.4.3 Asymmetries

The most prominent asymmetry in the images is due to the inclination of the disks. The edges where more dust is in the line-of-sight are brighter, creating two bright regions along the major axis. However, other significant asymmetries remain which cannot be explained by an axisymmetric disk (see Figure 3.6). Such asymmetries would be expected from gravitational perturbation caused by a large planet or binary companion. For planetary companions of sufficiently low mass, some disk gas is expected to be transported across the gap while the dust transport is strongly inhibited (Alexander & Pringle 2007). In order to rule out close companions, deep infrared AO searches with 8-10m class telescopes will be necessary.

The disk around HD 135344B is the most asymmetric, so much so that modeling with an axisymmetric disk can never provide a good fit. The vast majority of the disk material lies to the southwest, with a cleared region in the ring to the north (see Figure 3.2).

3.4.4 Inner material

While the SMA images provide a large amount of information about the outer edge of the hole, information regarding the structure close to the star must come from other sources. The presence of material close to the star, making the density reduction a gap rather than a hole, places constraints on many gap producing processes. While the only indications of dust close to the star are the 1-10 μm excesses, we have two additional indications that there is gas close to the stars. First, LkHα 330 and HD 135344B display H Balmer α emission, with equivalent width measurements ranging from 11 to 20 Å (Fernandez et al. 1995, Cohen & Kuhi 1979), and so are still accreting gas. Second, emission from warm (800 - 1000 K) gas is seen in the 4.7 μm v=1$\rightarrow$0 rovibrational emission lines of CO (see Chapter 4). This molecular gas must be close to the star to reach such temperatures.

3.5 Discussion

We have directly imaged large inner gaps in three young protoplanetary disks. The observed sizes are in excellent agreement with those found through SED fitting. Model images, also produced by

the 2D radiative transfer code, fit the data well, although the asymmetry of the HD 135344 disk poses problems with the axisymmetric model used. The limits from the SMA images on the amount of material within the holes are also in agreement with the models and reveal a significant reduction in dust in the inner regions. The gap edge is very abrupt in the LkHα 330 disk with a thousand-fold increase in dust density occuring over less than 5 AU.

One proposed process for quickly clearing the inner disk region is photoevaporation (Clarke et al. 2001, Alexander et al. 2006). An inner hole occurs when the photoevaporation rate driven by the ionizing flux from the central star matches the viscous accretion rate. However, this condition is only effectively fulfilled when accretion rates are low and would result in no gas or dust close to the star for gap radii of several tens of AU. Photoevaporation is thus unlikely to be responsible for the 27-40 AU radiii gaps observed in the LkHα 330, HD 135344B and SR 21 disks.

An alternative explanation to physical removal of the dust is that it has grown beyond the size at which it efficiently radiates as a blackbody so that it no longer emits strongly in the mid-IR and submillimeter (Tanaka et al., 2005). Within any realistic distribution of dust grain sizes, even a minimum grain diameter of 50 μm significantly overproduces the flux in the 10 μm region with no density reduction. Thus, grain growth to very large sizes with little fragmentation in collisions is needed for this scenario to be relevant for these transitional disks. The sharp cutoff in dust mass surface density between the inner and outer disk in LkHα 330 is also difficult to reconcile with dust coagulation models.

3.6 Conclusions

To summarize, LkHα 330, HD 135344B and SR 21 present dramatic cases of disks evolving from the inside out rather than smoothly throughout the disk as would be expected in alpha-viscosity models of disk evolution. The large gaps are largely empty of dust but gas does remain, and the outer edge of the gaps rise steeply. Importantly, the good agreement of both data and model lends confidence to current interpretations of SEDs with significant dust emission deficits being due to inner holes in disks. Further SED-based searches can therefore be expected to yield numerous additional candidates that can be examined at high spatial resolution. Ultimately, in such studies it will be critical not only to image the dust but to provide estimates of the gas:dust ratios in the outer and inner disk if the different possible gap creation scenarios are to be disentangled. A combination of spatially resolved imaging, ultimately with the Atacama Large Millimeter Array (ALMA), and

high resolution spectroscopy to trace the gas content will provide future understanding of these interesting objects.

Chapter 4

Searching for gas inside the gap with Keck/NIRSPEC

Abstract

Cold disks often show signs of accretion onto their central stars despite evidence of dust clearing over radii of $\sim$1 to several tens of AU, indicating that the dissipation of dust may not be strongly coupled with gas dissipation. Therefore, observations of gas as well as dust are necessary to trace protoplanetary disk evolution. The terrestrial disk region can be probed using high dispersion near-infrared through mid-infrared rovibrational spectroscopy of abundant molecules. In this chapter, I present 4.7 μm CO v=1 $\rightarrow$ 0 R=25,000 spectra of 10 transitional disks using the NIRSPEC echelle spectrometer at the Keck II telescope and compare these with a sample of 38 non-transitional disks. 64% of the cold disks do have CO within the inner 1 AU, which provides limits on the number of disk holes that are formed by photoevaporation. The cold disks show cooler excitation temperatures than do non-transitional disks at similar radii.

4.1 Introduction

The inner regions of protoplanetary disks (R $<$ 5 AU) are likely to be the most active regions of planet formation and hold the key to understanding the formation of solar systems like our own. Unfortunately, imaging studies of the terrestrial regions of disks are challenging due to small size scales, less than 10 mas at the typical 140 pc distance of the nearest star forming regions, and due to the high contrast needed at optical and near-infrared wavelengths to reject light from the central star. However, high resolution spectroscopic line studies can probe warm molecular emission within this region by using high velocity resolution rather than milli-arcsecond spatial resolution.

The most abundant gas within protoplanetary disks is molecular hydrogen, which initially appears an obvious observational choice. However, at the few 100 K temperatures found in the inner 0.1-50 AU of disks, H_2 mainly populates its ground vibrational and lowest few rotational levels. It also has small transition probabilities due to its lack of an electric dipole moment. In regions where temperatures are high enough to populate the first vibrational state, the column density is often too high to achieve sufficient line-to-continuum contrast against dust blackbody emission. Pure rotational lines of H_2 have excitation temperatures of $\gtrsim$100 Kl, but only a few lines are observable from the ground. The Infrared Space Observatory (ISO) provided the first detections of these lines from disks around Herbig Ae and T Tauri stars but using large apertures (Thi et al., 2001). However, these detections were not confirmed by subsequent higher spatial resolution ground-based observtations (Richter et al. 2002, Sako et al. 2005). Spitzer has again allowed space-based observations of molecular hydrogen but with much better sensitivity and spatial resolution. Even so, lines have only been detected from about 8% of young disks observed, many of which have known molecular outflows (Lahuis et al., 2007). Florescent excitation of the rovribrational hydrogen lines has also been successfully observed in a handful of disks (Bary et al., 2003). However, to observe thermally excited gas from ground-based observatories, a different tracer must be found.

A complementary diagnostic of gas in terrestrial regions is CO. Carbon monoxide is the most abundant molecule after molecular hydrogen and at inner disk temperatures should be entirely in the gas phase. CO emission is seen ubiquitously from stars with optically thick inner disks (Brittain et al. 2007, Najita et al. 2003) and can be excited either thermally or via infrared (vibrational) or UV (electronic) fluorescence (Blake & Boogert, 2004). In an optically thick passive disk, line emission is expected from the disk atmospheres due to the vertically increasing temperature gradient. Regions of low dust optical depth may also produce strong line emission even as the continuum is suppressed,

Table 4.1. Summary of Keck/NIRSPEC transitional disk observations

Source	^{12}CO v=1→0	^{13}CO v=1→0	^{12}CO v=2→1	Pf β	Hu ϵ	Notes
CoKu Tau 4	n	n	n	n	n	Hole of 10 AU[1]
DM Tau	n	n	n	y	y	Inner hole of 3 AU [2]
GM Aur	y	n	n	y	y	Inner hole of 24 AU[2]
HD 135344B	y	n	n	y	y	Gap from 0.55 - 55 AU[3]
LkHα 330	y	n	n	y	t	Gap from 0.8 - 35 AU[3]
SR 21	y	y	y	y	t	Gap from 0.35 - 20 AU[3]
SU Aur	e/a	n	n	y	n	Gap from 0.02 - 5 AU[4]
T Cha	n	n	n	-	-	Gap from 0.2-15 AU[3]
TW Hya	y	n	n	y	y	Inner hole of 4 AU[5]
UX Tau	y	n	n	y	y	Cold disk SED[6]

[a]y - yes, t - tentative, n - no, w - weak, e/a - emission and absorption

[b1] - Forrest et al. (2004), [2] - Calvet et al. (2005), [3] - Brown et al. (2007), [4] - Marsh & Mahoney (1992), [5] - Calvet et al. (2002), [6] - Furlan et al. (2006)

increasing the line-to-continuum contrast.

Infrared spectrophotometry provides tantalizing glimpses that a small set of disks, "cold disks," have cleared the dust from the terrestrial region while still maintaining material further out in the disk (Calvet et al. 2002, Brown et al. 2007). Questions remain about the corresponding gas evolution. Surprisingly, many cold disks still show signatures of accretion, mainly Balmer Hα emission, implying that gas is present close to the star. Fluorescent H_2 emission has been seen from the surface of the TW Hya disk (Herczeg et al., 2006), while CO has also been seen from the interiors of transitional disks around GM Aur and TW Hya (Rettig et al. 2004, Salyk et al. 2007). On the other hand, most completely optically thin disks show no CO emission (Brittain et al., 2007). The conditions of these disks provide observational constraints on theories of disk evolution and planet formation, and so it is important to expand the presently small sample of transitional disks studied in gas tracers.

4.2 Observations

We used the cross-dispersed echelle spectrograph NIRSPEC on Keck II (McLean et al., 1998) to obtain high resolution (R=25,000) spectra of the 4.7 μm CO v=1→0 fundamental emission band

of over 100 low and intermediate mass stars. The data were collected over a period of 5 years from 2002 to 2007. The P-branch CO rovibrational lines cover the region 4.65-5.15 μm. Two grating settings were observed covering R(0) to P(12) (4.65-4.78 μm) in the shorter wavelength echelle order and P(30)-P(40) (4.96-5.1 μm) in the longer wavelength order. We have not observed the intermediate lines, in part because the 4.78-4.96 μm wavelength region contains many strong atmospheric lines and because the observed lines are typically sufficient to characterize the CO excitation and column density.

Strong thermal background ($\sim$300 K) from the Earth's atmosphere dominates M-band spectra. To allow background subtraction, a telescope nod pattern of ABBA was used, moving 6$''$ away from the center in each direction along the 0.$''$43x24$''$ slit. Each position was observed for 30-60 seconds to minimize atmospheric variation and ensure good background subtraction.

Calibration was done using IDL routines (see Boogert et al. 2002 for additional details). First, a nod pair of spectra were differenced to remove the thermal background. The 2D spectra were then linearized and added along the slit direction to create 1D spectra. The 1D spectra were aligned and wavelength calibrated using the prevalent atmospheric lines. In order to remove atmospheric absorption and instrumental features, a standard star, preferably of A spectral type due to their lack of stellar lines near 5 μm, was divided from the source spectrum. Residal stellar features from the standard such as the continuum shape and hydrogen absorption were removed with a Kurucz atmosphere model. Wavelengths with significant telluric absorption from the atmosphere (transmission of $\sim$40% - 65%) were removed. By observing at periods of positive and negative Doppler shifts due to the Earth's orbital motion, complete wavelength coverage is possible. Using these techniques, flux-calibrated spectra with signal-to-noise ratios approaching the shot-noise limit can be obtained.

4.3 Data

We observed 48 stars that show various degrees of CO gas emission. Sources which have SEDs indicative of dust clearing and the inferred hole sizes are listed in Table 4.1. SR 21 also clearly shows emission lines from ^{13}CO v=1$\rightarrow$0 and ^{12}CO v=2$\rightarrow$1. The H I lines Pf β (4.6538 μm) and Hu ϵ (4.6725 μm), which are accretion diagnostics, also lie in this region. The Pf β line is from a lower energy state than the Hu ϵ line and is generally stronger. The majority of the sources show the Pf β line with a range of intrinsic fluxes, which does not seem to correlate with CO strength. This line is

clearly variable, as is common for accretion tracers (Cohen & Kuhi, 1979), in several of the sources including TW Hya. The Hu ϵ line is weaker and also blended with the ^{12}CO v=1→0 P(2) line, so it can be difficult to determine its strength accurately.

The 4.7 μm CO emission is rovibrational in nature and contains information on both the spatial and temperature structure of the disk (e.g. Najita et al. 2003, Blake & Boogert 2004). It is sensitive to a range of gas energies due to the many rotational levels within the vibrational states. The line strengths of the rotational lines correlate with the populations of the different energy rotational levels, allowing the gas excitation to be used to trace the disk temperature profile. The lines are Doppler broadened due to the approximately Keplerian rotation of the disk. At the high resolution (R=25,000) of NIRSPEC, the disk emission is spectrally resolved unless the disk is nearly face-on, and the line profile can thus be used to locate the gas within the disk.

A sample of 10 transitional disks were examined. Out of these only three, CoKu Tau 4, DM Tau and Hen 3-600, do not show CO v=1→0 emission (see Figure 4.3). The southern transitional disk T Cha also does not show any CO emission when examined with VLT/CRIRES (Pontoppidan, priv. comm.). The remaining seven all show CO emission of varying strengths, providing a detection rate of 64% for the full sample of 11 sources (see spectra in Figures 4.1 and 4.2).

4.4 Analysis

The first step in analyzing the spectra was to determine the strength and shape of the individual rotational lines. Each transition was fit with a Gaussian and normalized to a clean continuum (see Table 4.2 for a sample of the output data). While this fitting procedure overcame problems with missing sections of lines due to atmospheric absorption, not all lines were Gaussian in shape so errors in line flux are higher for those lines. Some lines are also blended with Pf β, Hu ϵ, or lines from other CO isotopes or vibrational states. Thus, while much of the analysis was automated due to the large sample size, the line fitting results were all examined by eye, and only the cleanest lines were retained for further analysis.

We have chosen to model the emission lines with a simple uniform slab model due to the number of uncertainties associated with a more complex 2D disk model such as that outlined in Chapters 2 and 3. In this slab model, derived in §4.5, the gas lies in a flat disk characterized by three variables: a single temperature ($T_{\rm rot}$), column density ($N_{\rm CO}$), and solid angle (Ω) (expressed as the emitting area, $A_{\rm emit}$ such that $A_{\rm emit} = 4\pi d^2 \Omega$, where d is the distance). It is important to note that the temperature is

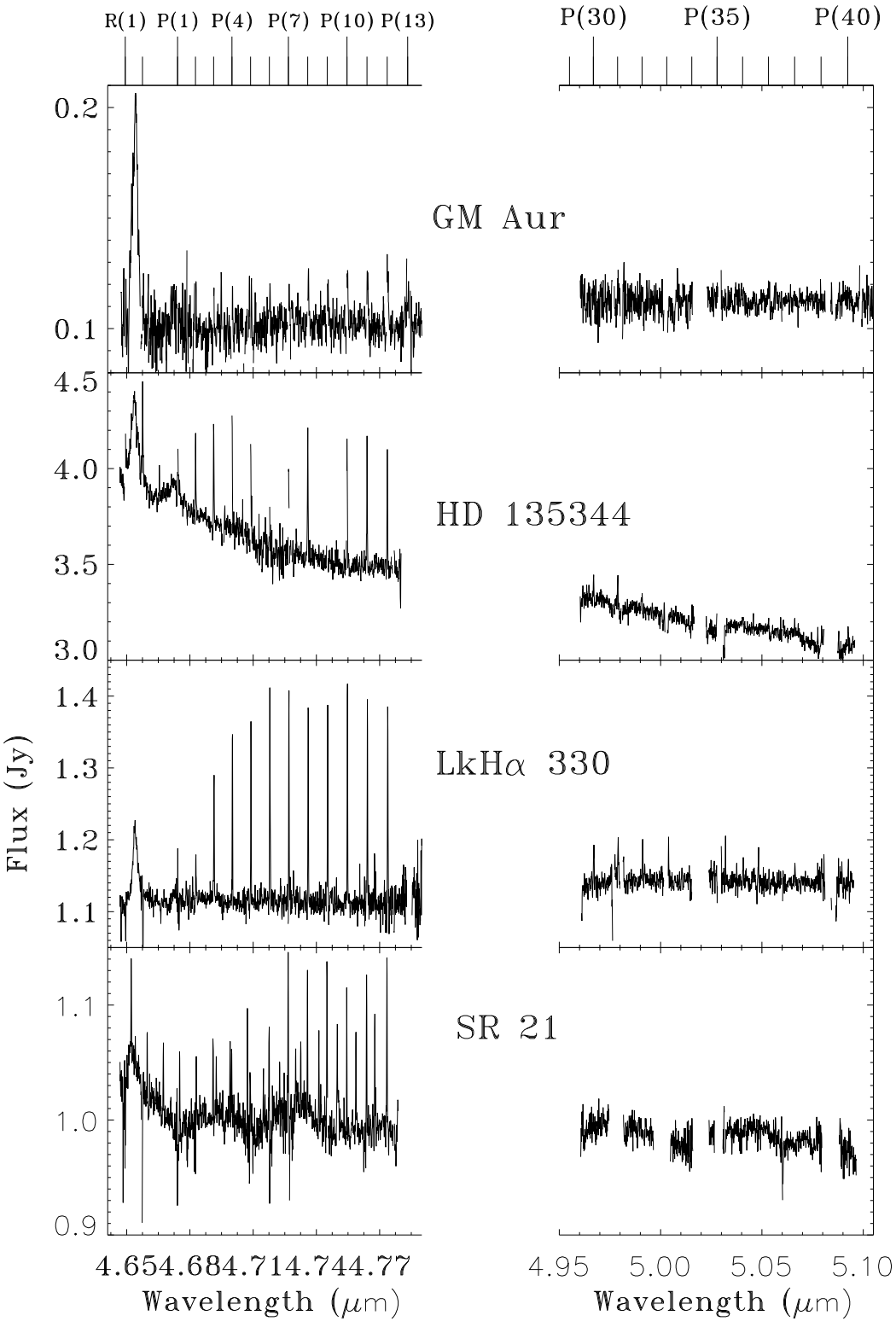

Figure 4.1 An overview of the NIRSPEC spectra of the four cold disks, GM Aur, HD 135344, LkHα 330 and SR 21 for which high resolution SMA images are available.

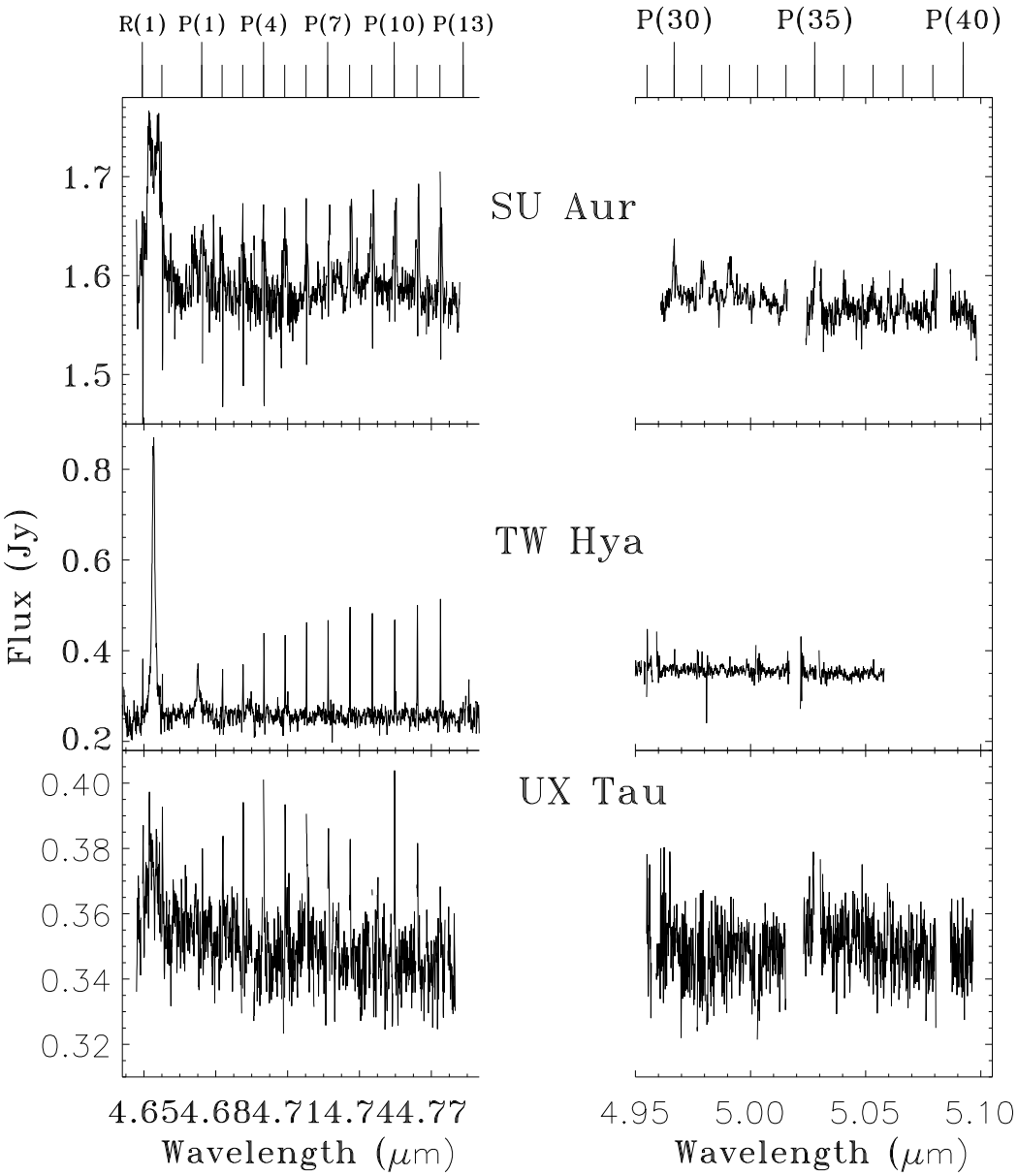

Figure 4.2 Continuation of Figure 4.1. NIRSPEC spectra of the three cold disks, SU Aur, TW Hya and UX Tau A.

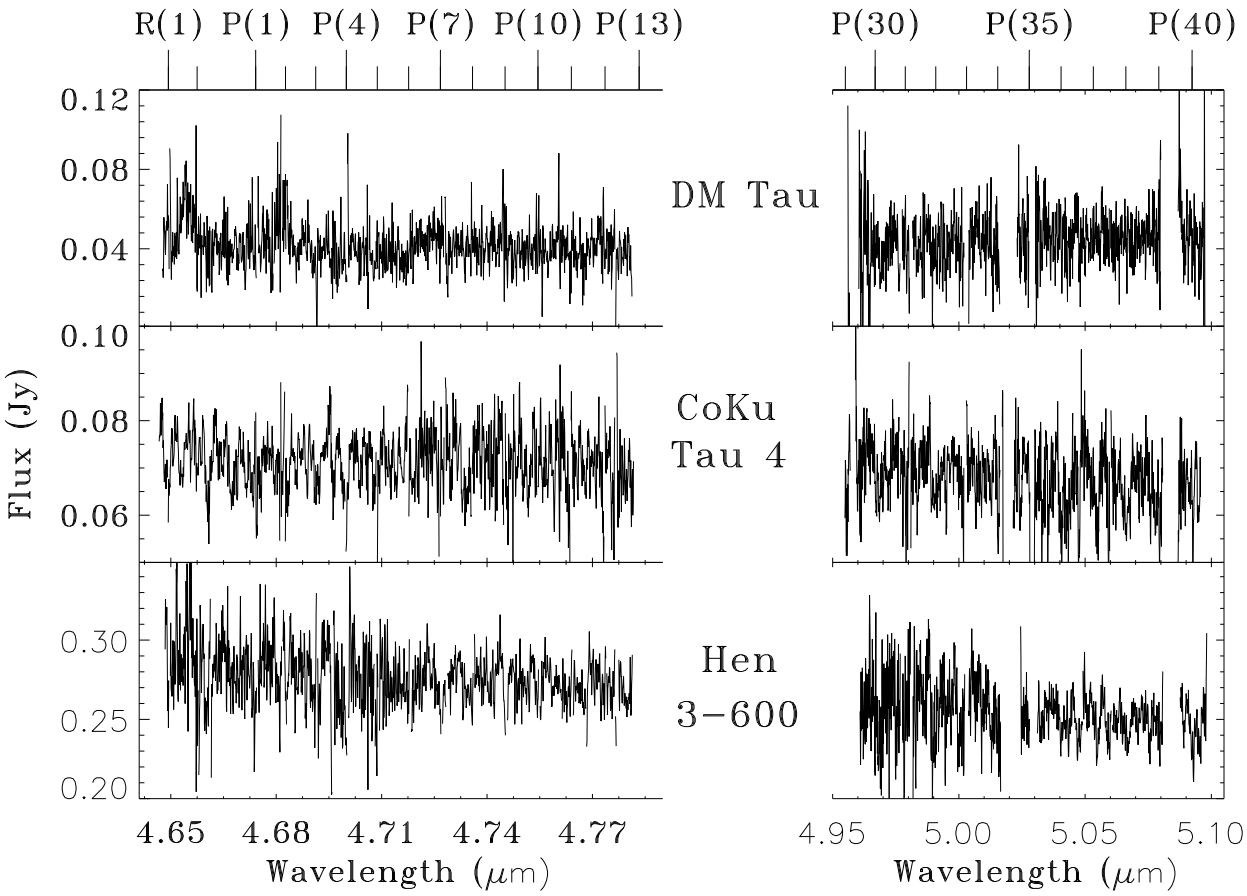

Figure 4.3 NIRSPEC spectra of the transitional disks from which CO emission was not detected (DM Tau, CoKu Tau 4 and Hen 3-600). Only DM Tau shows evidence of accretion through the Pf β line at 4.65 μm as well as Hu ϵ emission 4.67 μm.

Table 4.2. Observed ^{12}CO v=1-0 Line Parameters for HD135344B

Transition ν = 1 - 0	Center km/s	FWHM km/s	Line Flux Jy	Notes*
P(40)	13.7	11.2	0.0169 (0.029)	0
P(39)	4.76	22.2	0.0181 (0.026)	0
P(38)	3.99	18.8	0.0126 (0.015)	0
P(37)	-1.12	28.6	0.0184 (0.026)	0
P(36)	9.58	24.4	0.0104 (0.027)	0
P(35)	5.60	24.1	0.0214 (0.027)	0
P(32)	-5.78	40.4	0.0300 (0.025)	0
P(31)	3.40	18.7	0.0269 (0.035)	0
P(30)	4.34	22.0	0.0155 (0.033)	0
P(12)	7.87	28.8	0.0850 (0.043)	1
P(11)	4.62	32.2	0.0925 (0.030)	1
P(10)	-0.688	18.2	0.0590 (0.025)	1
P(9)	6.93	22.3	0.117 (0.19)	1
P(8)	4.45	38.4	0.0921 (0.021)	1
P(6)	9.94	24.2	0.0883 (0.092)	1
P(5)	-2.78	13.2	0.0405 (0.049)	1
P(3)	5.80	28.2	0.0689 (0.060)	1
P(1)	-3.35	22.4	0.0213 (0.037)	1
R(0)	7.72	49.8	0.0532 (0.038)	1
R(1)	12.3	28.0	0.0317 (0.038)	1

*0 indictes a good fit; 1 indicates that the line profile is incomplete due to an atmospheric line but a fit was obtained over the missing Doppler coverage.

not necessarily the thermal temperature of the gas as processes other than collisional excitation can drive CO v=1→0 emission. The optimal rotation diagram fit was found by minimizing the absolute χ^2 over a range of physically likely input rotation temperatures, CO column densities and emitting areas. Figure 4.4 shows the trends of each of these variables, where the two remaining (static) variables were set at the fixed values $T_{\rm rot}$ = 1250 K, $N_{\rm CO} = 10^{-3}$, or $A_{\rm emit}$ = 0.1 AU^2. Increasing any of the three variable leads to an increase in flux. Most of the slope changes are related to temperature. These three parameters are somewhat degenerate so a range of values can provide similar levels of goodness of fit. A sample set of chi-squared plots is shown in Figure 4.5 and confidence intervals are marked to demonstrate how the various parameters relate. The rotation diagrams with the optimal fit model are shown in Figure 4.7 and values are listed in Table 4.3 with transitional disks in the first section and classical disks in the second.

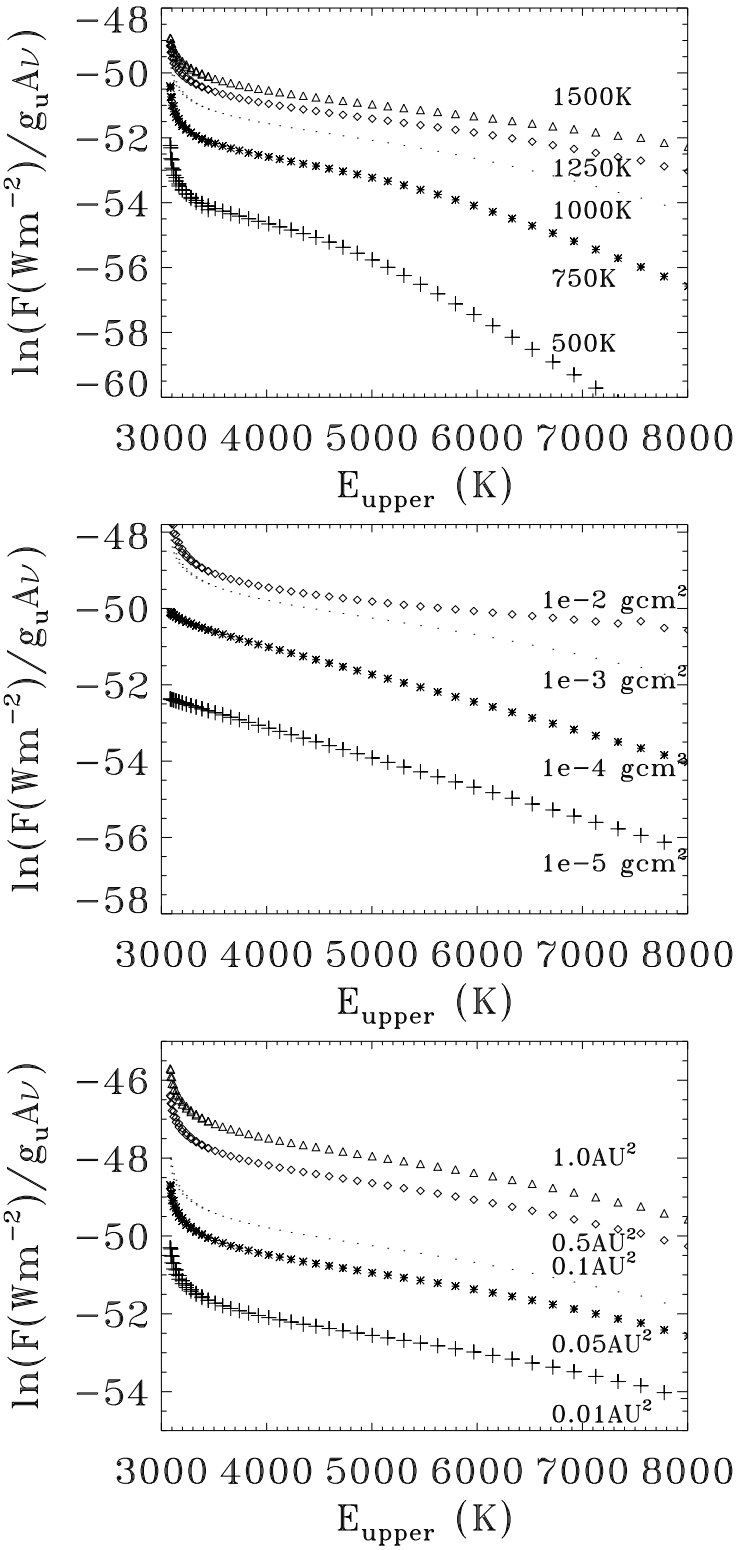

Figure 4.4 Effects of varying $T_{\rm rot}$ (top), $N_{\rm CO}$ (middle) and $R_{\rm emit}$ (bottom) in model where the parameters not varied are fixed at $T_{\rm rot}$ = 1250 K, $N_{\rm CO} = 10^{-3}$ and $A_{\rm emit} = 0.1AU$.

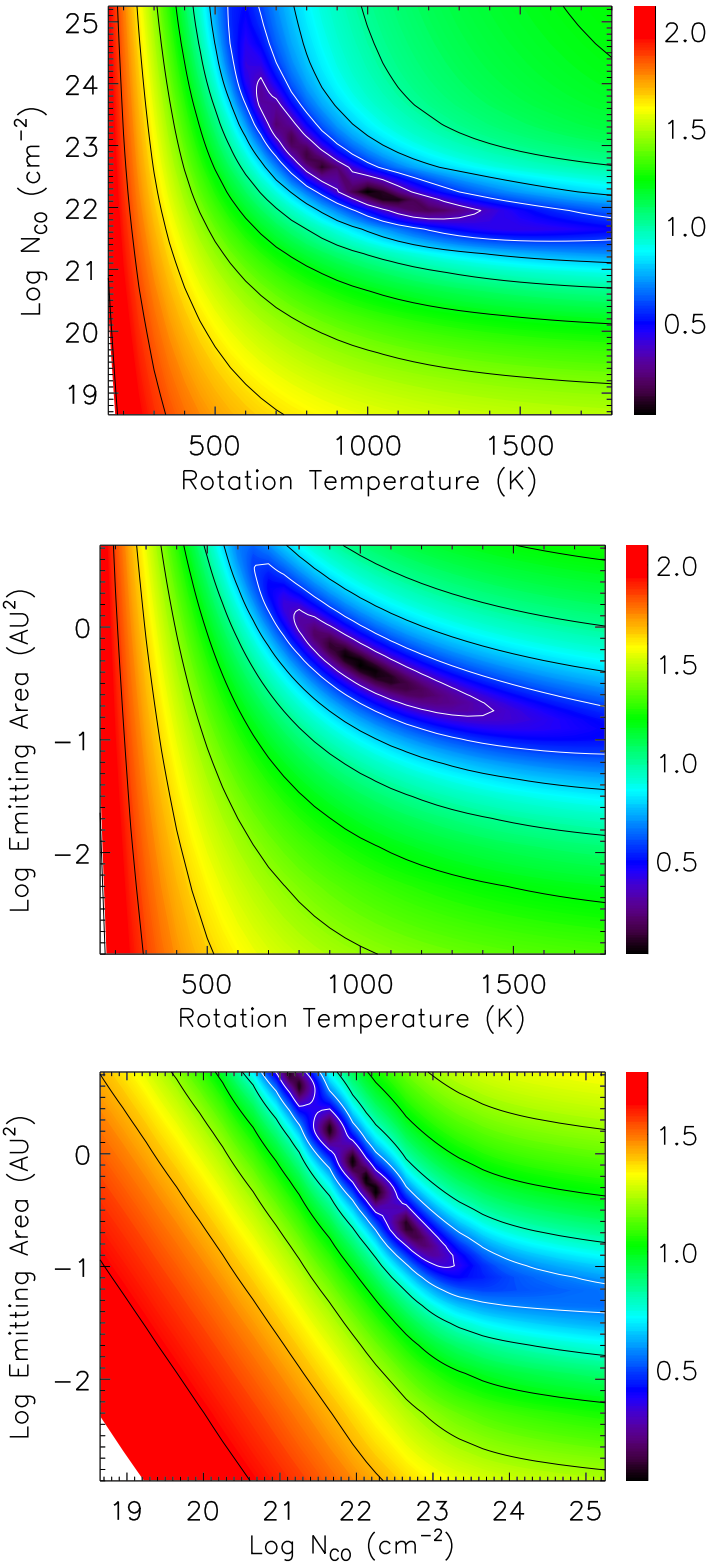

Figure 4.5 Log χ^2 plots for the LkHα 330 model. The parameters are degenerate causing a range of parameters to have good fits. Confidence intervals have been overlaid with 95% and 90% confidence in white and decreasing confidence levels in intervals of 5% in black.

Table 4.3. Summary of Keck/NIRSPEC rotation diagrams

Source	Rotation temperature (K)	CO column density (g cm^{-2})	Emitting area (AU^2)
GM Aur*	600.	5.0e-3	0.031
HD 135344B	950.	3.6e-4	0.031
LkHα 330	1000.	8.0e-5	0.45
SR 21*	550.	4.0e-3	0.15
SU Aur	800.	2.8e-3	0.080
TW Hya	800.	2.8e-4	0.020
UX Tau	1050.	4.8e-4	0.011
AB Aur	850.	8.4e-4	0.92
AS 205N	1600.	2.e-4	0.18
DoAr 44	1400.	2.4e-3	0.02
DF Tau	1150.	8.0e-3	0.15
DR Tau	1200.	1.0e-2	0.13
EC 82	1000.	9.6e-4	0.41
Elias 1	650.	5.2e-3	0.45
Elias 23	1250.	1.e-2	0.045
GG Tau	1800.	7.2e-4	0.011
GQ Lup	1350.	3.2e-3	0.062
HD 144432S	650.	4.8e-3	0.28
HD 163296	1350.	9.6e-4	0.08
HD 190073	600.	6.0e-2	3.1
IRAS 03301+3111	1450.	8.0e-3	0.08
LkHa 326	1750.	2.4e-3	0.02
LkHa 327A	1450.	3.2e-3	0.062
MCW 442	700.	6.0e-2	1.5
MWC 480	1400.	3.2e-3	0.08
MWC 758	900.	7.6e-4	0.66
PV Cep	800.	1.0e-2	4.7

Table 4.3 (cont'd)

Source	Rotation temperature (K)	CO column density (g cm^{-2})	Emitting area (AU^2)
RNO 90	1350.	3.2e-3	0.18
SR 4	1700.	8.8e-4	0.020
SR 9	1700.	2.8e-4	0.031
SR 13	1150.	9.2e-4	0.031
T Tau N	1800.	6.8e-4	0.15
UY AUR	1800.	8.E-4	0.031
VSSG 1	850.	8.0e-2	0.13
VV Ser	1450.	7.6e-4	0.13

*These values are upper limits.

4.5 Derivation of the equations in the CO thermal disk model

Beginning with the formal solution of the radiative transfer equation

$$I_\nu(\tau_\nu) = I_\nu(0)e^{-\tau} + \int_0^{\tau_\nu} e^{-(\tau_\nu - \tau_\nu')} S_\nu(\tau_\nu') d\tau_\nu', \tag{4.1}$$

where I_ν is the specific intensity, S_ν is the source function and τ_ν is the optical depth, we can write

$$I_\nu(\tau_\nu) = S_\nu + e^{-\tau}(I_\nu(0) - S_\nu) \tag{4.2}$$

provided the source function is constant.

In local thermal equilibrium (LTE), $S_\nu = B_\nu(T)$, which, in deriving the line fluxes, is the temperature of the gas. When the optical depth of the gas is zero, the only flux is from the dust continuum so $I_\nu(0) = B_\nu(T_{\rm dust})$. In this case

$$I_\nu(\tau_\nu) = B_\nu(T_{\rm gas}) + e^{-\tau}(B_\nu(T_{\rm dust}) - B_\nu(T_{\rm gas})), \text{ where } B_\nu(T) = \frac{2h\nu^3/c^2}{exp(h\nu/kT) - 1}. \tag{4.3}$$

The optical depth is defined to be the amount of absorption along the line of sight and can be written as

$$\tau_\nu(s) = \int_{s_0}^{s} \alpha_\nu(s') ds', \tag{4.4}$$

where s is the distance along the path and α_ν is the absorption coefficient, which defines the amount

of absorption at each point along the path.

The Einstein coefficients quantify the probability of transition between two energy levels and are defined as follows. The coefficient for spontaneous emission, A_{21}, is dependent solely on the properties of the upper state. The coefficients for absorption, B_{12}, and stimulated emission, B_{21}, depend both on the density of photons at frequencies around the transition frequency, ν_0, and the properties of the states. In thermodynamic equilibrium, where the photon density equals that from a blackbody at all frequencies, the Einstein relations dictate that

$$g_1 B_{12} = g_2 B_{21} \tag{4.5}$$

$$A_{21} = \frac{2h\nu^3}{c^2}. \tag{4.6}$$

The absorption coefficient, corrected for stimulated emission, is therefore

$$\alpha_\nu = \frac{h\nu}{4\pi}\phi(\nu)(n_1 B_{12} - n_2 B_{21}). \tag{4.7}$$

The $\frac{h\nu}{4\pi}$ coefficient is due to each atom contributing energy $h\nu_0$ isotopically, or distributed over 4π solid angle, while the normalized line profile function, $\phi(\nu)$, peaks at ν_0.

The detailed balance relationship specified in the first Einstein relation means that

$$\alpha_\nu = \frac{h\nu}{4\pi}\phi(\nu) n_1 B_{12}(1 - \frac{g_1 n_2}{g_2 n_1}), \tag{4.8}$$

and from the second Einstein relation, we find that

$$\alpha_\nu = \frac{h\nu}{4\pi}\phi(\nu) n_1 \frac{g_2}{g_1}\frac{c^2}{2h\nu^3}A_{21}(1 - \frac{g_1 n_2}{g_2 n_1}). \tag{4.9}$$

In LTE, the population balance between the two energy levels is simply

$$\frac{n_1}{n_2} = \frac{g_1}{g_2} exp(\frac{h\nu}{kT}), \tag{4.10}$$

so eq. (4.9) may be written as

$$\alpha_\nu = \frac{c^2}{8\pi\nu^2}\phi(\nu)\frac{g_2 n_1}{g_1}A_{21}(1 - exp(-\frac{h\nu}{kT})). \tag{4.11}$$

We know the equilibrium ratio of the population of an energy level to the total population is

terms of the partition function, q,

$$n_1 = n_{\rm CO}\frac{g_1 exp(-\frac{E_1}{kT})}{q}. \tag{4.12}$$

Now the absorption coefficient is

$$\alpha_\nu = \frac{g_2 c^2}{8\pi\nu^2}\phi(\nu)\frac{n_{\rm CO}}{q_{\rm CO}}exp(-\frac{E_1}{kT})A_{21}(1-exp(-\frac{h\nu}{kT})). \tag{4.13}$$

Here the line profiles are assumed to be Gaussian such that

$$\phi(\nu) = \frac{1}{\sqrt{2\pi}\Delta\nu_\theta}exp(-\frac{(\nu-\nu_{Doppler})^2)}{2\Delta\nu_\theta^2}), \tag{4.14}$$

and to change the line profile from frequency to velocity, $\Delta\nu/\nu = {\rm V}/c$, so

$$\phi({\rm V}) = \frac{c}{\sqrt{2\pi}\nu\Delta{\rm V}_\theta}exp(-\frac{({\rm V}-{\rm V}_{Doppler})^2)}{2\Delta{\rm V}_\theta^2}). \tag{4.15}$$

Plugging this particular form into the expression for the absorption coefficient gives

$$\alpha_\nu = \frac{g_2 c^3}{8\pi\sqrt{2\pi}\Delta{\rm V}_\theta\nu^3}\frac{n_{\rm CO}}{q_{\rm CO}}A_{21}exp(-\frac{({\rm V}-{\rm V}_{Doppler})^2)}{2\Delta{\rm V}_\theta^2})exp(-\frac{E_1}{kT})(1-exp(-\frac{h\nu}{kT})). \tag{4.16}$$

Finally, the expression can be incorporated back into the expression for specific intensity and integrated along the line of sight, namely

$$I_\nu(\tau_\nu) = B_\nu(T_{\rm gas}) + e^{-\int_{s_0}^{s}\alpha_\nu(s')ds'}(B_\nu(T_{\rm dust}) - B_\nu(T_{\rm gas})), \tag{4.17}$$

to derive flux from the specific intensity

$$F = \int I_\nu cos\theta d\Omega. \tag{4.18}$$

Since the model is uniform, the integral is particularly simple and

$$\int_{s_0}^{s}\alpha_\nu(s')ds' = \frac{g_2 c^3}{8\pi\sqrt{2\pi}\Delta{\rm V}_\theta\nu^3}\frac{n_{\rm CO}\times s}{q_{\rm CO}}A_{21}exp(-\frac{({\rm V}-{\rm V}_{Doppler})^2)}{2\Delta{\rm V}_\theta^2})exp(-\frac{E_1}{kT})(1-exp(-\frac{h\nu}{kT})), \tag{4.19}$$

where $n_{\rm CO}\times s = N_{\rm CO}$ where $N_{\rm CO}$ is the column density (cm^{-2}) rather than the density (cm^{-3}).

Here, only the gas is fitted so

$$F = \int B_\nu(T_{\rm gas})(1-e^{-\int_{s_0}^{s}\alpha_\nu(s')ds'})cos\theta d\Omega, \tag{4.20}$$

and since the model is uniform integrating over Ω gives $\Omega = A_{\rm emit}/4\pi d^2$. Thus,

$$F = \frac{2h\nu^3/c^2}{exp(h\nu/k\mathbf{T})-1}\frac{\mathbf{A}_{\rm emit}}{4\pi d^2}(1-exp(-\frac{A_{21}g_2c^3}{8\pi\sqrt{2\pi}\Delta V_\theta\nu^3}\frac{\mathbf{N}_{\rm CO}}{q_{\rm CO}}e^{-\frac{(V-V_{Doppler})^2)}{2\Delta V_\theta^2}}e^{-\frac{E_1}{k\mathbf{T}}}(1-e^{-\frac{h\nu}{k\mathbf{T}}}))), \tag{4.21}$$

and this is the equation we use to determine the excitation temperature, emitting area and column density of CO. The Einstein A coefficients, upper state energies and transition frequencies needed are taken from the HITRAN molecular database (Rothman et al., 2005).

4.6 Correlations of CO with stellar parameters

Since the central star is the driving force in the system, providing the energy needed to excite the gas, correlations between CO properties and stellar parameters might be expected. Therefore, I compared the three derived model properties of rotation temperature, column density and emitting area with various stellar properties from the literature including mass, luminosity, accretion rate, and spectral type (see Figures 4.12 to 4.16). The linear Pearson correlation coefficients are in Table 4.4. These coefficients, *r*, are equal to

$$r = \frac{\Sigma(x_i-\overline{x})(y_i-\overline{y})}{(n-1)\sigma_x\sigma_y}, \tag{4.22}$$

where $\overline{x}$ and $\overline{y}$ are the mean values of x and y, σ_x and σ_y are the standard deviations, and *n* is the number of points. Strong positive correlations produce values near 1, and strong negative correlations have *r* = -1. A large sample of 26 non-transitional disks with CO emission were included to determine if the transitional disks were significantly different in their CO properties. All disks from our Keck survey with CO emission and observed at both wavelength settings were included.

A large scatter can be seen in all of the plots, likely indicating that reality is more complicated than the simple model presented in Section 4.5. Correlations were found with mass, luminosity, spectral type, age, and inner dust radius as presented in Figures 4.12 to 4.16. No correlations were found with inclination, A_V, or Pf β equivalent width. There might be some correlations with mass accretion rate, but the sample size with accurately determined mass accretion rates is small.

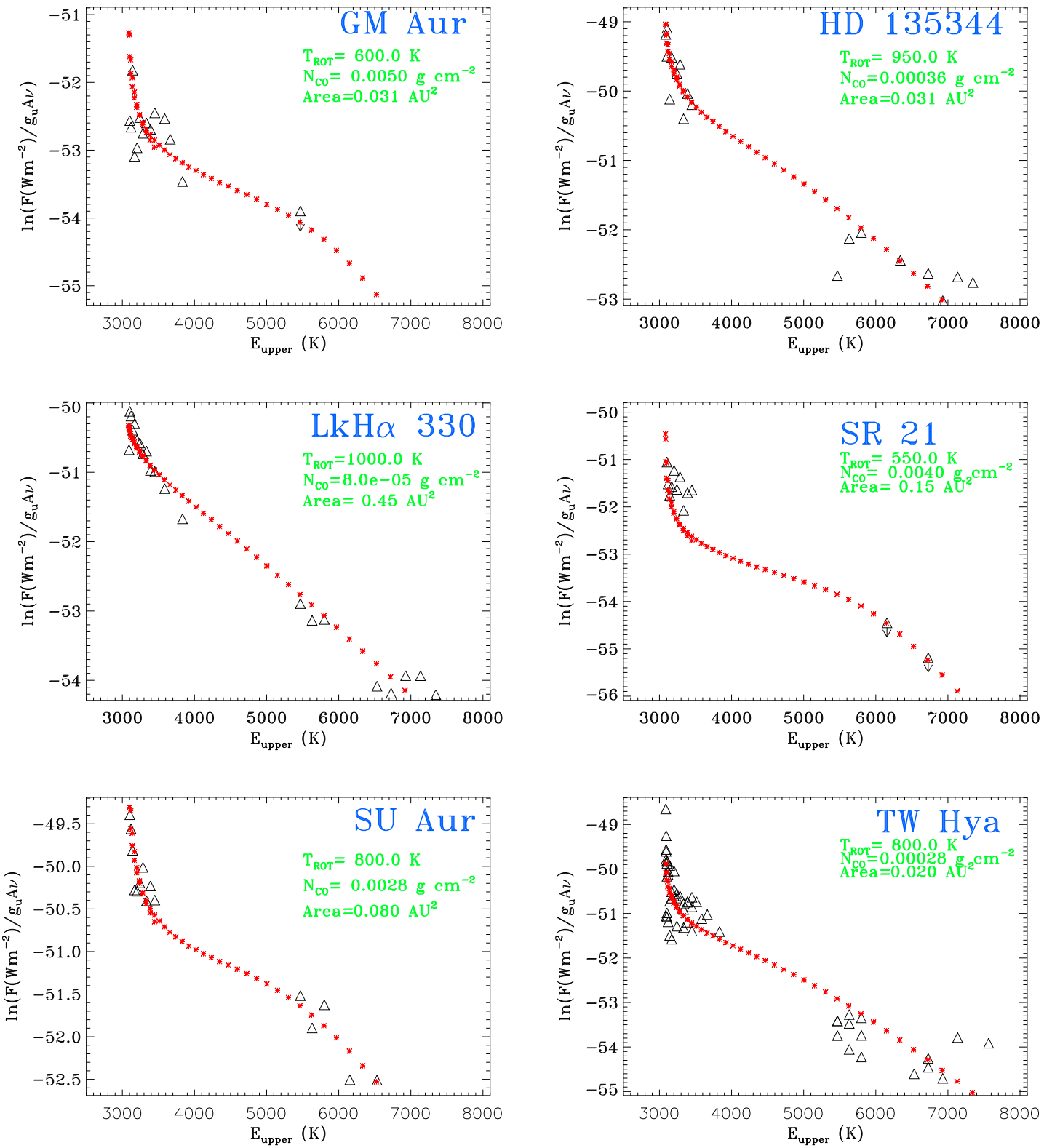

Figure 4.6 Rotation diagrams of the transitional disks. The black triangles are the data and the red stars are the model fit.

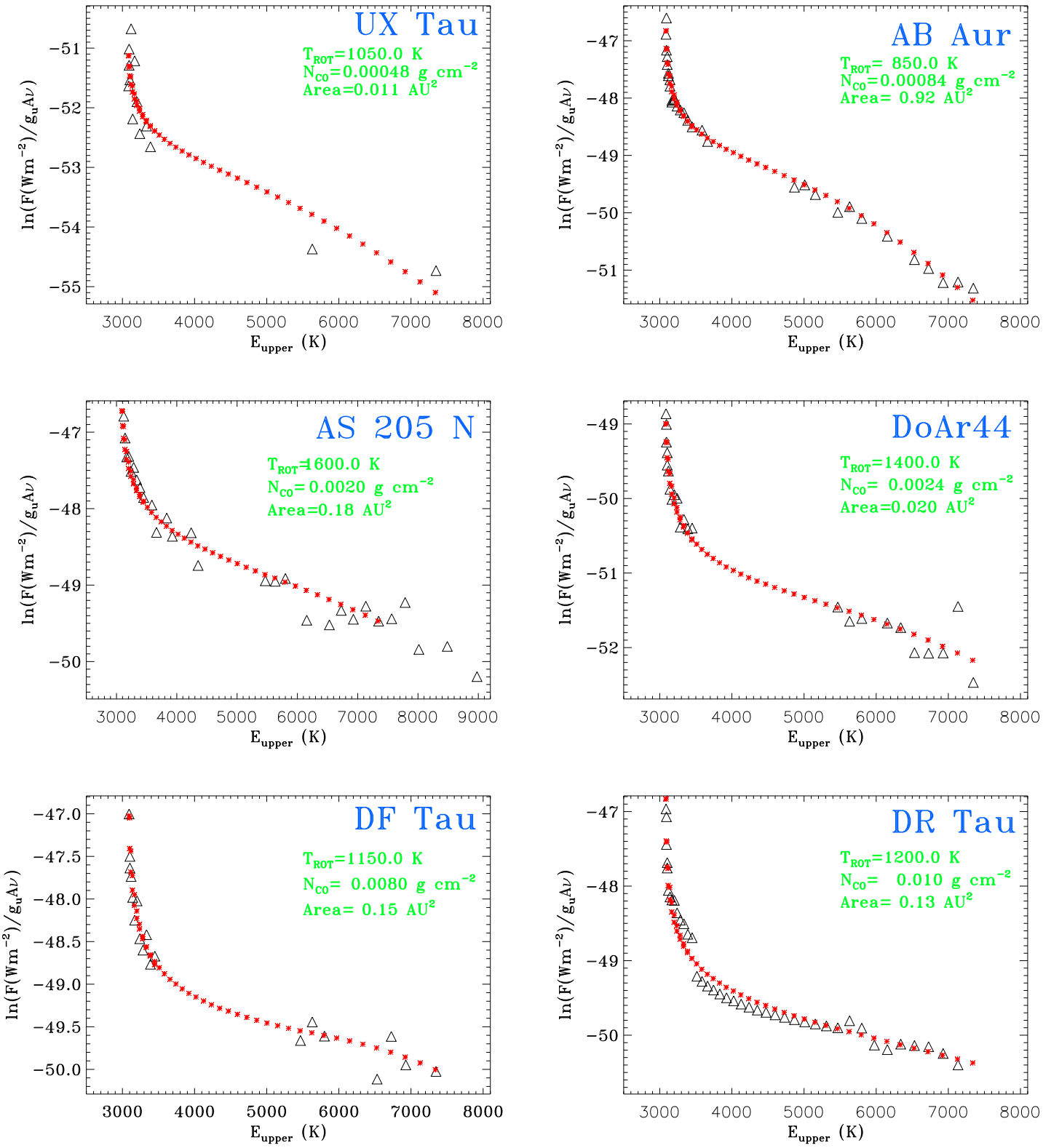

Figure 4.7 Rotation diagrams of non-transitional disks beginning with AB Aur.

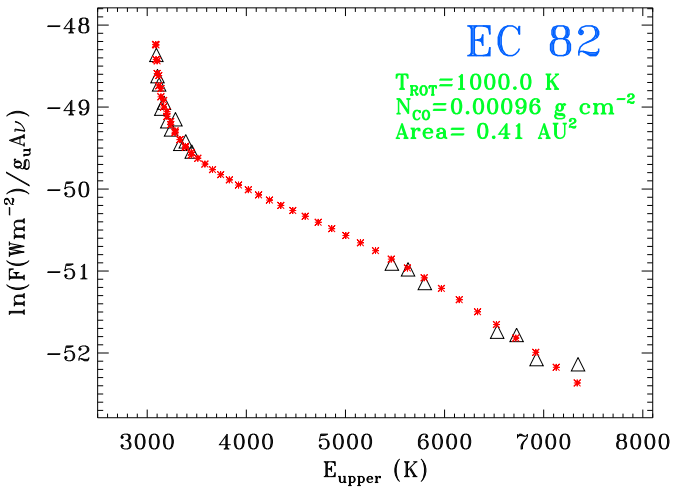

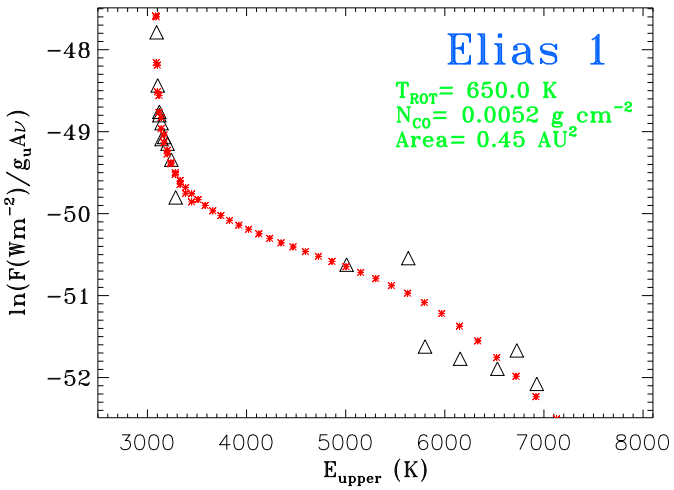

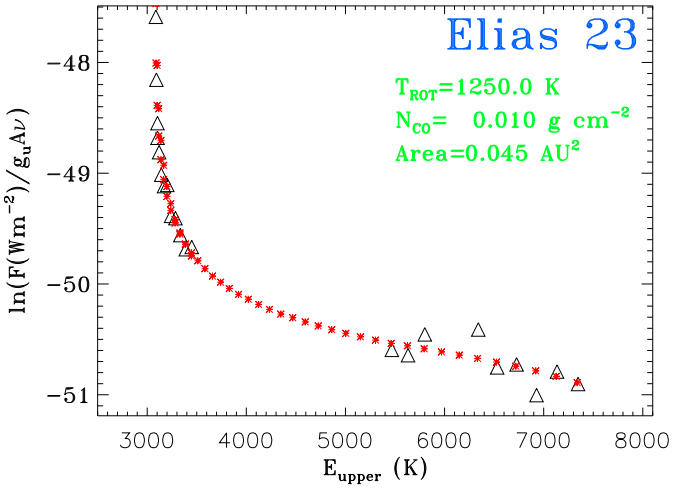

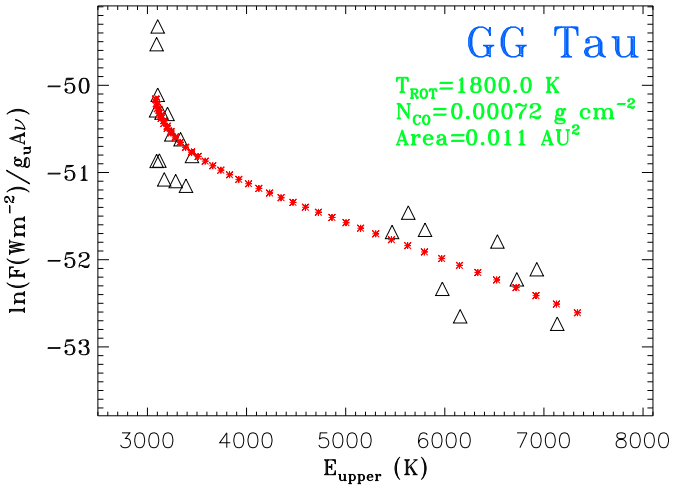

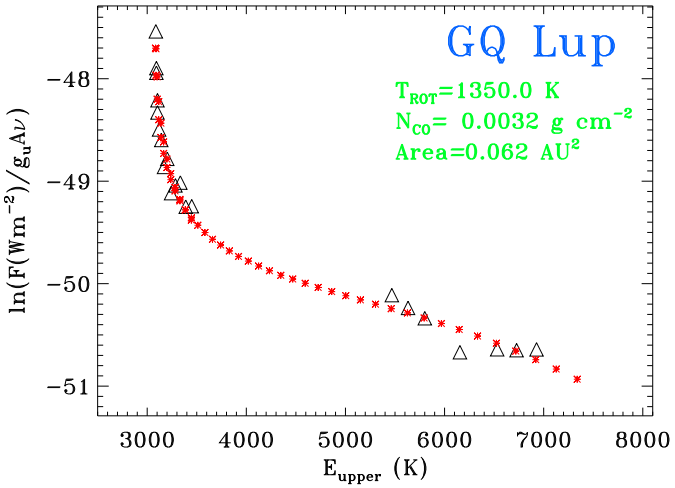

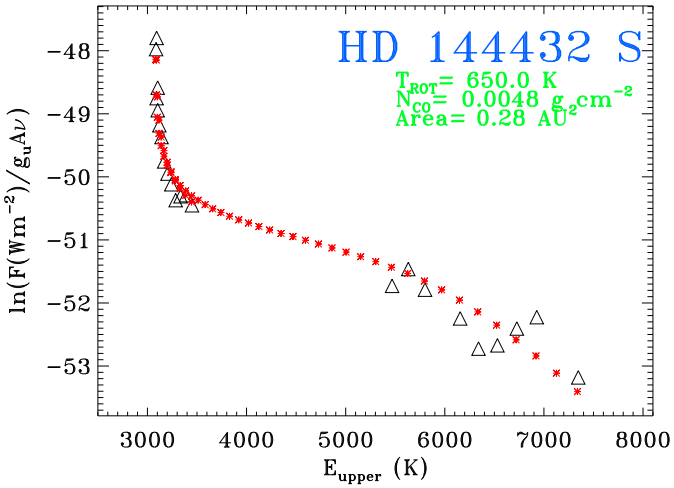

Figure 4.8 Continuation of Figure 4.7

.

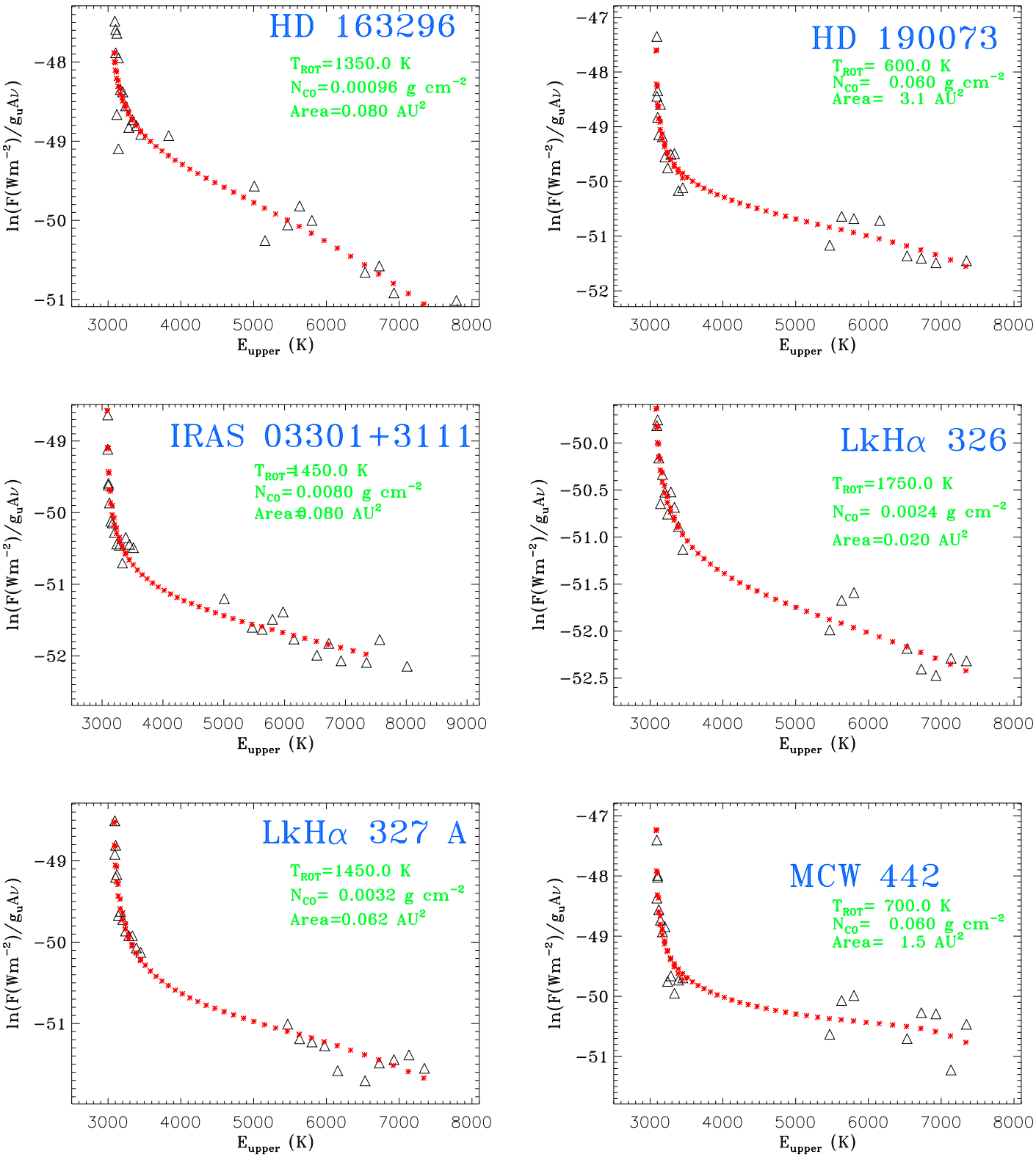

Figure 4.9 Continuation of Figure 4.7

.

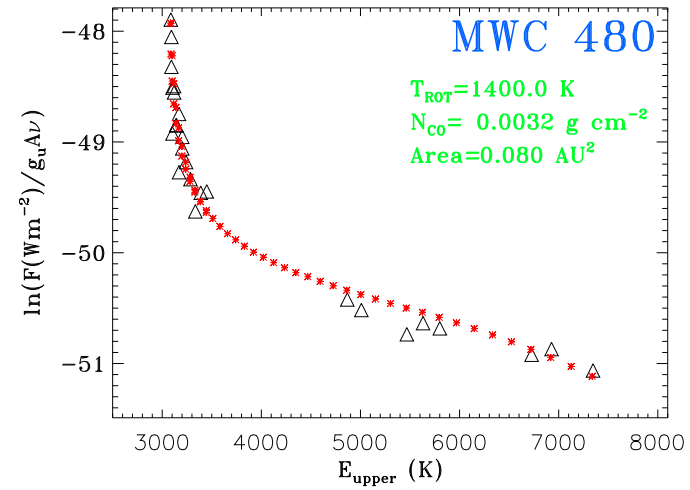

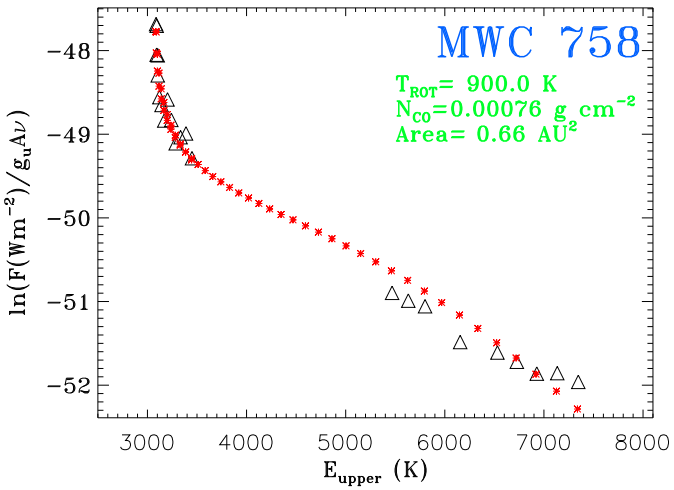

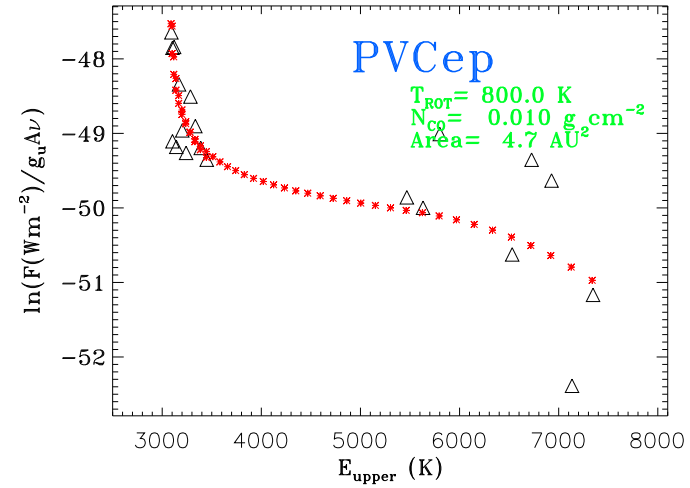

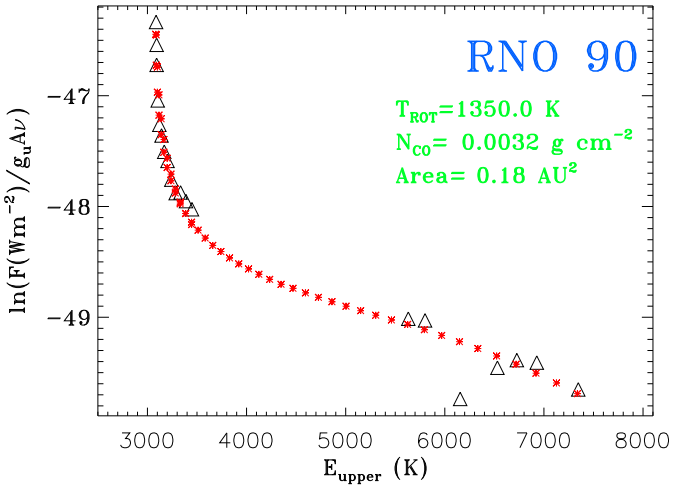

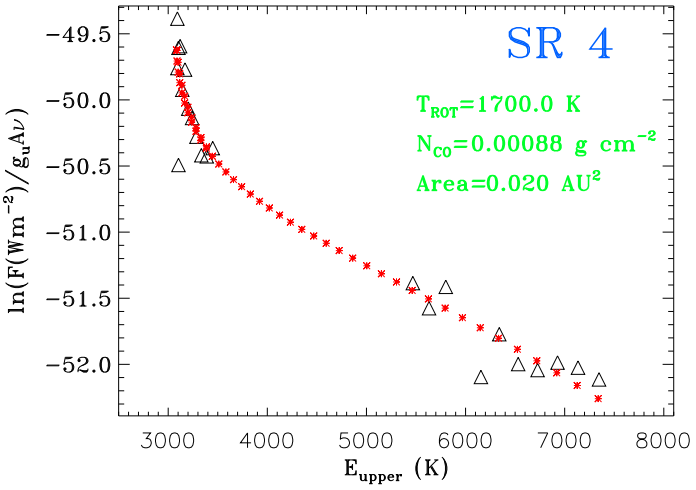

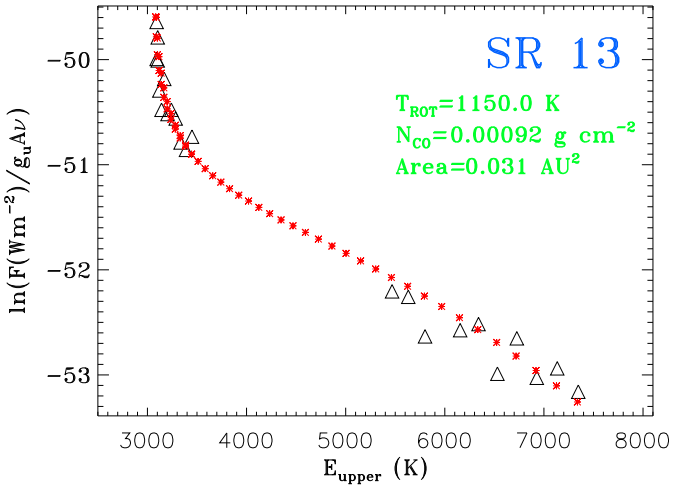

Figure 4.10 Continuation of Figure 4.7

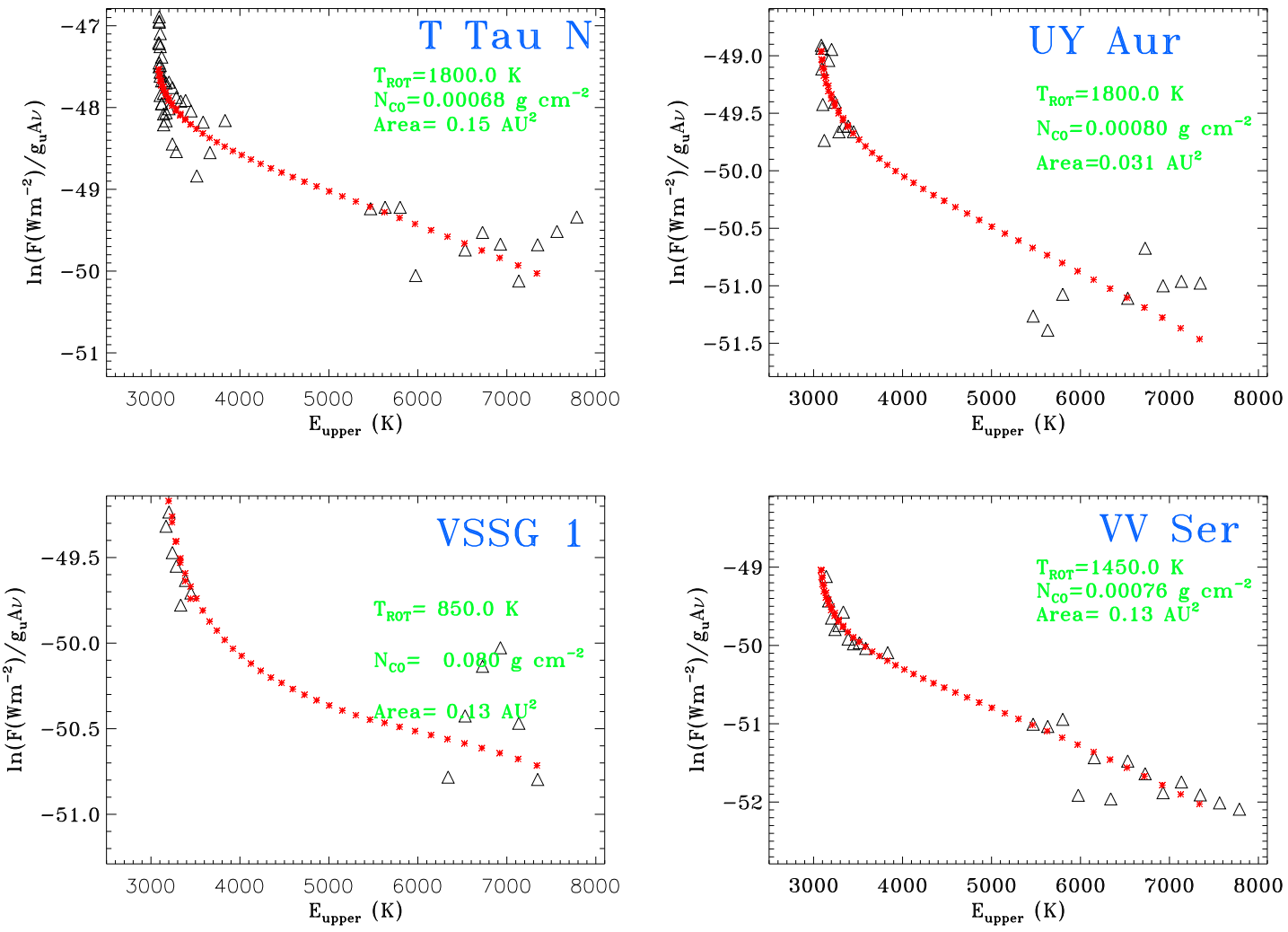

Figure 4.11 Continuation of Figure 4.7

.

For all disks, increased stellar luminosity leads to larger emitting area (bottom right, Figure 4.12). A similar effect is seen with increased stellar mass (bottom left, Figure 4.12). These correlations are in agreement with similar findings from optical/near-IR interferometric measurements (Eisner et al., 2007). More luminous and massive stars emit more energy, shifting the dust sublimation radius outward and in turn increasing the CO emitting area, which strongly tracks the dust sublimation radius (Figure 4.15). It is important to remember here that the emitting area is derived from the solid angle, and many different geometric orientations could underlie this parameter such as a uniform disk or a narrow ring. For the non-transitional sources, a strong trend is seen between rotation temperature and emitting area, both model derived parameters. Larger areas have lower temperatures as might be expected from material further away from the star. Inclination will also affect the observed solid angle, although the lack of a strong correlation between emitting area and inclination means this is unlikely to be the dominant effect. Correlations with age show that the densest CO is associated with the youngest stars and no old ($>$5 Myr) disks had column densities greater than 0.002 g cm^{-2} (see Figure 4.14). The spread of ages is limited with the oldest disks in the sample comprising only the transitional disks. However, the trend of decreasing CO column density with age seen here points to the expected dissipation of the gas over the same $\sim$10 Myr timescale seen for dust dissipation.

The transitional disks, marked by red crosses in Figures 4.12–4.16, are in many diagrams indistinguishable from their non-transitional counterparts. However, the cold disks do on average have lower CO temperatures than non-transitional sources with similar stellar properties (e.g., Figure 4.13). Disks around massive A spectral type stars have similar temperatures to the cold disks, but the emitting area is larger and likely corresponds to a cooler region of the disk. However, the transitional disks have low temperatures for the derived emitting area (see Figure 4.16).

4.7 Discussion

The inner regions of cold disks are depleted in dust as evidenced by their SEDs. However, the fate of the gas appears mixed. Fully seven of the ten transitional disks sampled here with NIRSPEC do show CO emission, which is often strong. The remaining three do not show CO lines within the S/N achieved. The presence of gas rules out photoevaporation as a cause of the dust gap, as photoevaporation models predict the total absence of gas in the inner disk region for such large holes (Alexander & Armitage, 2007). However, photoevaporation remains a possibility for the

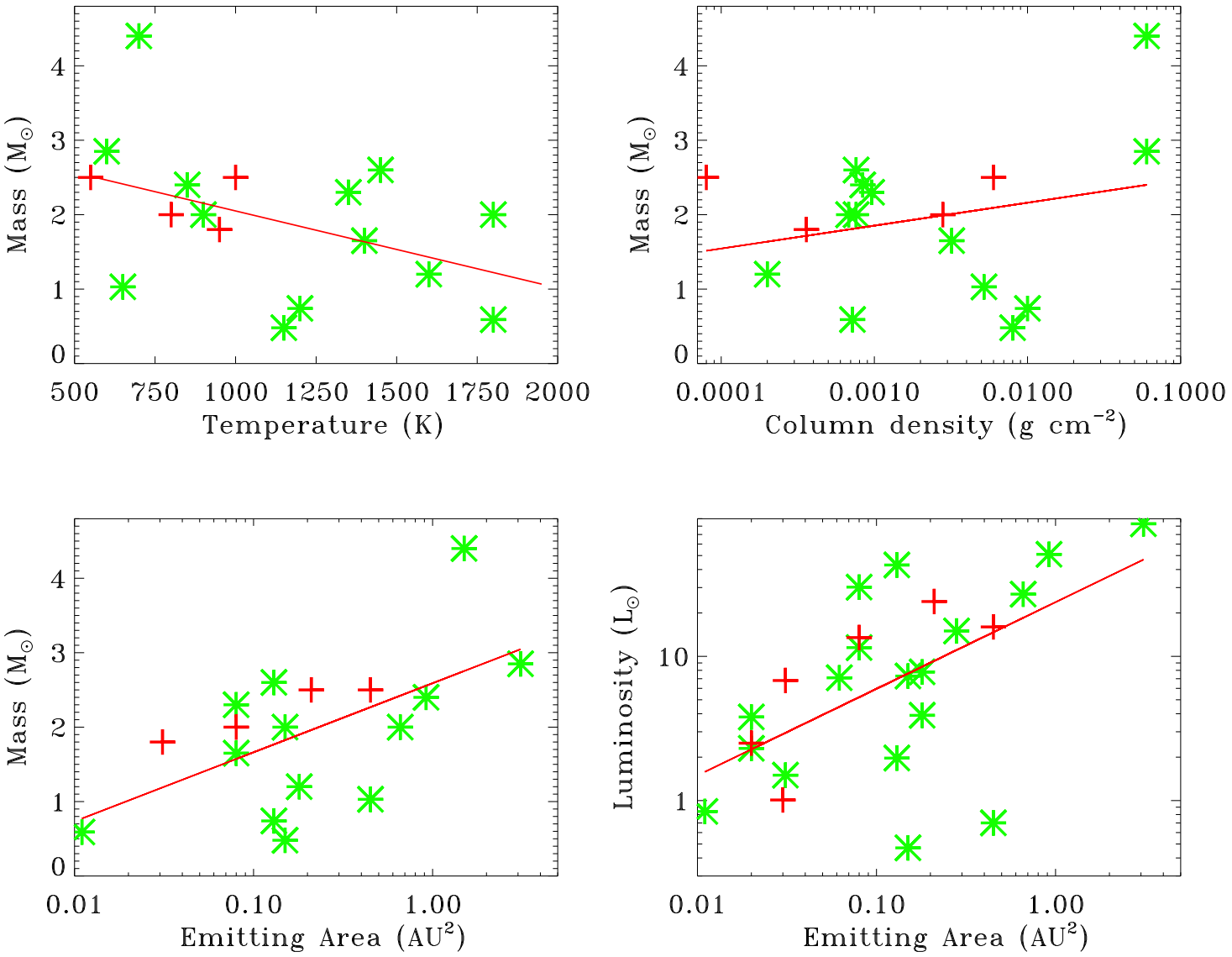

Figure 4.12 Correlations of rotation temperature (top left), CO column density (top right) and emitting area (bottom left) with stellar mass and emitting area with stellar luminosity (bottom right). The green stars are the non-transitional disks while the red crosses are the transitional disks. The best fit line is drawn in red. Correlation coefficients are listed in Table 4.4.

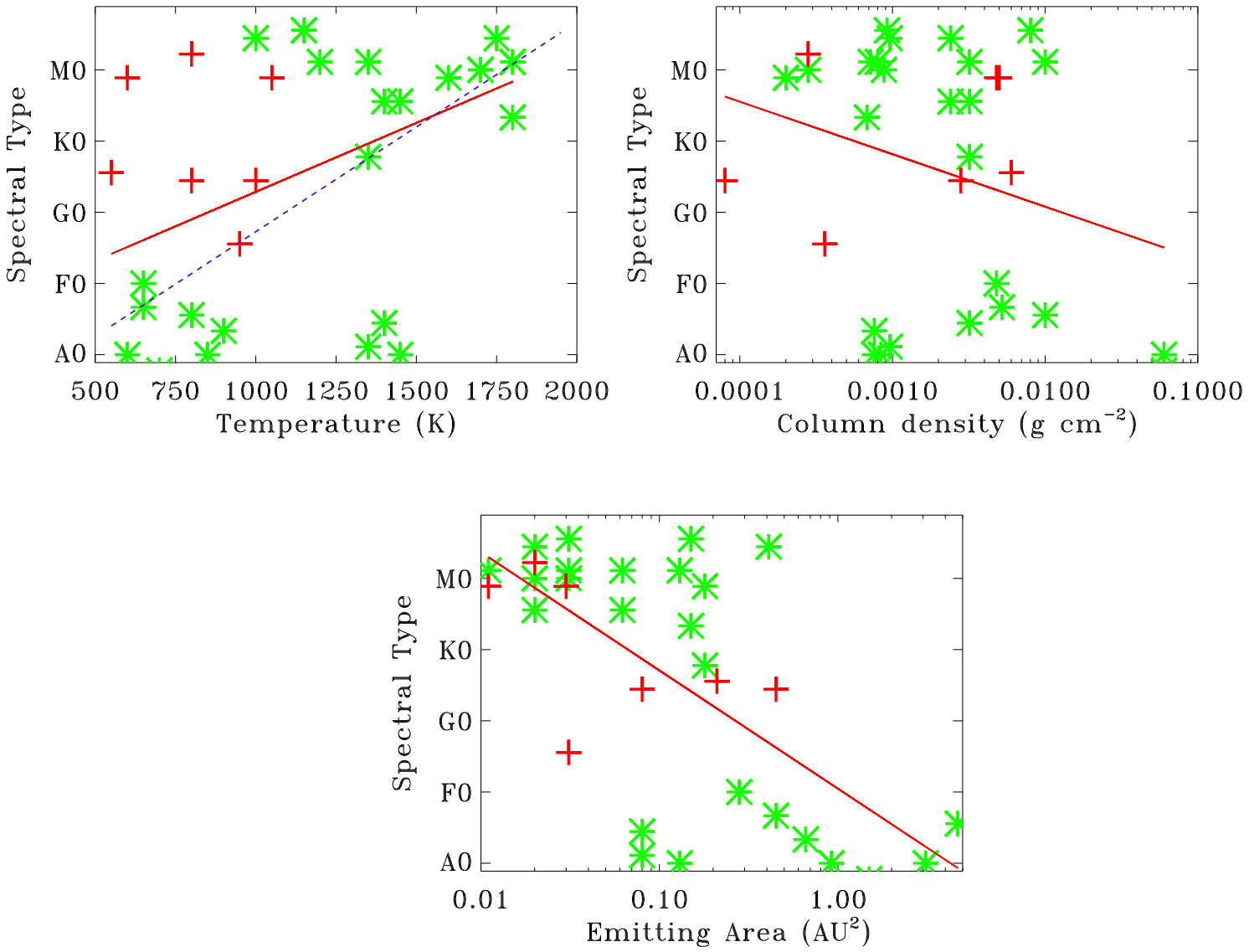

Figure 4.13 Correlations of CO temperature (top left), column density (top right) and emitting area (bottom) with spectral type. The green stars are the non-transitional disks while the red crosses are the transitional disks. The best fit line including all sources is drawn in solid red. In the top left plot, the best fit line excluding the transitional sources is drawn in dashed blue.

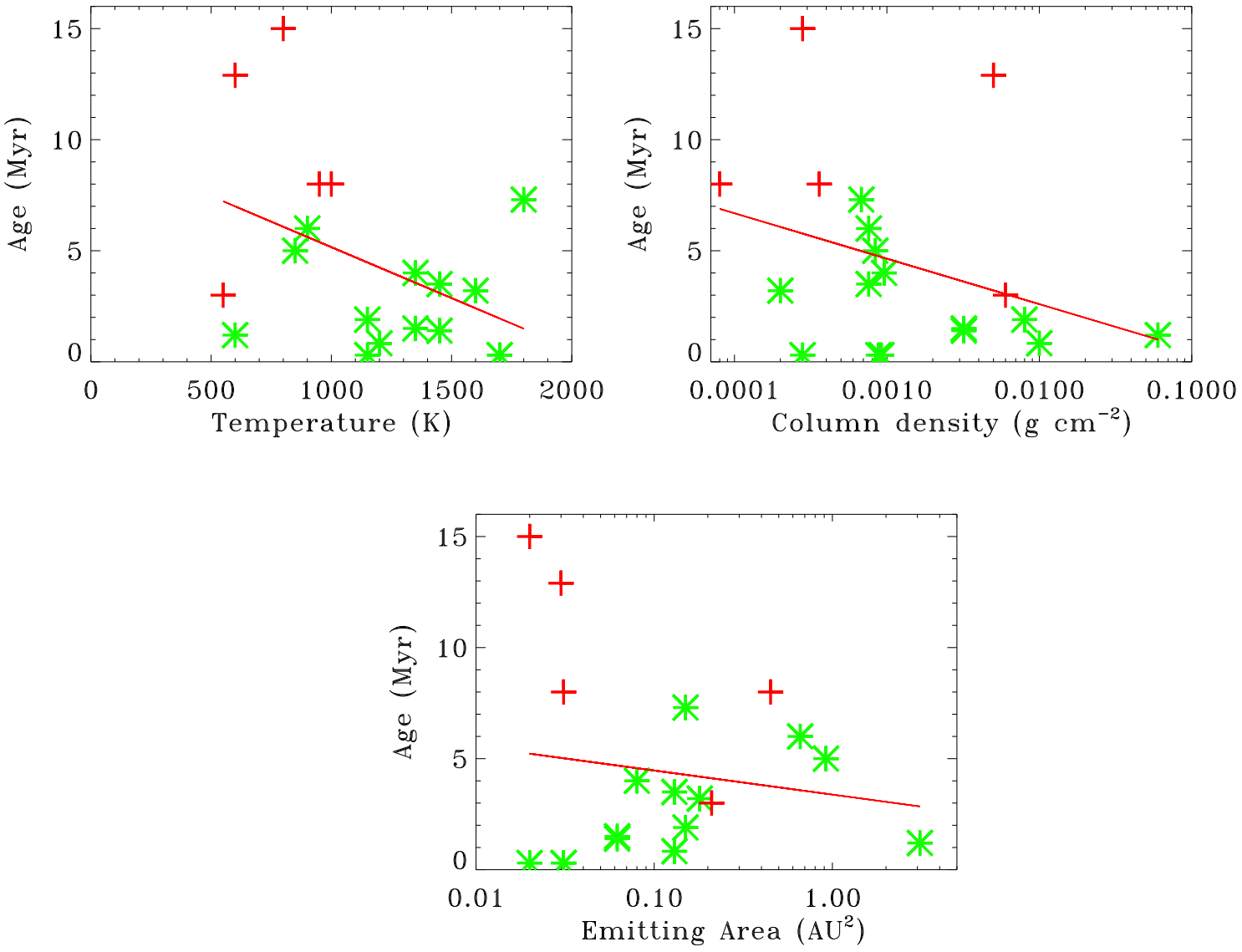

Figure 4.14 Correlations of CO temperature (top left), column density (top right) and emitting area (bottom) with age. The green stars are the non-transitional disks while the red crosses are the transitional disks. The best fit line is drawn in red.

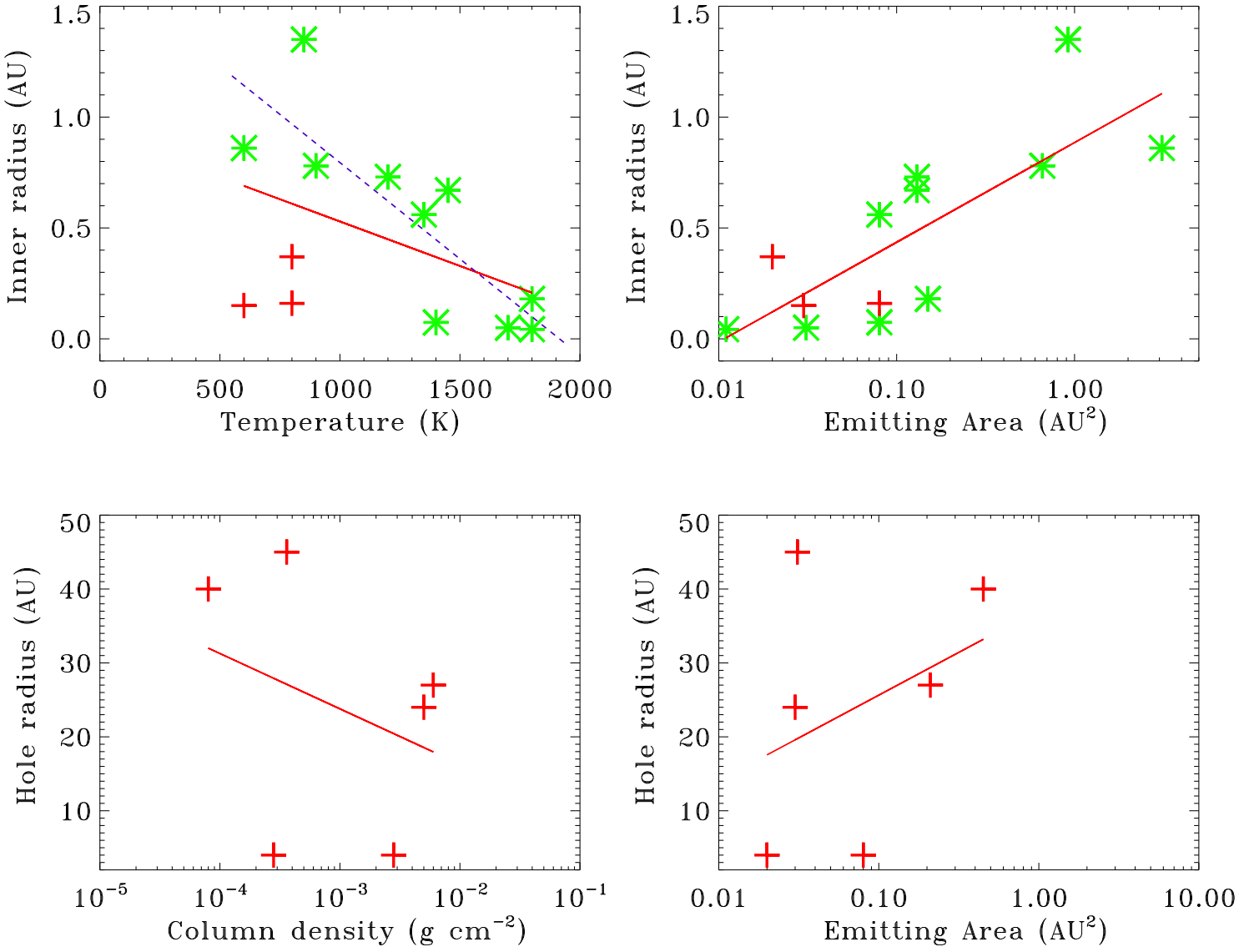

Figure 4.15 Correlations of CO properties with (top) optical interferometric measurements of the dust sublimation radius and (bottom) dust hole size in the transitional disks. The best fit line including all sources is drawn in solid red. In the top left plot, the best fit line excluding the transitional sources is drawn in dashed blue.

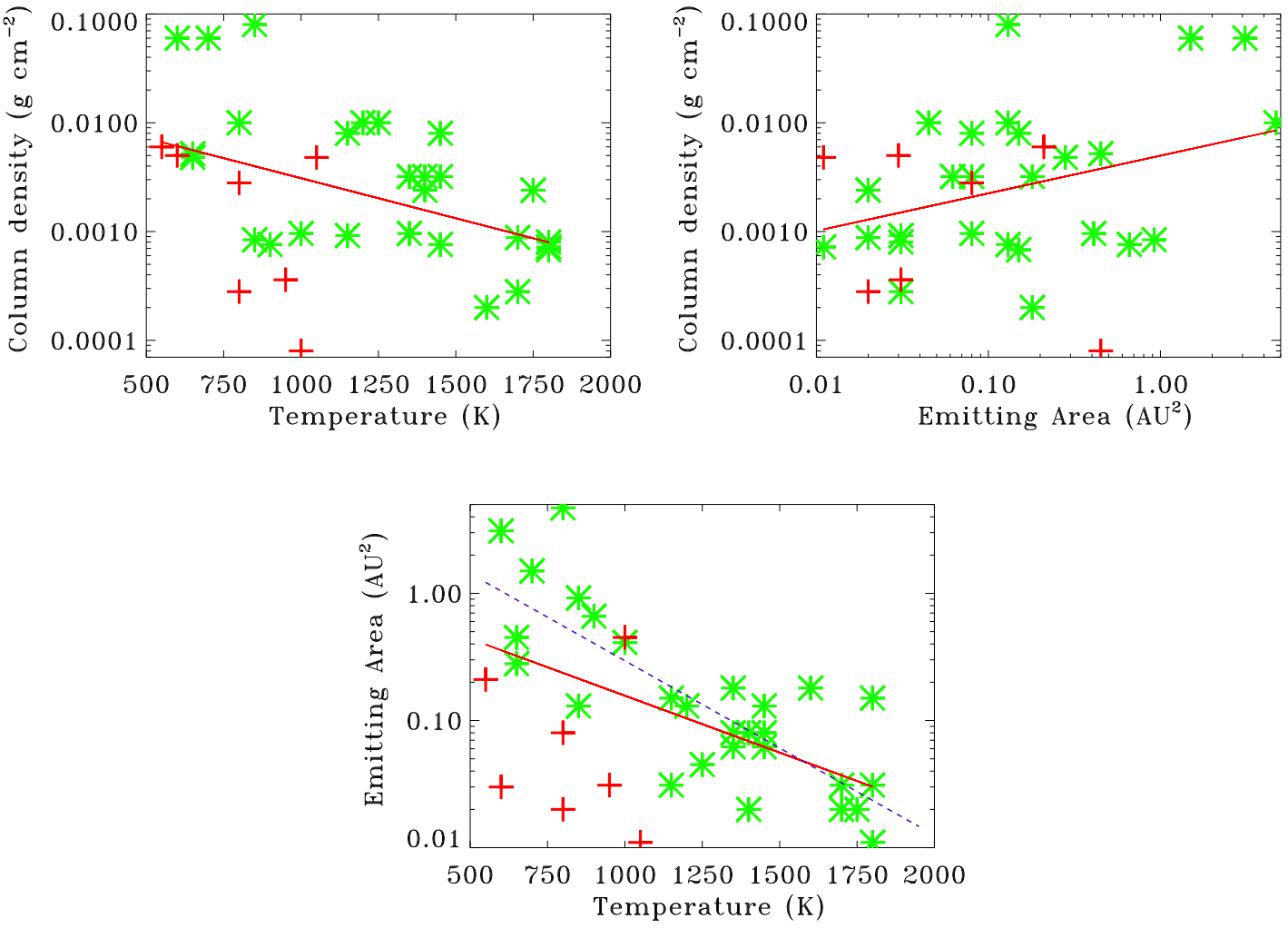

Figure 4.16 Correlations of derived CO properties with each other - CO column density with rotation temperature (top left), column density with emitting area (top right) and emitting area with temperature (bottom). The best fit line including all sources is drawn in red. In the bottom plot, the best fit line excluding the transitional sources is the blue dashed line.

Table 4.4. Linear Pearson correlation coefficients

Stellar parameter	Temperature	Column density	Emitting area
Stellar mass	-0.43	0.25	0.58
Stellar luminosity	-0.17	0.04	0.58
Spectral type	0.44/0.62	-0.32	-0.66
Inclination	0.26	0.03	-0.14
Accretion rate	0.06	0.44	0.31
Pf β EW	0.21	0.21	-0.05
Dust inner radius	-0.42/-0.83	0.32	0.77
Dust hole radius	0.34	-0.37	0.34
A_v	-0.13	-0.31	0.15
Age	-0.44	-0.52	-0.18
Rotation temperature	–	-0.34	-0.51/-0.79
CO column density	–	–	0.37

three disks without gas (and for T Cha, studied with CRIRES).

The three NIRSPEC non-detections, CoKu Tau 4, DM Tau and Hen 3-600, have different inner disks than the others. CoKu Tau 4 and Hen 3-600 are not accreting strongly. The lack of gas may well indicate that these inner disks have photoevaporated. Surprisingly, DM Tau does not show CO emission but is still accreting at 2×10^{-9} $M_\odot$/yr (White & Ghez, 2001) and has a massive outer disk imaged at millimeter wavelengths (Andrews & Williams, 2007b). The source is intrinsically faint but the spectrum places a 3-sigma line-to-continuum ratio limit of 1.4, assuming a line width of 15 km s^{-1}. These non-detections can place limits on the amount of gas present if some simple assumptions are made. We assume that the gas temperature would be 800 K, which is sufficient to excite CO v=1→0 emission and is fairly typical of the cold disks in general. We also assume an emitting area of 0.01 AU^2. This limits the CO column density to under 6×10^{-4} g cm^{-2}.

While the transitional disks contain regions that appear cleared of dust, the CO v=1→0 emission lines are surprisingly unaffected using classical disks as the reference. The detection rate of CO gas for the these sources, including the CRIRES nondetection of T Cha, was 64%. Only weak trends are seen with gap size, indicating that the innermost gas is largely unaffected by the amount of dust clearing further out in the disk. As most of the transitional stars are still accreting, their inner gas has a limited lifetime, which for most of these sources is of order only a few thousand years. The presence of CO v=1→0 emission lines from 64% of the transitional disk sample suggests that the inner gas reservoirs are being replenished despite dust clearing.

Carbon monoxide emission lines are only sensitive to gas at certain physical conditions and

there may be substantial reservoirs of unobservable CO gas present. If the gas is too cold and does not receive UV radiation or resonantly scattered 4.7 μm photons, then it will not be excited to higher energy states and will not emit. Also, only gas emission above the τ = 1 surface escapes without begin absorbed again by the dust. Although transitional disks are thin in the vertical direction compared to classical disks, significant column densities and hence high optical depths often exist radially. Since the heating comes from the central star, this can create significant vertical temperature structure. The observations here only measure the upper layer and thus place lower limits on the total disk column density. It also means that lowering the dust density and thus the τ = 1 surface can artificially enhance the apparent CO line strength and column density. While this might affect the transitional disks, it does not explain the lower rotational temperatures, as the fractional increase in flux would be larger for the weaker high energy lines, leading to higher temperature measurements.

Transitional disks show cooler rotation temperatures compared to stars of similar spectral type. The cooler temperatures might be taken to suggest that the gas is at larger radii. However, the small emitting area and the line profiles make it unlikely to be a shift in the location of the gas. One explanation is that CO observations in transitional disks probe further below the surface layer of the disk. The lower dust density results in the τ = 1 dust surface lying at smaller scale heights, so gas observations probe cooler gas that is closer to the midplane. Another explanation may be that reduced photoelectric heating due to the lower dust content results in a very different disk temperature profile.

4.8 Conclusions

CO emission is detected from 70% of the transitional disks observed with NIRSPEC at the Keck II telescope, indicating that there is still gas in the inner regions. Rotational excitation temperatures, column densities and emitting radii were determined using rotation diagrams and a simple thermal model. Significant differences are apparent between the transitional disks and the larger disk sample. Transitional disks show cooler rotation temperatures compared to stars of similar spectral type. Within the model, the derived rotation temperatures and emitting radii also show a distinct segregation between the transitional and non-transitional disks.

Chapter 5

CSO submillimeter observations

Abstract

While scarce, disks that represent the transitional phase between T Tauri-like disks and debris disks are vital to our understanding of planet formation and disk evolution. The Spitzer Legacy Program "Cores to Disks" has identified dozens of transitional disk candidates. We have observed 19 new sources identified in the c2d Spitzer maps and 22 previously known sources with the CSO SHARCII camera at 350 μm and 450 μm to characterize their outer disks. Combined with resolved images at longer wavelengths and infrared spectroscopy of the warm inner regions, the SHARCII flux ratio and fluxes detail the evolutionary state of the disk, providing information vital to the determination of grain size, disk extent, and temperature/density distribution as a function of radius. Knowledge of these properties is required to make meaningful conclusions regarding disk evolutionary schemes and planet formation mechanisms.

5.1 Introduction

Transitional disks are usually discovered through their relative lack of mid-infrared emission, as the dust emission in that spectral region arises from grains no more than tens of AU away from the central star, matching well the putative gap radii. However, the apparent evolution of the interior dust leaves open intriguing questions about the state of the dust in the outer disk. It is clear from long wavelength Spitzer observations and large millimeter surveys, such as Beckwith et al. (1990), Andre & Montmerle (1994), and Andrews & Williams (2005, 2007a), that transitional disks often have substantial outer disks, but a more detailed analysis of their properties is needed. Has there been notable evolution in dust grain sizes, indicating grain growth? Are these disks more or less massive than average? In order to answer such questions, it is necessary to turn to (sub)millimeter wavelengths to study the outer disk.

Submillimeter emission arises primarily from the optically thin outer disks, with sizes ranging up to several hundred AU. Submillimeter observations thus probe the vast majority of the dust population leading to a good estimate of dust disk masses. The detailed shape of the submillimeter SED, obtained through multi-wavelength observations, also reflects the dust opacity and temperature structure (Beckwith & Sargent 1991, Mannings & Emerson 1994). As grains grow, the Rayleigh-Jeans slope flattens providing a signature of evolution in the outer disk. The opacity is strongly influenced by the exact dust properties including size and composition.

Transitional disks are rare so current studies usually focus on individual disks rather than a statistically significant sample. The large scale mapping of the Spitzer Legacy Program "Cores to Disks" (Evans et al., 2003) has provided a complete photometric inventory of young stars within five nearby star forming clouds in areas with $A_v > 3$. Flux from these disks falls with increasing wavelength, allowing submillimeter flux measurements to more efficiently determine long wavelength flux levels than millimeter observations and to define a viable sample for follow-up high resolution millimeter interferometry.

Measurements at 350 and 450 μm provide a measure of the SED slope and, combined with supplemental data, constrain disk parameters such as dust grain size, physical disk extent and emission profile, which are fundamental for understanding both disk evolution and planet formation. Model SED-based fits also benefit from this constraint on the allowed parameter space.

Table 5.1. CSO SHARCII detections

Source	R.A.	Declination	Flux$_{350\mu m}$ (mJy)	3σ RMS (mJy)	Flux$_{450\mu m}$ (mJy)	3σ RMS (mJy)
HD 135344B	15:15:48.88	-37:09:16.0	5289	85.6	4096	68.0
SR 4	16:25:56.30	-24:20:50.0	470	14.0	353	9.1
VSSG 1	16:26:18.86	-24:28:19.7	621	15.	610.	11.
DoAr 24E	16:26:23.38	-24:21:00.1	1390	77.	–	–
SR 21	16:27:10.20	-24:19:16.0	2527	37.	1967.	28.
IRS 51	16:27:39.82	-24:43:15.1	657	19.	539	14.
SR 9	16:27:40.27	-24:22:04.0	141	6.6	74.5	6.1
SR 13	16:28:45.28	-24:28:19.0	615	14.	303	7.5
DoAr 44	16:31:33.54	-24:27:37.0	697	53.5	661	12.
GY 224	16 27 11.18	-24 40 46.7	564	19.	376	10.
IRS 46	16:27:29.70	-24:39:16.0	592	60.	658	34.
SSTc2d J182900.9+002931	18:29:00.88	00:29:31.5	91.3	33.0	–	–
SSTc2d J182953.1+003607[1]	18:29:53.06	00:36:06.5	701	42.	–	–
EC 90[1]	18:29:57.68	01:14:07.1	6820.	293.	–	–
LkHα 330	03:45:48.28	32:24:11.8	1600	320.	1000.	20.5
Serpens SMM3[2]	18:29:59.3	01:14:02.3	12300	293	–	–
Serpens SMM4[2]	18:29:57.1	01:13:15	21500	384	–	–

[1]This is a confused region and the aperture was placed at the nominal source position.

[2]Serendipidous source in map

5.2 Observations

SHARCII on the Caltech Submillimeter Observatory (CSO) 10.4 m Leighton telescope was used to obtain 350 and 450 μm fluxes for $\sim$20 potential cold disks identified in the *c2d* program and the literature. The majority of the data were collected in 2005 April during a period of excellent submillimeter weather ($\tau_{225GHZ} \leq 0.05$). Further data were obtained in 2005 July and 2007 May. SHARCII is a 384 bolometer array with a FWHM beam diameter of 8-9". Uniform coverage was obtained by scanning the telescope in a Lissajous pattern over the source. The data were reduced using the latest version [1.52] of CRUSH.

Fluxes were obtained from the coadded images using aperture photometry. Apertures of 6.4-16 arcseconds were tried, but the final photometry was calculated using a 9.6 arcsecond aperture. Planetary observations [Neptune (2005 April, 2007 May) and Mars (2005 July)] were used to bootstrap the calibrator fluxes and where possible were used to directly correct the science data. The scatter in the calibrator fluxes was 20%, so fluxes were corrected to the mean of all the calibrator scans for the run rather than with the most contemporaneous scan. In almost all cases, the errors in the fluxes

Table 5.2. CSO 350 μm non-detections

Source	R.A.	Declination	3σ RMS (mJy)	Mass limit ($M_\odot$)
HD 147196	16:21:19.19	-23:42:28.7	64.9	1.2e-4
SSTc2d J162131.9-230140	16:21:31.91	-23:01:40.3	127.6	2.4e-4
SSTc2d J162148.5-234027	16:21:48.48	-23:40:27.3	84.7	1.6e-4
SSTc2d J162221.0-230403	16:22:21.00	-23:04:02.6	88.9	1.7e-4
SSTc2d J162245.5-243124	16:22:45.48	-24:31:23.9	40.4	7.5e-5
SSTc2d J162332.9-225847	16:23:32.85	-22:58:46.9	88.4	1.6e-4
SSTc2d J162506.9-235050	16:25:06.91	-23:50:50.4	42.5	7.9e-5
SR 1	16:25:24.32	-24:27:56.6	130.5	2.4e-4
IRS 9	16:25:49.00	-24:31:36.0	162.0	3.0e-4
GSS 20	16:25:57.50	-24:30:34.0	131.9	2.5e-4
VSS 27	16:26:46.50	-24:12:03.0	135.1	2.5e-4
IRS 42	16:27:21.46	-24:41:43.1	283.9	5.3e-4
Haro 1-14	16:31:05.20	-24:04:04.4	106.3	1.9e-4
SSTc2d J163854.8-241120	16:38:54.80	-24:11:20.0	113.8	2.1e-4
SSTc2d J182816.3-000316	18:28:16.29	-00:03:16.4	232.4	1.4e-3
SSTc2d J182821.6+000016	18:28:21.58	00:00:16.2	68.9	4.4e-4
SSTc2d J182849.4-000605	18:28:49.39	-00:06:04.6	73.2	4.7e-4
SSTc2d J182902.9+003009	18:29:02.86	00:30:09.0	339.5	2.2e-3
SSTc2d J182915.1+005212	18:29:15.09	00:52:12.3	79.1	5.1e-4
SSTc2d J182915.6+003912	18:29:15.58	00:39:11.6	50.4	3.2e-4
SSTc2d J182935.6+003504	18:29:35.62	00:35:03.6	226	1.5e-3
SSTc2d J182936.2+004217	18:29:36.19	00:42:16.5	96.2	6.2e-4
SSTc2d J182947.3+003223	18:29:47.27	00:32:23.0	213	1.4e-3
EC 82	18:29:56.89	01:14:46.5	672.1	4.3e-3
EC 92	18:29:57.88	01:12:51.6	383.6	2.5e-3
SSTc2d183019	18:30:18.9	01:14:16.7	145.1	9.3e-4

are dominated by flux calibration uncertainties rather than noise in the images. The fluxes of the 15 sources detected by SHARCII can be seen in Table 5.1.

The sample was selected via two different methods. Since one of the primary goals of this project was to identify suitable targets for follow-up interferometric study, breadth was favored over depth, so many targets were examined, resulting in upper limits of $\sim$100 mJy (see Table 5.2). The c2d sources were selected based on simple fits of a stellar photosphere to 2MASS fluxes along with IRAC + MIPS photometry to characterize the disk. Sources that are photospheric through IRAC 3 (5.8 μm) but had excesses in IRAC 4 (8.0 μm) and MIPS 1 (24.0 μm) were considered potential cold disks and included in the sample. Sources from the literature included known cold disks primarily found through mid-IR SEDS and transitional disks found through submillimeter photometry. The submillimeter-identified transitional disks, primarily from Andre & Montmerle (1994), had shallow

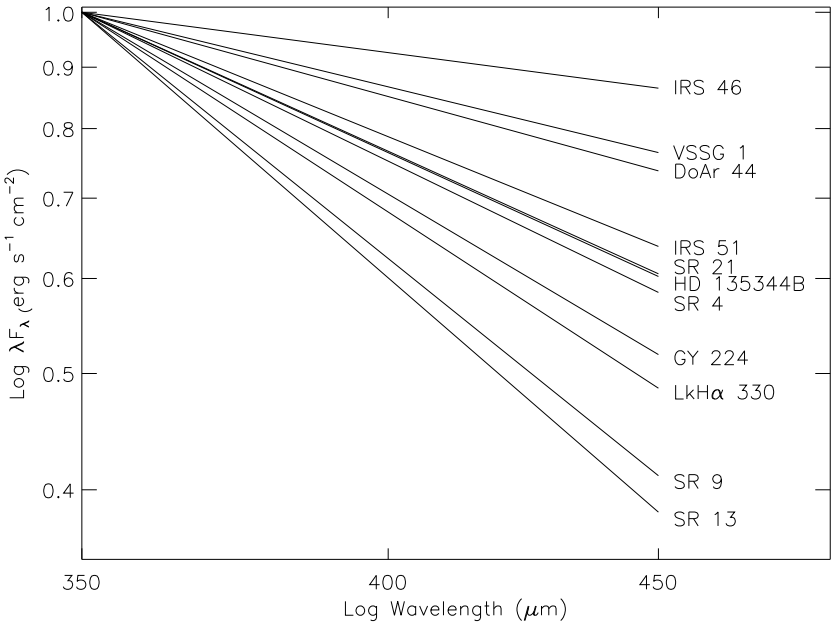

Figure 5.1 Wavelength vs. flux at 350 and 450 μm normalized at 350 μm.

submillimeter slopes that were taken as an indication of grain growth. The sample is also heavily biased towards Ophiuuchus and Serpens due both to more observing time and better weather in the spring observing runs.

5.3 Analysis

5.3.1 Submillimeter colors

The (sub)millimeter slope is usually well fit by a power-law such that $F_\nu \; \alpha \; \nu^\alpha$. The parameter α is often used to determine the evolution of large dust grains, as it directly relates to the opacity in optically thin disks where $\alpha = 2 + \beta$. Here, β characterizes the frequency dependence of the mass opacity coefficient of the dust opacity, κ, where $\kappa = \kappa_0(\frac{\nu}{\nu_0})^\beta$. For small amorphous grains ($a_{max} < 10$ μm), β is a constant with value $\sim$1.75 (D'Alessio et al., 2001). β reaches a maximum where $2\pi a/\lambda \approx 1$,, so for 350 μm, maximum β is reached when most particles have radii near 55 μm. The value of β then decreases with increasing size until $a_{max} > 10$ cm, at which point β becomes independent of size as the particles become unobservable. The interstellar medium, which mainly contains low density, unprocessed grains of submicron size, has $\alpha \approx 3.8 \pm 0.2$ (Draine,

Table 5.3. Isothermal model best fit values

Source	Distance (pc)	$Mass_{disk}$ ($M_\odot$)	Temperature (K)	β	α
DM Tau*	140.	0.013	38.	0.1	1.74
GM Aur*	140.	0.036	38	0.4	1.98
HD 135344B	84	0.004	47	1.3	2.9
LkCa 15*	140	0.05	23	0.1	1.47
LkHα 330	250	0.042	26	1.6	2.8
SR 21	132	0.032	17	2.2	2.53
UX Tau*	140.	0.032	14.	1.1	1.97
DoAr 44	132	0.023	29	0.0	1.56
GY 224	132	0.006	32	0.3	1.86
IRS 46	132.	0.020	11.	2.1	0.43
IRS 51	132	0.017	26	0.0	1.45
SR 4	132	0.020	11	1.9	1.99
SR 9	132	0.001	47	-0.1	1.65
SR 13	132	0.007	44	0.0	1.70
VSSG 1	132	0.035	11	2.2	1.88

*All fluxes taken from Andrews & Williams (2005) and Andrews & Williams (2007a) in order to expand the transitional disk sample

2006). However, Beckwith & Sargent (1991) found that protoplanetary disks have shallower slopes with $2 < \alpha < 3$. In a more recent study, Andrews & Williams (2007a) found that the median α in their Ophiuchus sample was 2 with only a few percent having $\alpha \geq 3$. While it is generally agreed that submillimeter continuum emission roughly follows $F_\nu \; \alpha \; \nu^{2+\beta}$, the exact value of β remains a question of contention (Hildebrand 1983, Wright 1987, Pollack et al. 1994, Henning & Stognienko 1996).

The submillimeter colors between 350 μm and 1.3 mm were calculated by finding the best fit line in log ν - log F_ν space. Figure 5.1 shows the submillimeter slopes for all the disks in the sample with both 350 and 450 μm fluxes. To provide more constraints, 850 μm fluxes have been taken from Andrews & Williams (2005) and Andrews & Williams (2007a), who also collected 1.3 mm measurements from the literature, which have been added to the full data set. Values of α are presented in the last column of Table 5.3.

5.3.2 Isothermal model

While submillimeter data are straightforward to interpret under the assumption of an optically thin disk, this is often not the case in the more massive disks surrounding young classical T Tauri stars, particularly at shorter wavelengths. For sources with both 350 and 450 μm measurements, I have modeled the disk submillimeter emission with a simple thermal blackbody model. Spatially resolved measurements are necessary to determine the fraction of material which is optically thick, but shortward of 1 mm, the fraction is likely to be in the range of 20-30 % for typical disk masses and radii (Andrews & Williams, 2007a).

The disk flux is governed by the Planck function such that

$$F_\nu = \frac{\cos(\mathrm{i})}{4\pi d^2} \int_{r_0}^{r_d} \frac{2h\nu}{c^2} \frac{1}{e^{h\nu/kT}-1} (1-e^{-\tau \sec(\mathrm{i})})\ 2\pi r\ dr, \tag{5.1}$$

where i is the disk inclination, d is the distance, T is the temperature, τ is the optical depth, and r_0 and r_d are the inner and outer disk edges, respectively.

The disk structure is approximated by a radial power law such that $\Sigma \propto r^{-p}$. A single temperature is assumed for the disk both to limit the number of free parameters and to approximate a midplane layer within the disk. The choice of p is not well constrained and might vary between disks. For simplicity, a value of 1.5 is used here in agreement with Weidenschilling (1977). This structure is equivalent to an initial picture of our Solar System, where the mass in the planets is increased to cosmic abundances and smeared out in radially symmetric annuli. Using a value of $p = 1$ has little effect on the results of this model. For example, the parameters for SR 21 become T=17, β=1.9 and M=0.023 rather than T=17, β=2.0 and M=0.022. The optical depth, τ, is the product of the opacity, κ_ν, and the surface density, Σ_r. One of the major uncertainties is the opacity, κ_ν. Here, we follow Beckwith et al. (1990) and adopt $\kappa_0 = 0.02$ cm^{2}g^{-1} anchored at $\nu_0 = 230$ GHz, and leave β as a free parameter. These values implicitly assume a gas to dust ratio of 100.

The disks are taken to have inner radii of 0.1 AU, outer radii of 100 AU, and inclinations of zero degrees (that is, the disks are face on). This leaves three free parameters: the temperature of the layer, β, and the mass of the disk. The best fit model was found using a χ^2 test and the resulting three parameters of temperature, disk mass and β can be found in Table 5.3.

5.3.3 Disk masses

For disks with only upper limits from the SHARCII observations, I have calculated the corresponding upper limits to the disk masses assuming an optically thin disk and that the Rayleigh-Jeans approximation is valid (see Table 5.2). As these disks are fainter at submillimeter wavelengths, there is likely less material present in the outer disk, making this a more appropriate assumption. As $h\nu << kT$, equation 5.1 simplifies to

$$S_\nu = B_\nu = \frac{2h\nu^3/c^2}{exp(h\nu/kT)-1} = 2kT\frac{\nu^2}{c^2}. \tag{5.2}$$

In order to determine the flux density, one must integrate over the solid angle, Ω, the source function, S_ν, times the optical depth, τ where $\tau = \kappa\Sigma$, such that

$$F_\nu = \int S_\nu \tau d\Omega = \int 2kT\frac{\nu^2}{c^2}\kappa_\nu\Sigma_d\frac{\sigma}{D^2}. \tag{5.3}$$

The total disk mass, M_D, can be found by integrating the surface density of the disk, Σ, over the surface area, σ, such that $M_D = \int \Sigma d\sigma$. Thus,

$$F_\nu = \frac{2k < T >}{D^2}\frac{\nu^2}{c^2}\kappa_\nu M_D. \tag{5.4}$$

It is assumed that the emission arises primarily from an approximately isothermal region with temperature, T. As the disk temperatures from the isothermal model span a range between 10 and 50 K with an average of 29$\pm$13 K, I have assumed that T is 30 K to derive upper limits.

5.4 Results

I have detected 15 disks at 350 μm and 11 of these at both 350 and 450 μm. Of these, 8 are transitional disks from the submillimeter literature and 3 are cold disks with central holes identified in the infrared. To expand the transitional disk sample, 4 additional cold disks have been modeled using the fluxes from Andrews & Williams (2005) and Andrews & Williams (2007a). An additional 26 disks were observed for which only upper limits were established on the disk masses ranging from 7×10^{-5} to 4×10^{-3} $M_\odot$ (see Table 5.2). The noise was generally much higher for sources in the Serpens star forming region at 18 hours due to high background flux and source confusion within the fields. Two very embedded objects, Serpens SMM 3 and SMM 4, were also serendipitously

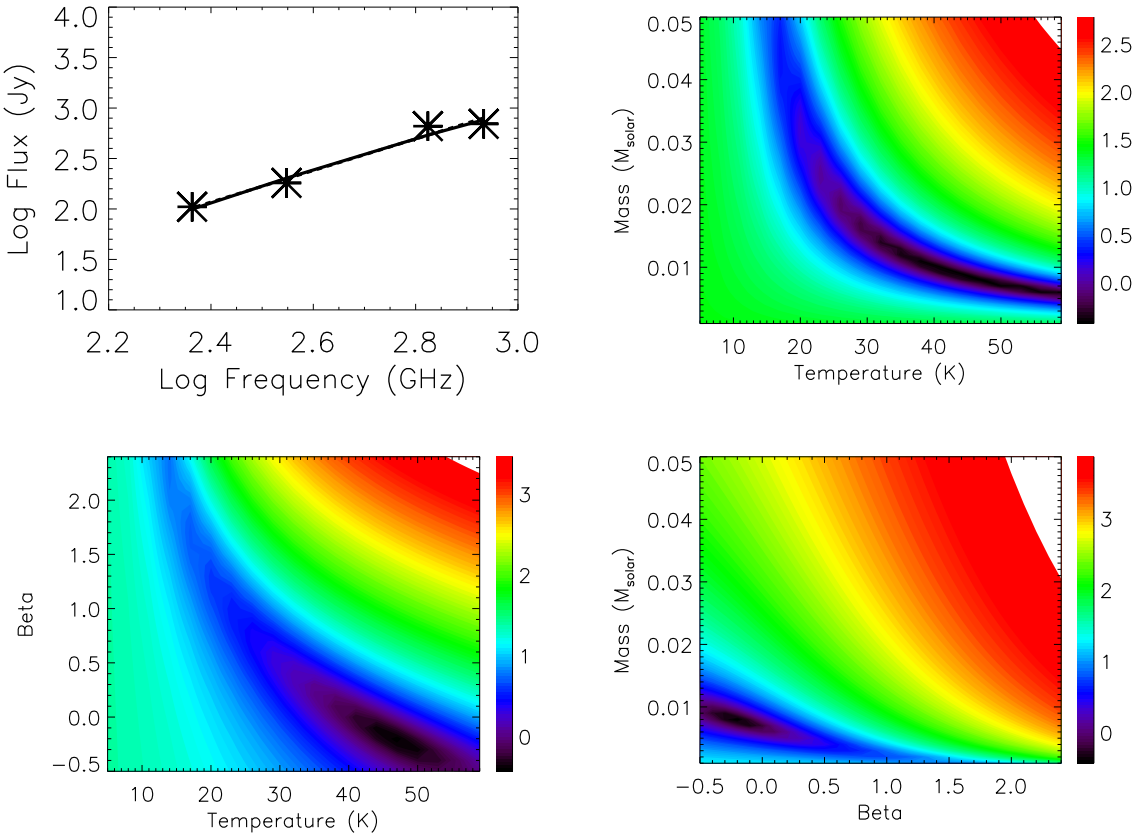

Figure 5.2 Model of DoAr 44. (Top left) Submillimeter photometry (stars) plotted in log flux - log frequency space. The solid line is the model fit and the dashed line is the linear fit used to calculate α. (Top left) Log reduced χ^2 for mass and temperature assuming the best fit β value. The dark purple correspond to the lowest χ^2 values. (Bottom left) Log reduced χ^2 for β and temperature assuming the best fit mass. (Bottom right) Log reduced χ^2 for mass and β assuming the best fit temperature.

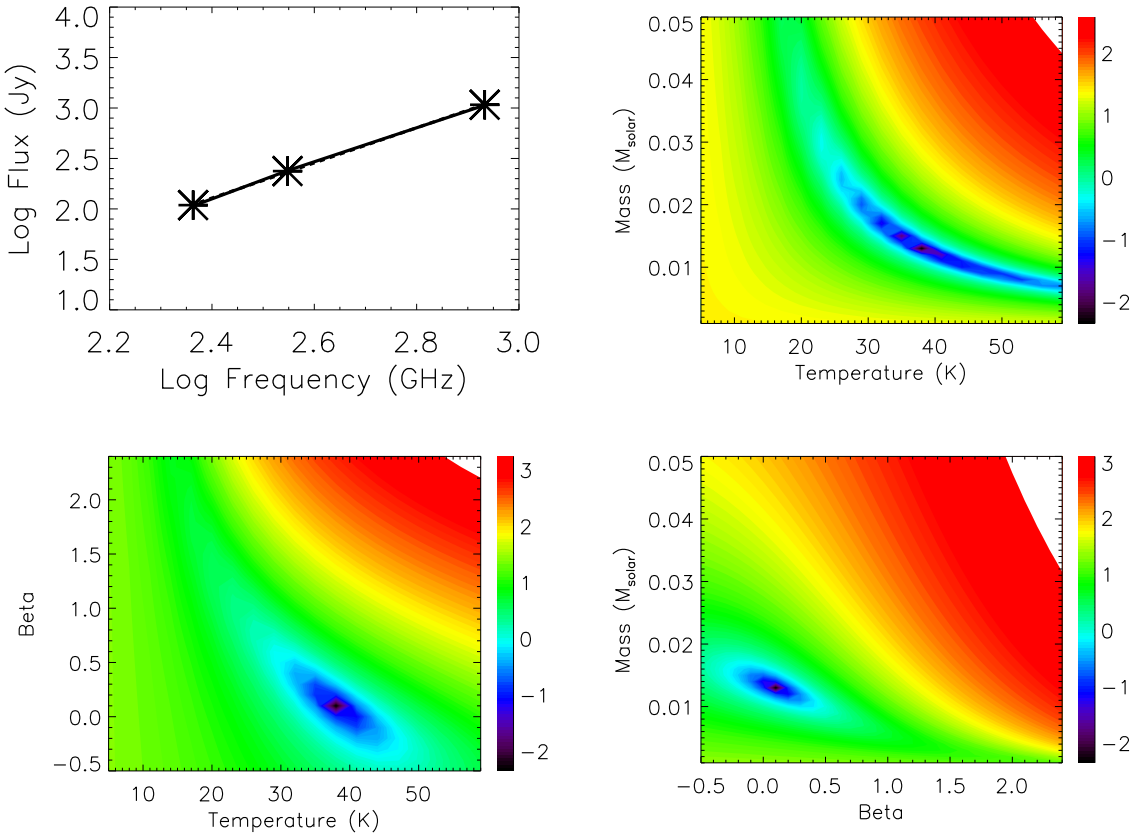

Figure 5.3 Model of DM Tau.

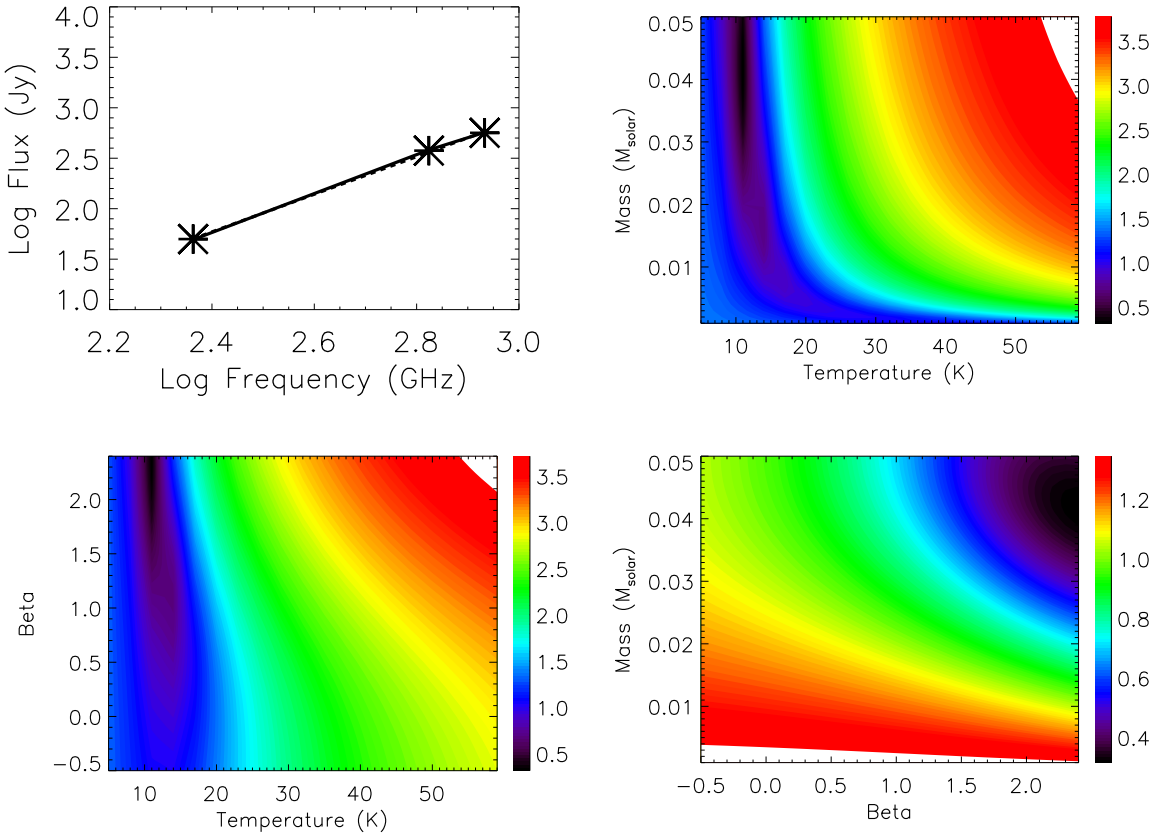

Figure 5.4 Model of GY 224.

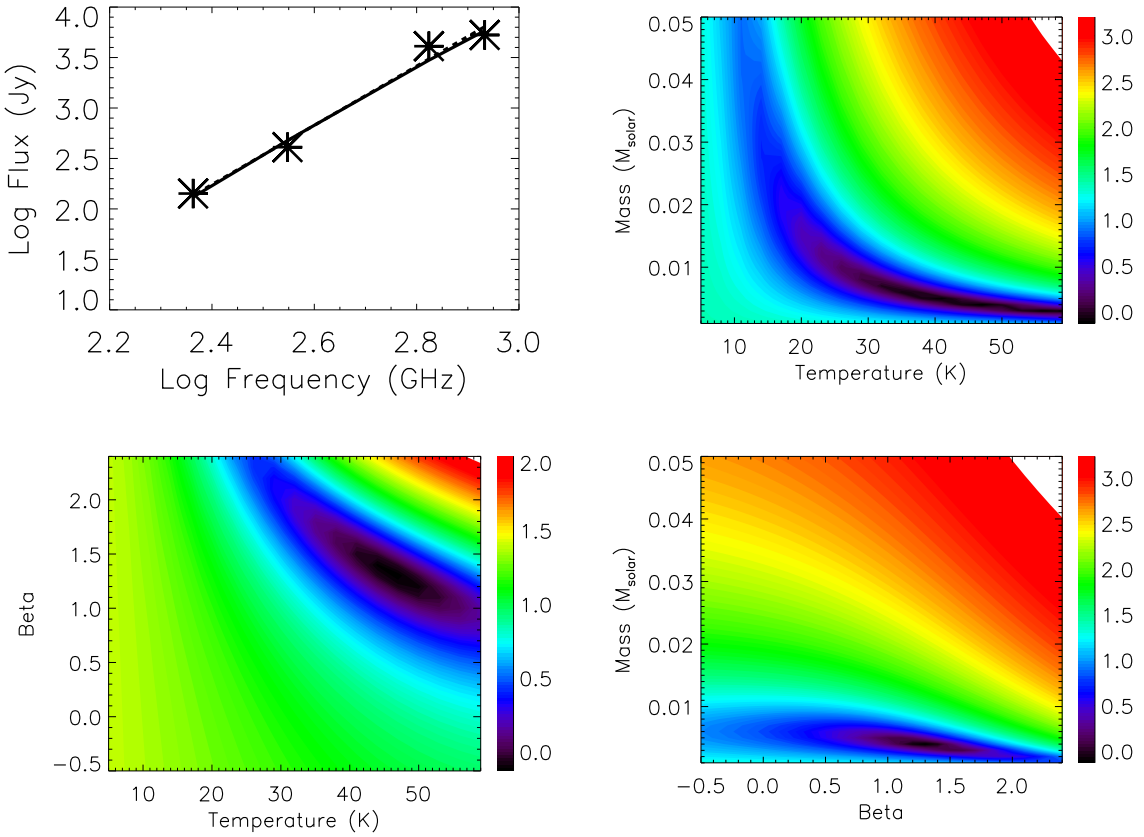

Figure 5.5 Model of HD 135344.

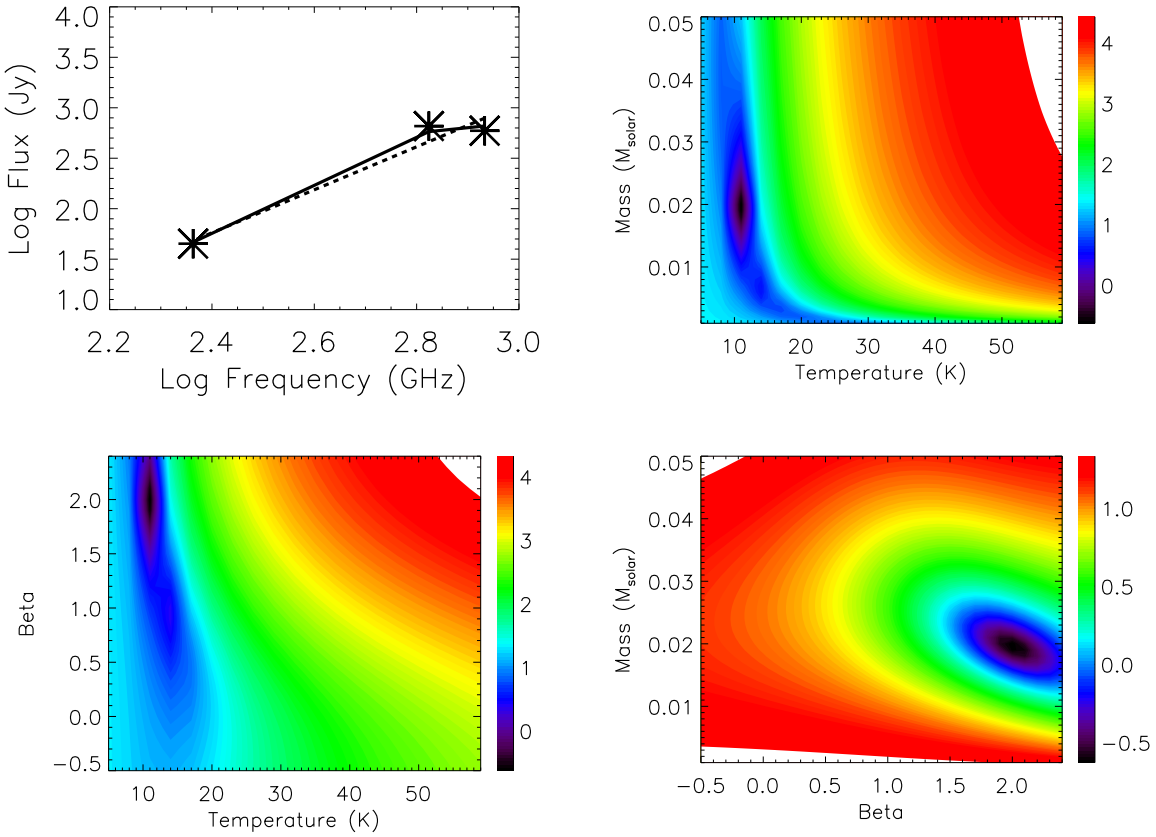

Figure 5.6 Model of IRS 46.

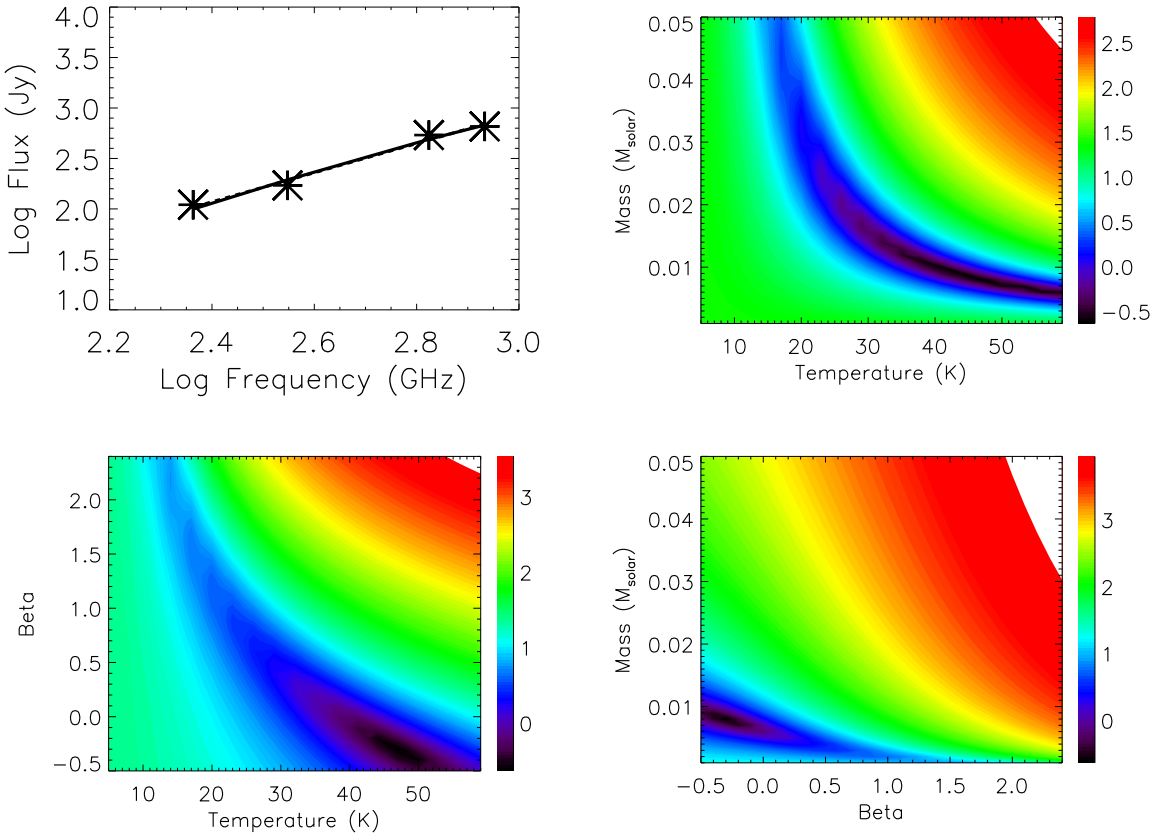

Figure 5.7 Model of IRS 51.

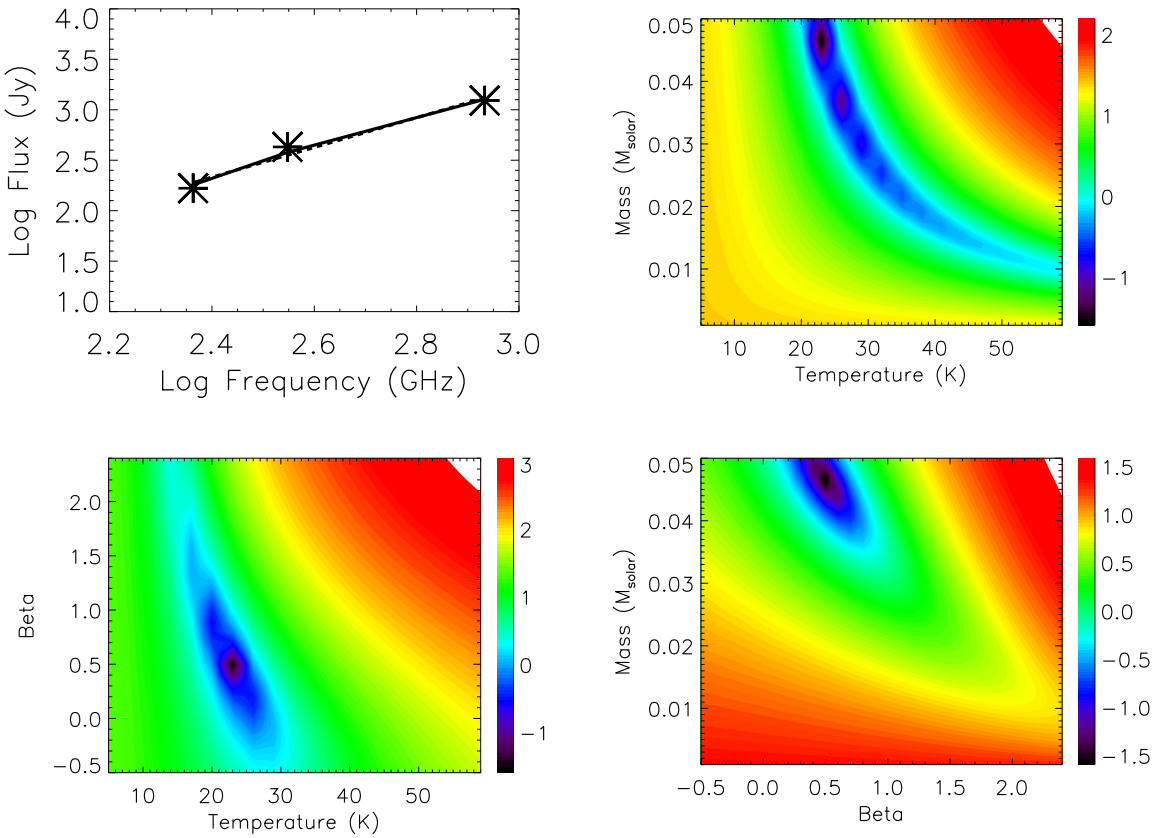

Figure 5.8 Model of LkCa 15.

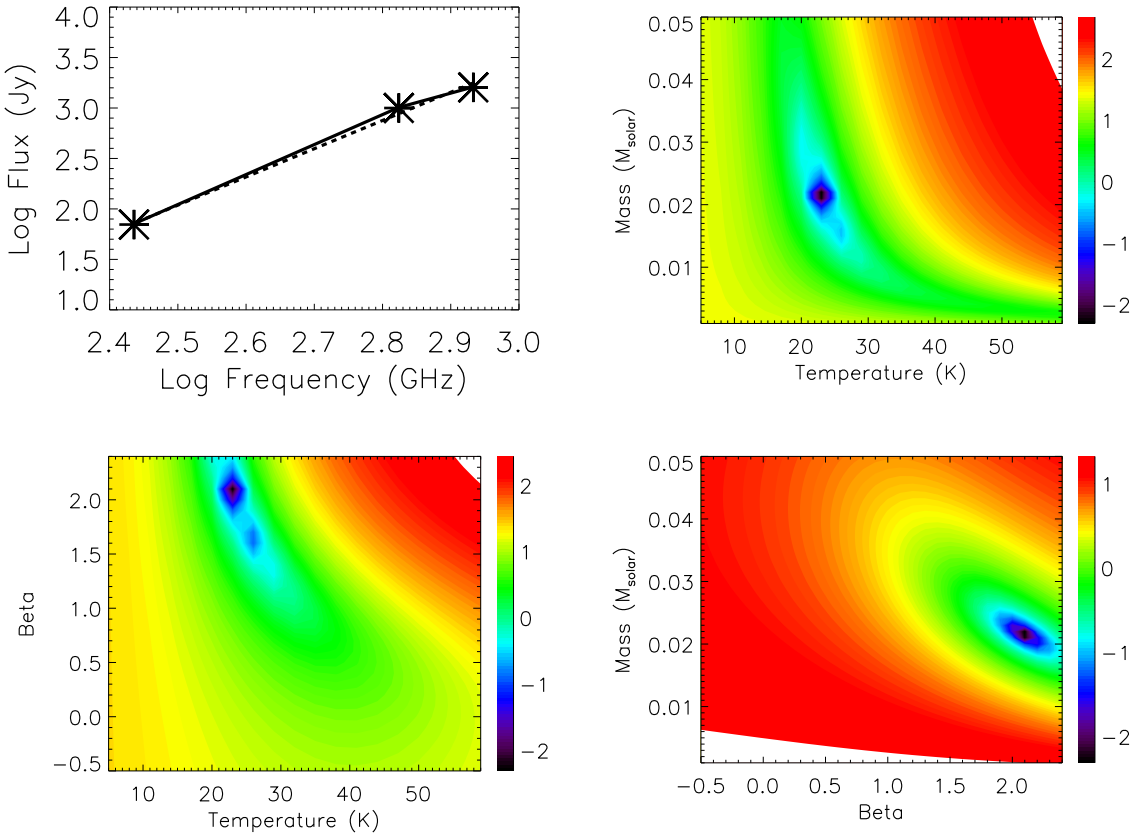

Figure 5.9 Model of lkHα 330.

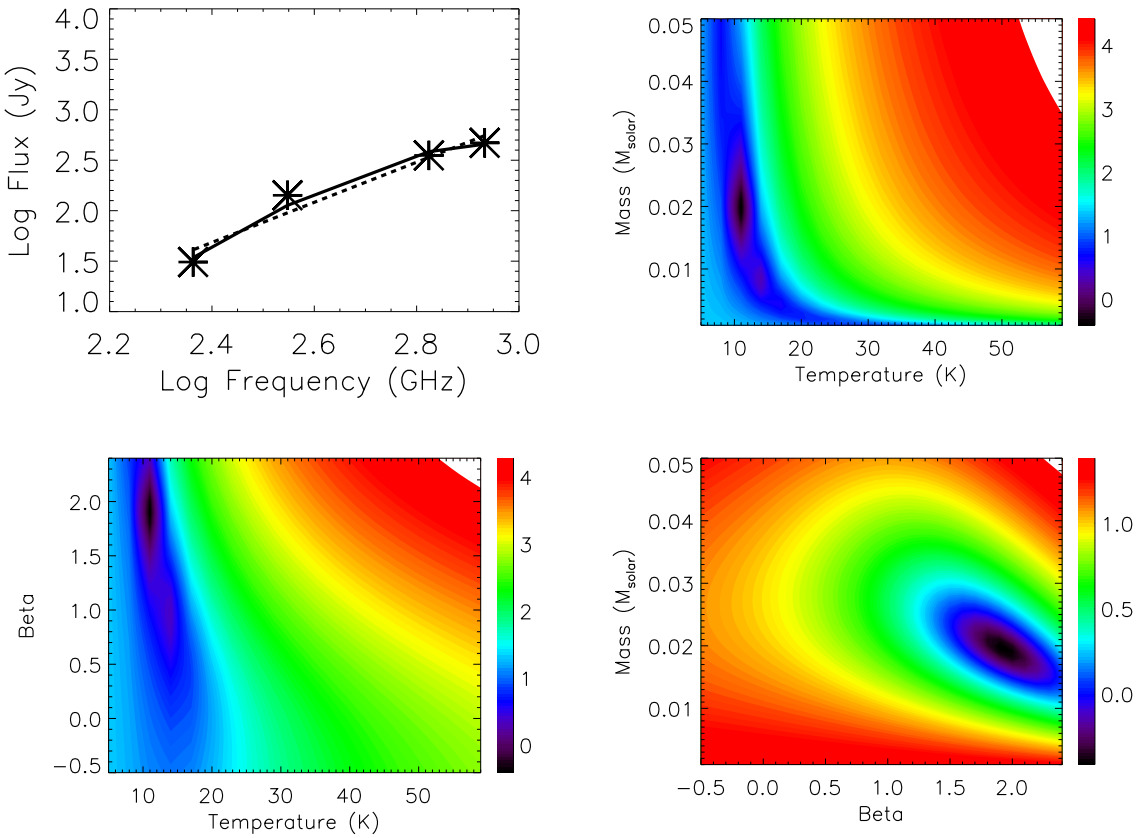

Figure 5.10 Model of SR 4.

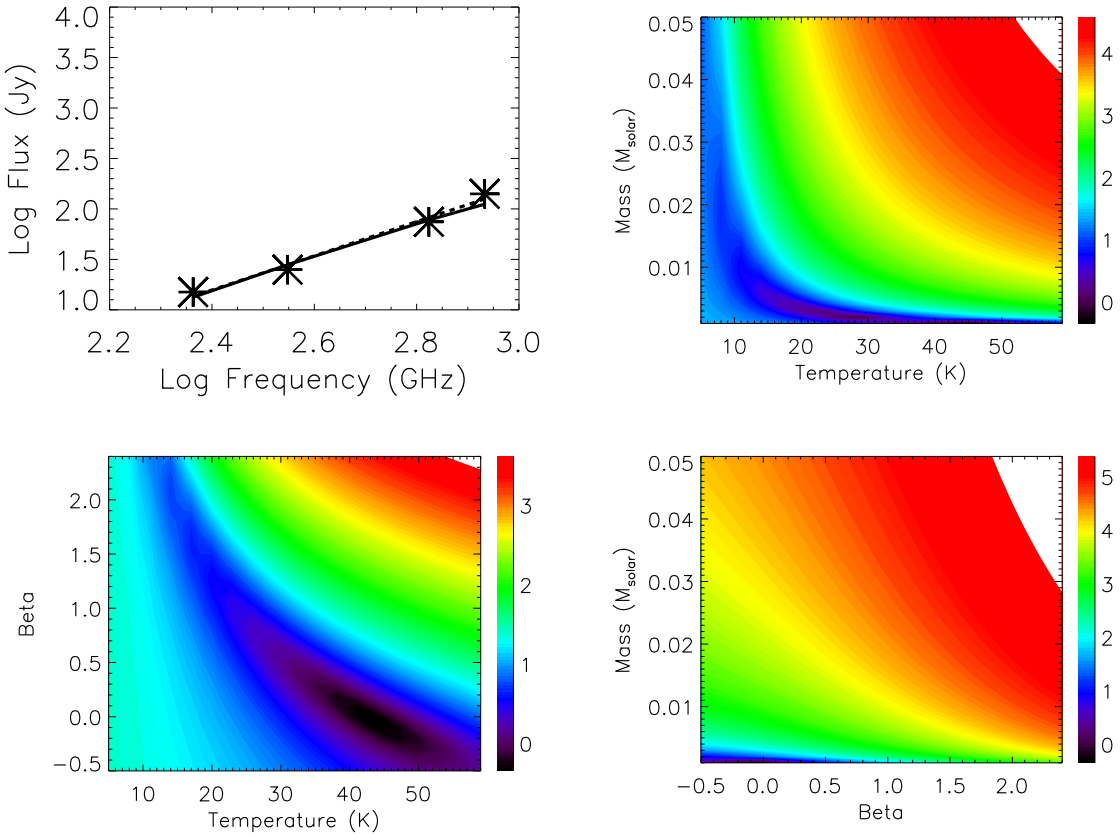

Figure 5.11 Model of SR 9.

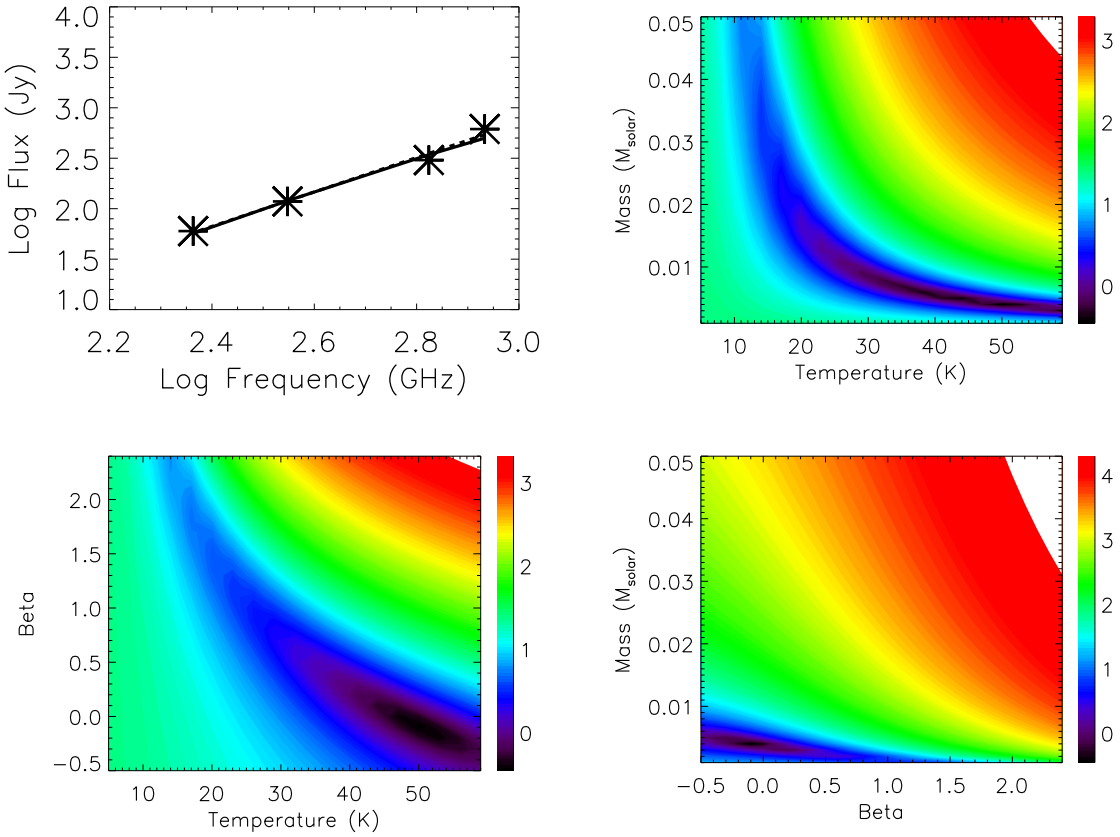

Figure 5.12 Model of SR 13.

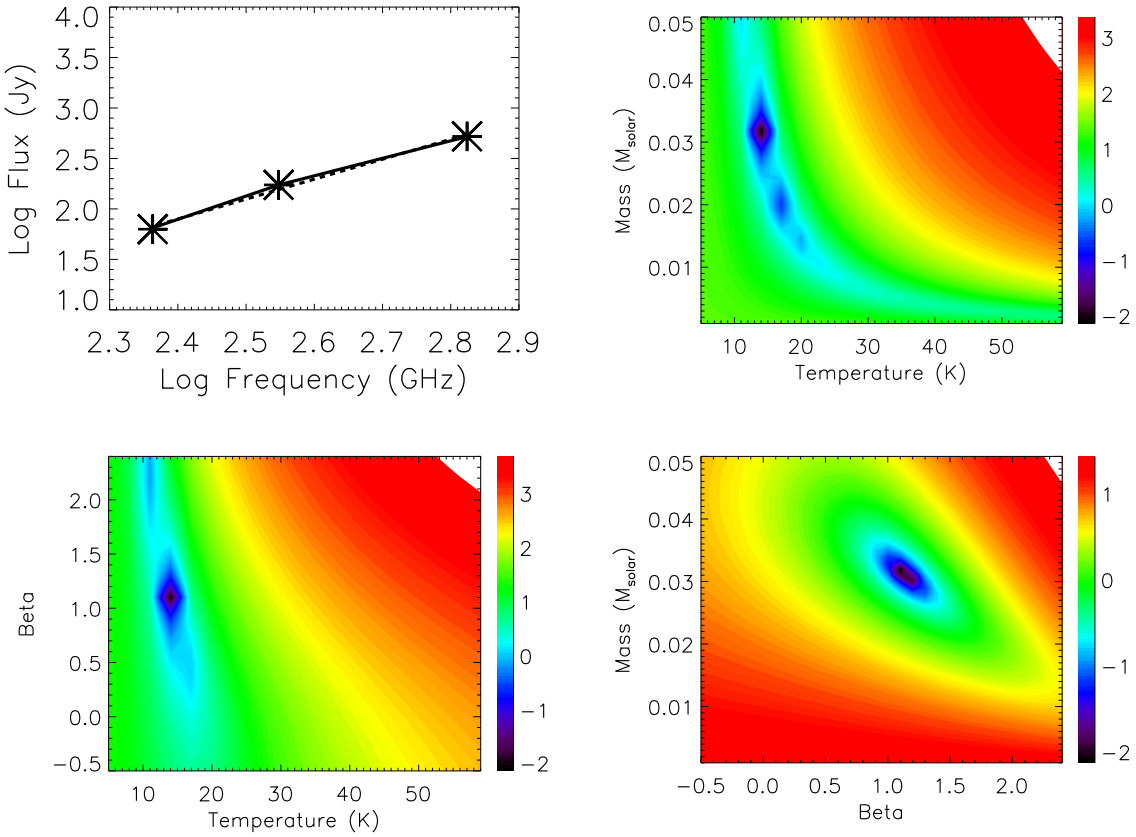

Figure 5.13 Model of UX Tau A.

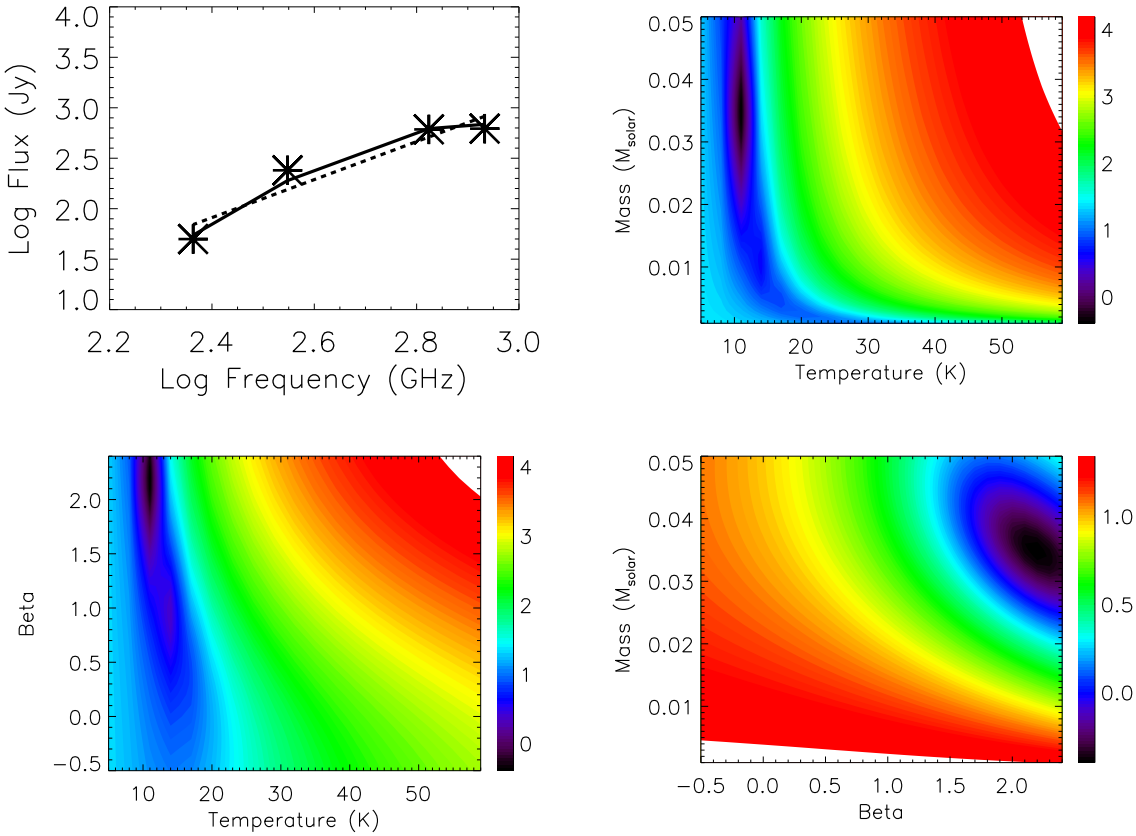

Figure 5.14 Model of VSSG 1.

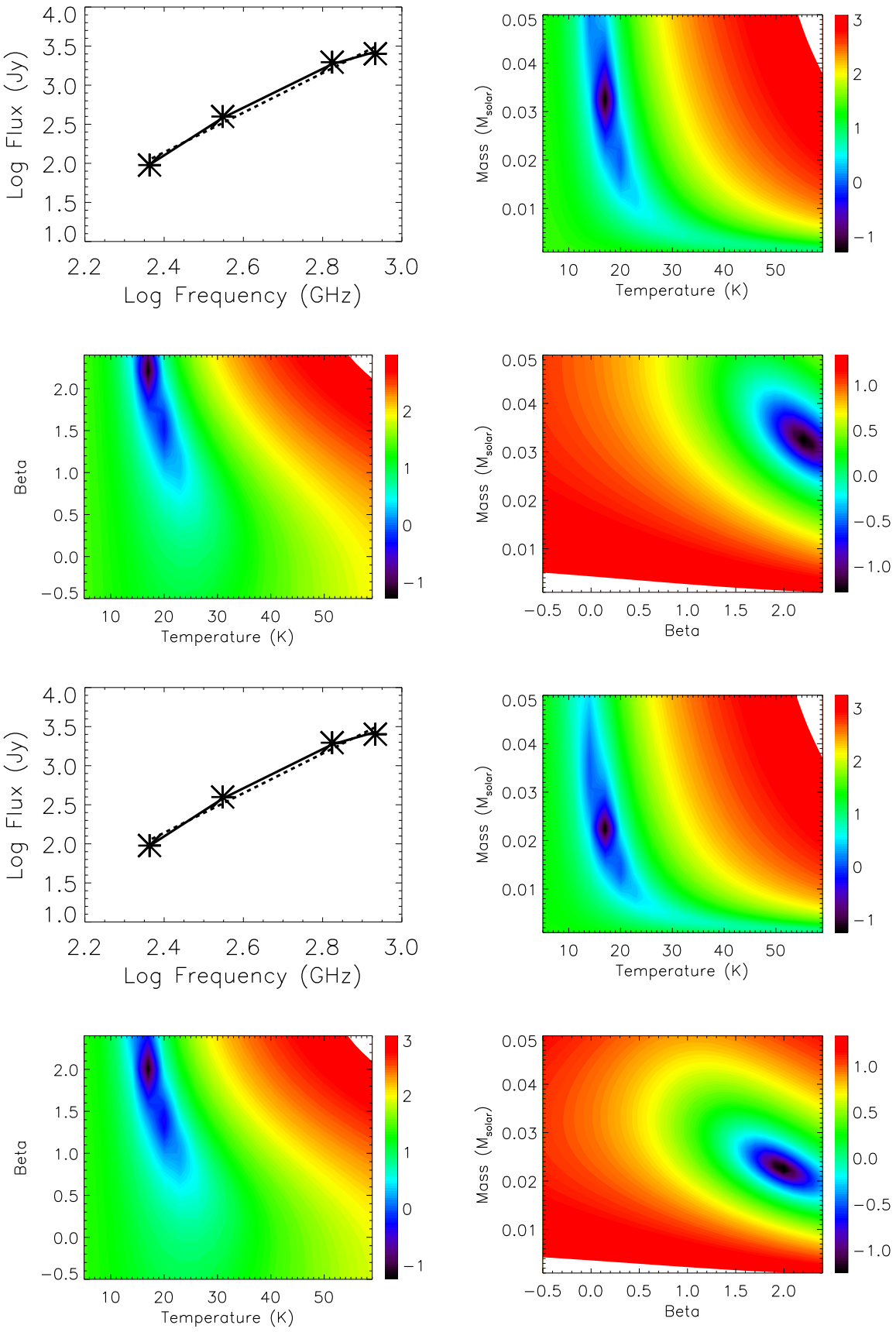

Figure 5.15 Comparison of SR 21 model fits with an inner radius of 0.1 AU (top) and 27 AU (bottom).

observed, and fluxes for these protostars are listed at the bottom of Table 5.1.

All the disks in this sample have α between 1.4 and 3. However, the disks known to contain central holes have, on average, higher α values. A Student's t-test on the two samples to see if this is merely coincidence finds that p is 0.036, so there is a 96.4% chance that they are drawn from two different parent populations. Since the sample size here is so small, I also compared it to the larger sample in Andrews & Williams (2005) and Andrews & Williams (2007a). Only disks with at least 3 different (sub)millimeter observations, including 350 μm fluxes, were included to avoid systematics from comparing different wavelength observations. After this cut, a total of 31 disks were included in the classical disk sample. Comparison with the larger sample decreased p to 0.098 or 90.2%. However, the LkCa 15 disk, included in the cold disk sample, does not show an SED deficit (Robitaille et al., 2007) unlike all the others – although it has a 50 AU radius hole in the 1.3 mm dust continuum (Piétu et al., 2006). Without LkCa 15, p drops to 0.006 (99.4%) and 0.028 (97.2%) respectively, indicating a statistically significant difference between SED-identified cold disks and the general population of young disks around classical T Tauri stars.

One of the most noticeable features from the modeling is that α does not equal 2+β. The indication, then, is that β is tracking not just changes in opacity but also serves as a proxy for frequency dependent effects in τ. One physical cause for such deviations is contamination by optically thick material. Indeed, this can be seen when examining the optical depths calculated in the model, which often greatly exceed τ = 1, especially in the inner grid cells. Also, the assumption that the submillimeter fluxes should be in the Rayleigh-Jeans limit of $h\nu << kT$ breaks down if the disks are very cold leading to $\alpha \neq 2+\beta$. At 20 K, for example, the Rayleigh-Jeans assumption leads to only a 2% error in approximating $\exp(h\nu/kT)$ as $1+h\nu/kT$, but at 10 K this increases to almost 25%.

LkHα 330 and SR 21 have very large values of β from the model results, although this is not the case for all of the cold disks. Part of this effect could result from the assumption that the disk inner radius lies at 0.1 AU. Using an inner radius placed at the hole edge determined previously (see Chapters 2 and 3) produces a significantly smaller β value without significantly changing the mass and temperature necessary to fit the data (see Figure 5.15).

5.5 Discussion

The inner holes in the cold disks can be seen in the submillimeter via the steeper submillimeter colors derived for these systems as compared to classical disks. In particular, cold disks discovered

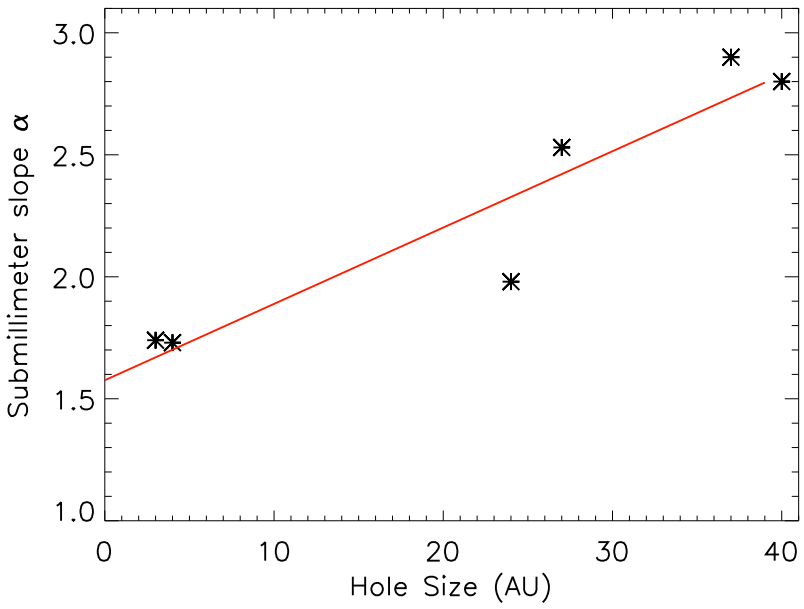

Figure 5.16 Submillimeter slope, α, compared to hole size. Disks with larger holes have larger values of α lending support to the theory that the differences in α values are largely due to opacity differences in the inner disks.

through SED-based searches show high α values, with a mean of 2.40. These disks are likely to be optically thin as $\alpha \approx 2+\beta$, unlike their non-cleared counterparts. Since the most optically thick regions of disks are those at small radii where the mass surface densities are high, decreasing the dust density in the inner regions of the disk disk will naturally make the submillimeter emission more optically thin, all else being equal. Thus, if the differences in α seen in the cold disks are due to inner disk opacity rather than grain growth, the disks with the largest holes, LkHα 330 and HD 135344B, should have the largest values of α. This is indeed the case, and a strong trend of larger α with larger hole size can be seen in Figure 5.16. Therefore, the submillimeter slope differences are likely due to the intrinsic differences in the physical disk structure rather than changes in grain properties.

The case of LkCa 15 is particularly interesting as it was found to have a 50 AU radius central hole in millimeter images but does not have steep submillimeter colors. This likely indicates that the evolution of this disk has been different than the other cold disks. It thus seems unlikely that submillimeter photometric searches would be an effective method to discover cold disks, as steep submillimeter slopes are also seen from optically thin objects with small grains.

The purported transitional disks found via submillimeter searches appear, in general, to be optically thick classical disks. For these disks, α is not statistically different from the larger sample, and β is generally less than 1, likely indicating optically thick material. While the disks are brighter at submillimeter wavelengths, thus facilitating detection, optically thick contamination is a serious problem for the interpretation of 350 and 450 μmphotometry.

An alternative to actually losing the dust in the gap, either onto the star or into protoplanets, is that it has become unobservable. Multi-wavelength submillimeter observations measure the state of grain growth through sizes of $\sim$1 cm. Grain growth into larger sizes, $\gtrsim$ 1 cm, produces inefficient emission (that is, small values of κ_0) in both the millimeter and infrared, potentially hiding large amounts of disk material. β is affected by both the grain size distribution and the maximum particle size. The steep submillimeter colors derived for the transitional disks mean that the holes in the cold disks are not full of $\sim$100 μm dust grains, although larger planetesimals cannot be ruled out.

The transitional disks studied here are all fairly massive, certainly above the average disk mass of 10^{-3} $M_\odot$ (Andrews & Williams, 2005). While this may be partly a selection effect, higher mass disks may facilitate large gap formation since they are advantageous for the rapid formation of planets, either by core accretion (Pollack et al., 1996) or gravitational instability (Boss, 2001). Holes in massive disks may thus be found preferentially due to the increased contrast between large outer disk and cleared inner hole. The fairly high non-detection limits of this SHARCII survey of additional, lower mass, transitional disks may increase the observational bias, and so deeper searches for submillimeter emission from the full suite of transitional disks uncovered by Spitzer are needed.

5.6 Conclusions

Unresolved submillimeter photometry finds properties of cold disks in agreement with the picture of them as disks with large central holes. The SED-identified cold disks show significantly steeper submillimeter colors, with a mean value of α of 2.37$\pm$0.46 as compared to the general disk population, which has a mean value of α = 2. As the value of α strongly correlates to hole size, this likely indicates that the inner regions of cold disks are optically thin even at 350 and 450 μm, unlike their classical T Tauri star counterparts. In order for the cold disks to show this difference, they must have centrally cleared most $\sim$100 μm sized grains as well as the $\sim$10 μm sized grains visible in the mid-infrared through their silicate emission features.

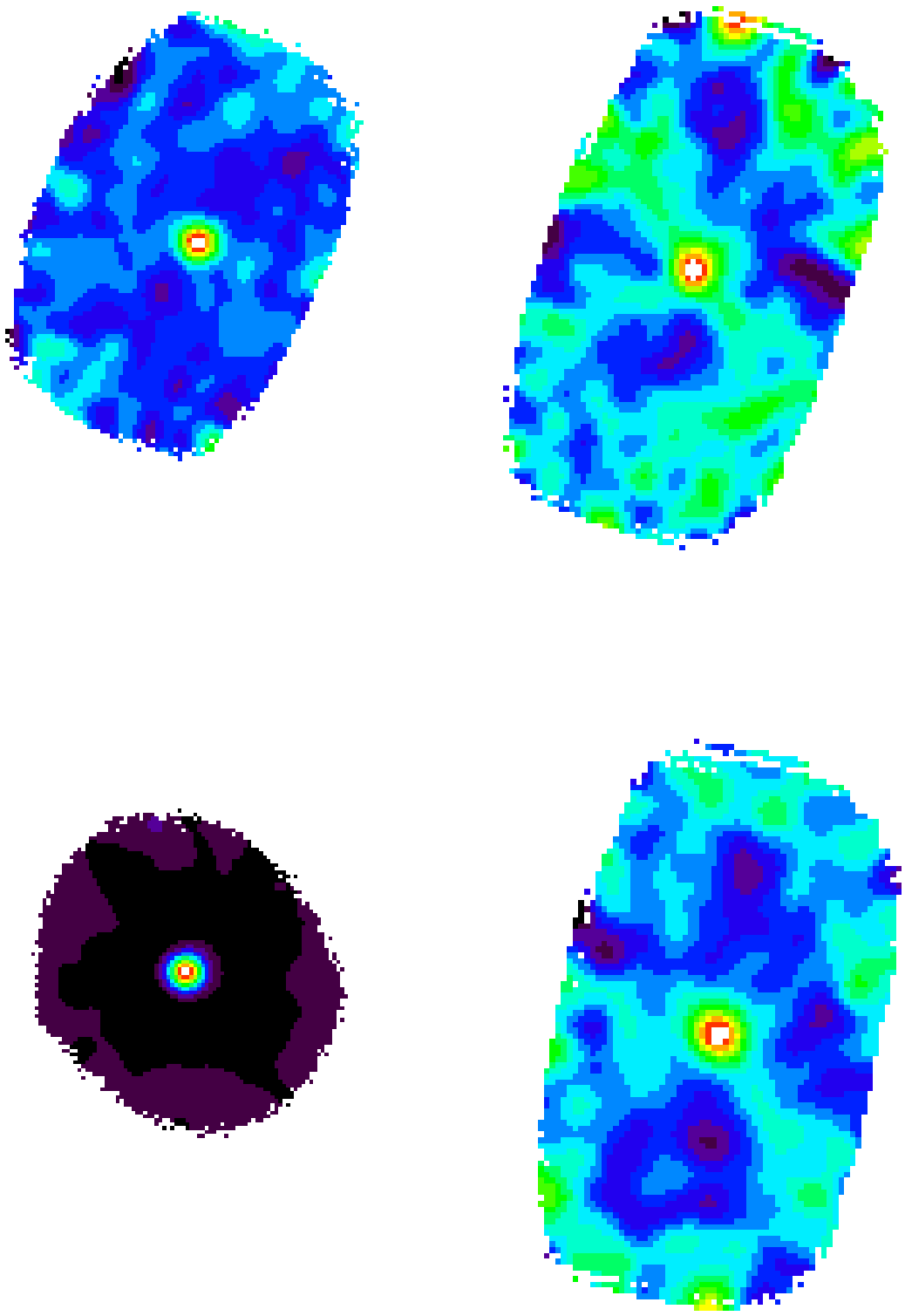

Figure 5.17 CSO 350 μm map of DoAr 44 (top left), SR 4 (top right), SR 21 (bottom left) and VSSG 1 (bottom right).

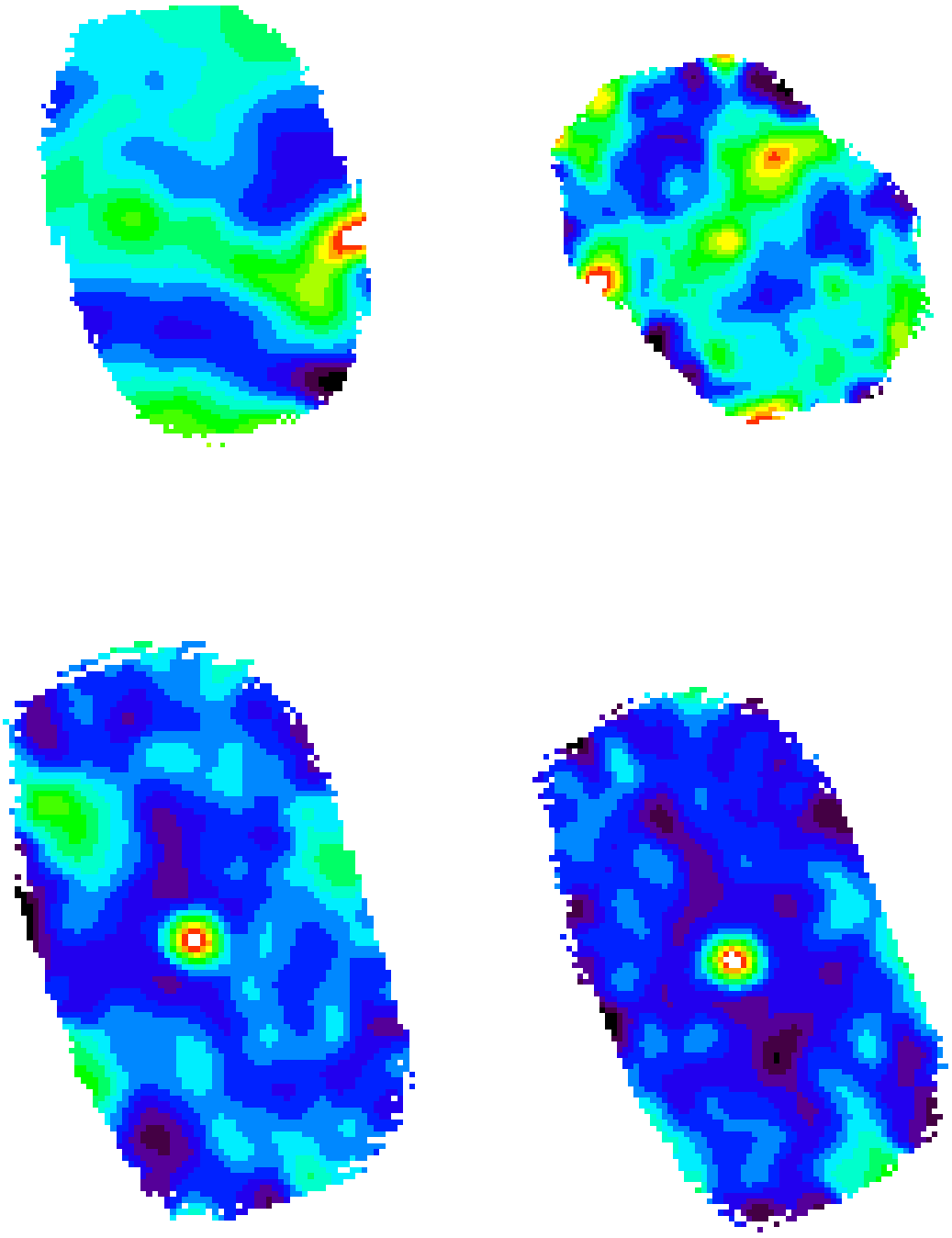

Figure 5.18 CSO 350 μm map of DoAr 24E (top left), SR 9 (top right), IRS 51 (bottom left) and SR 13 (bottom right).

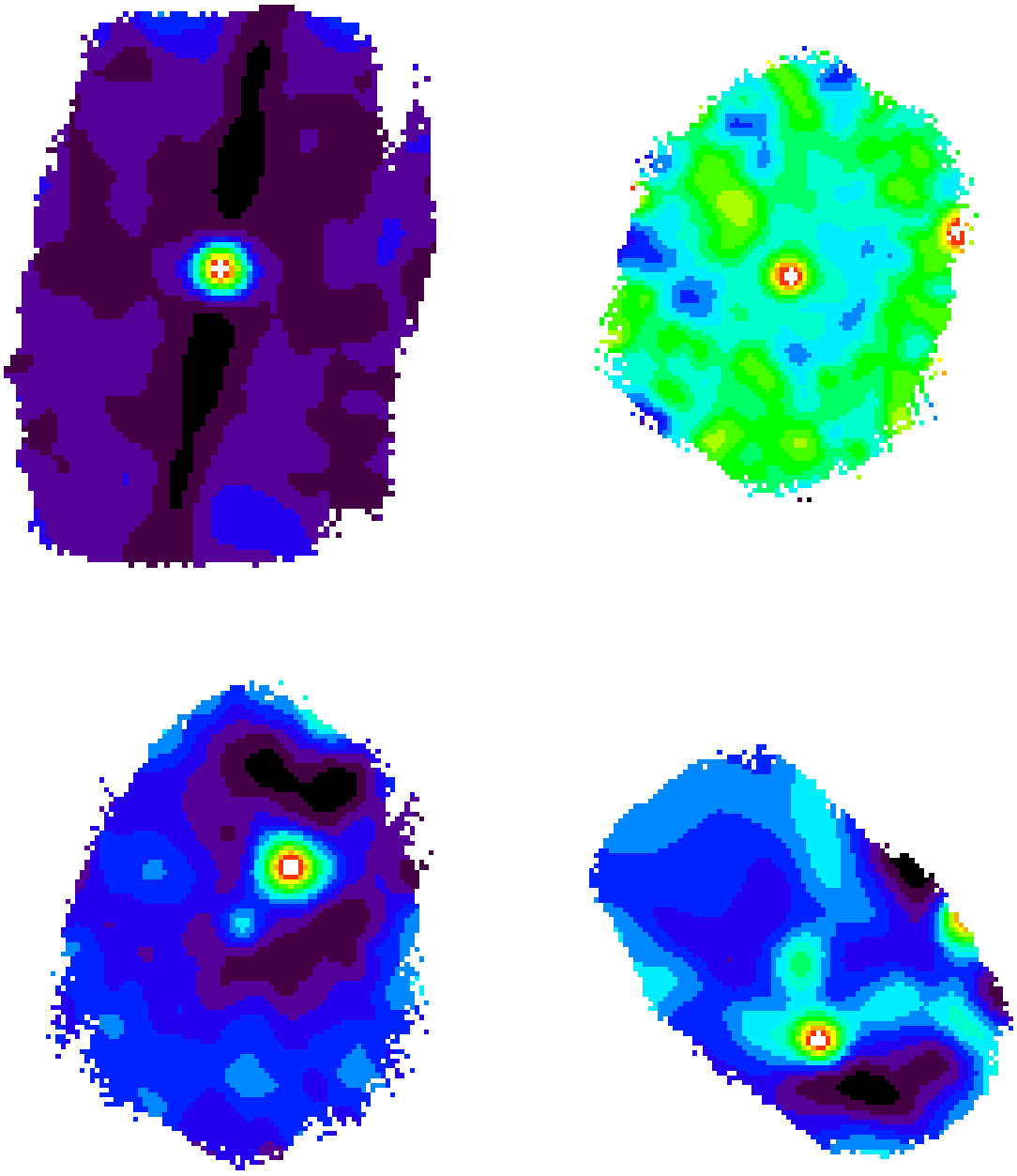

Figure 5.19 CSO 350 μm map of HD 135344B (top left), GY 224 (top right), IRS 46 (bottom left) and EC 90 (bottom right).

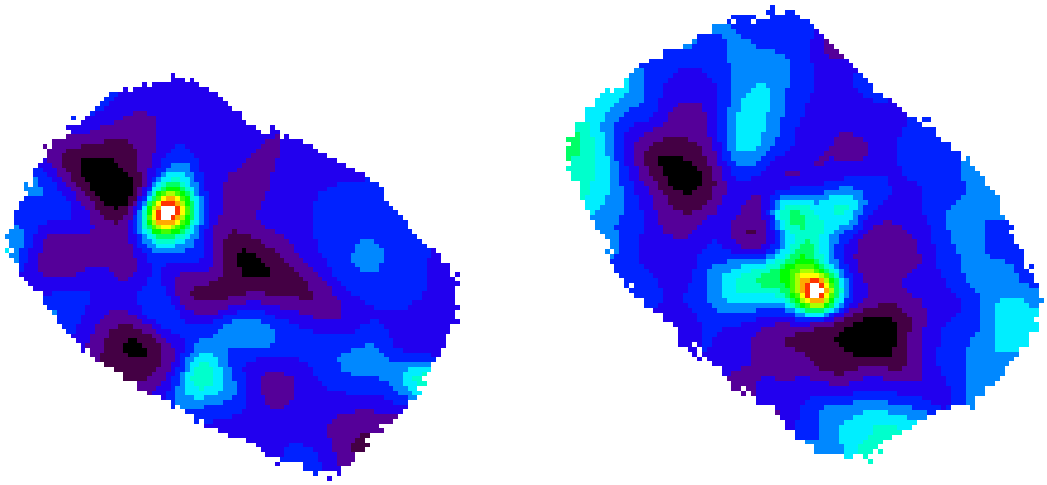

Figure 5.20 CSO 350 μm maps of EC92 (left) and C2D 182953S (right).

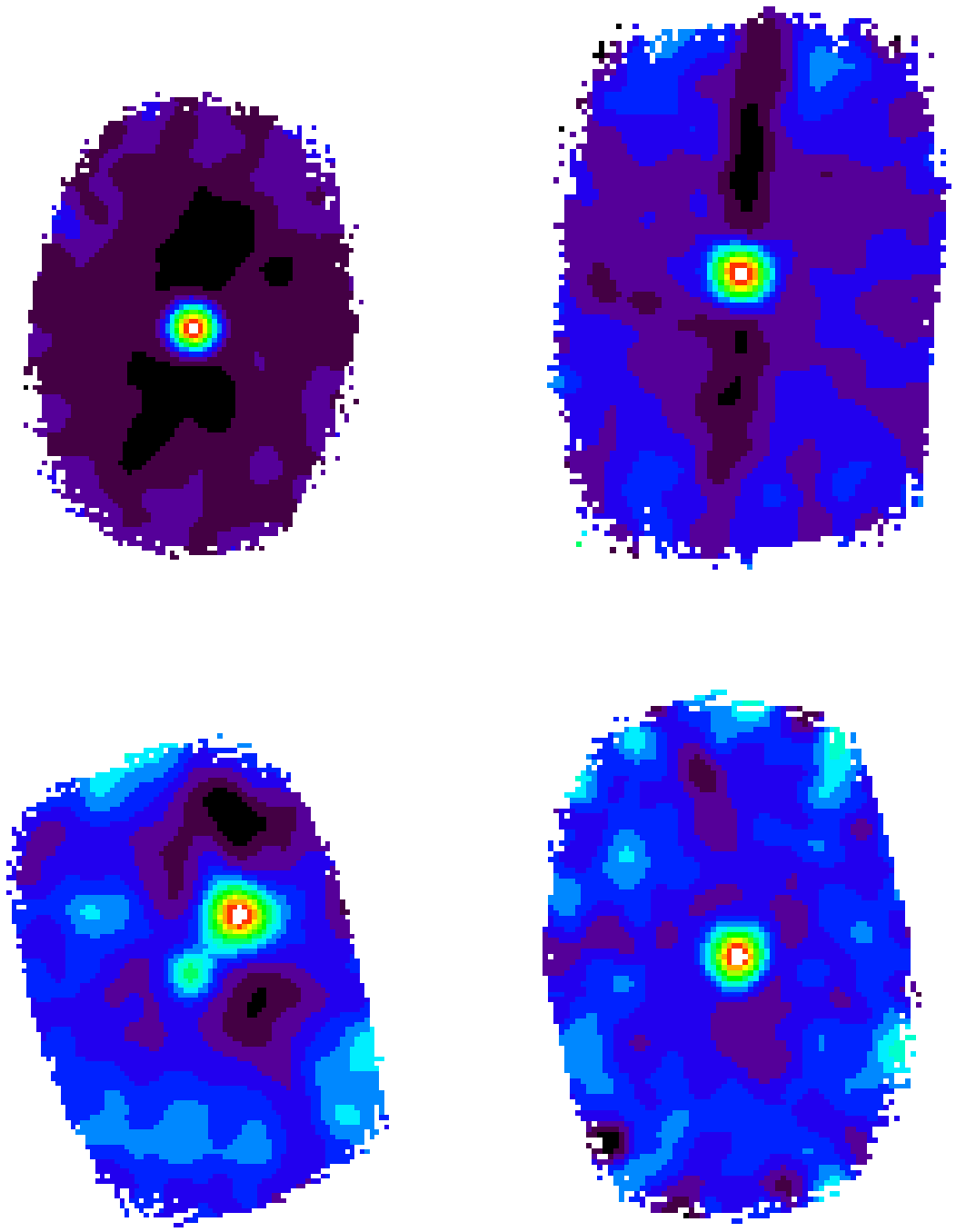

Figure 5.21 CSO 450 μm maps of SR 21 (top left), HD 135344B (top right), IRS 46 (bottom left) and DoAr 44 (bottom right).

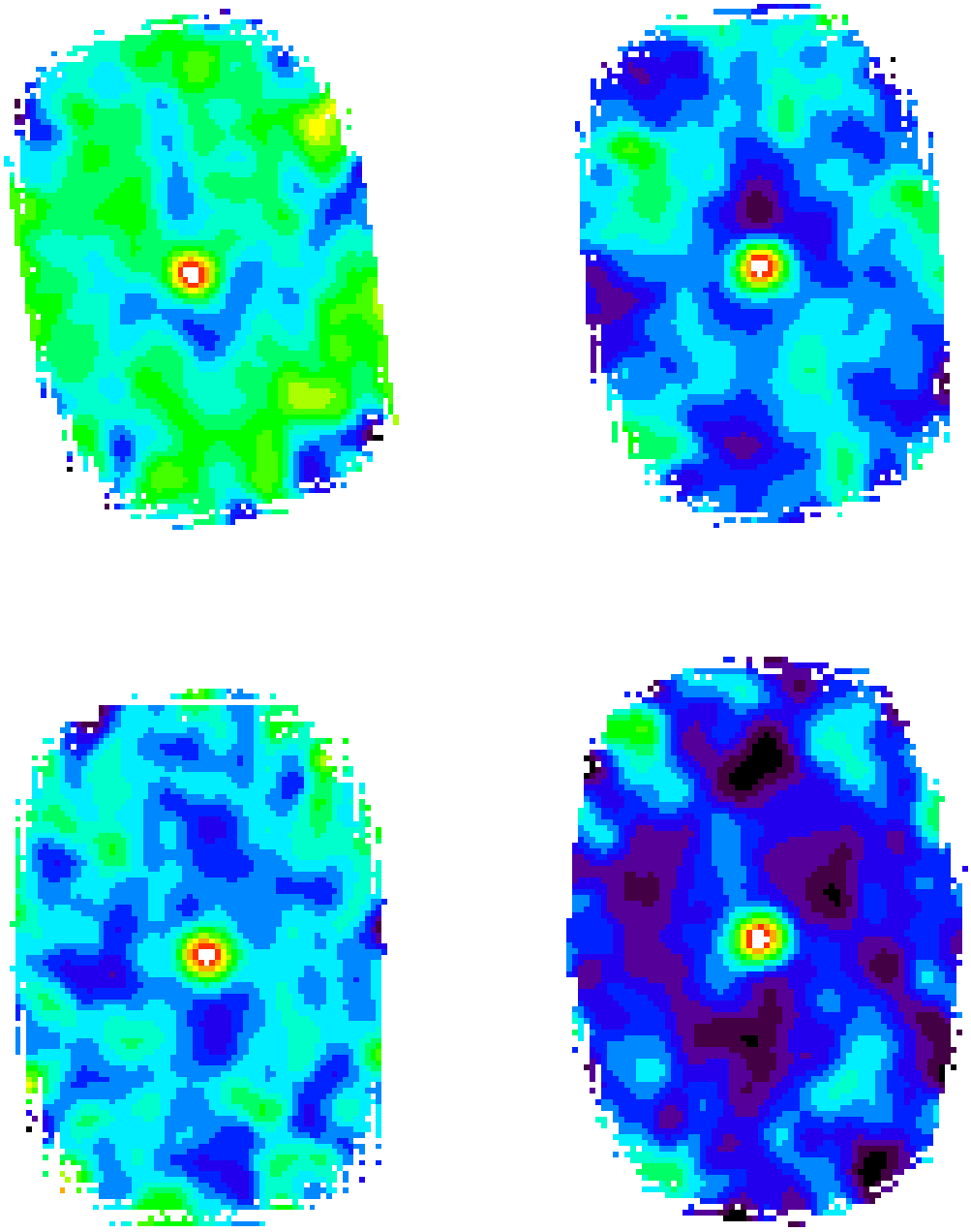

Figure 5.22 CSO 450 μm maps of GY 224 (top left), IRS 51 (top right), SR 13 (bottom left) and SR 4 (bottom right).

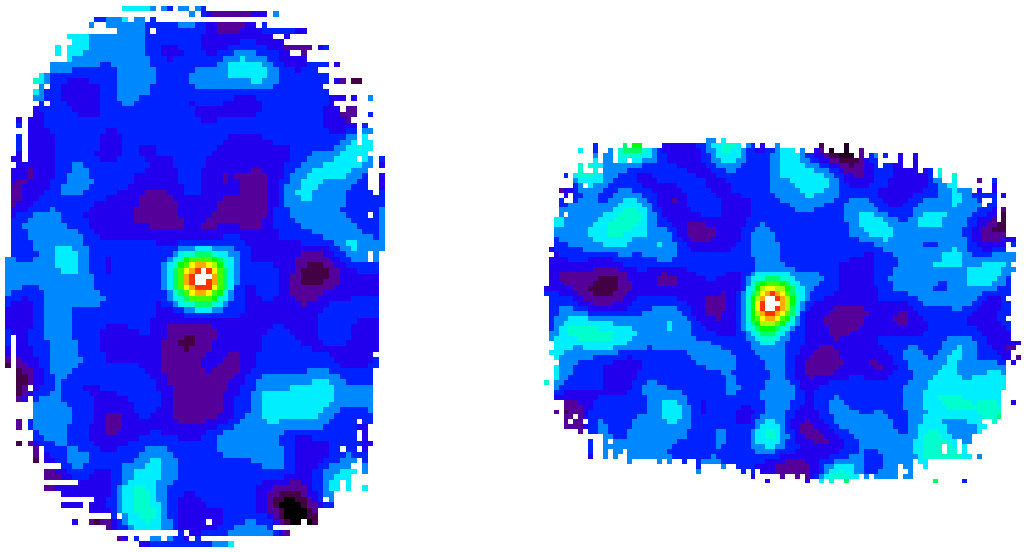

Figure 5.23 CSO 450 μm maps of VSSG 1 (left) and LkHa 330 (right).

Chapter 6

CARMA observations of outer disk properties

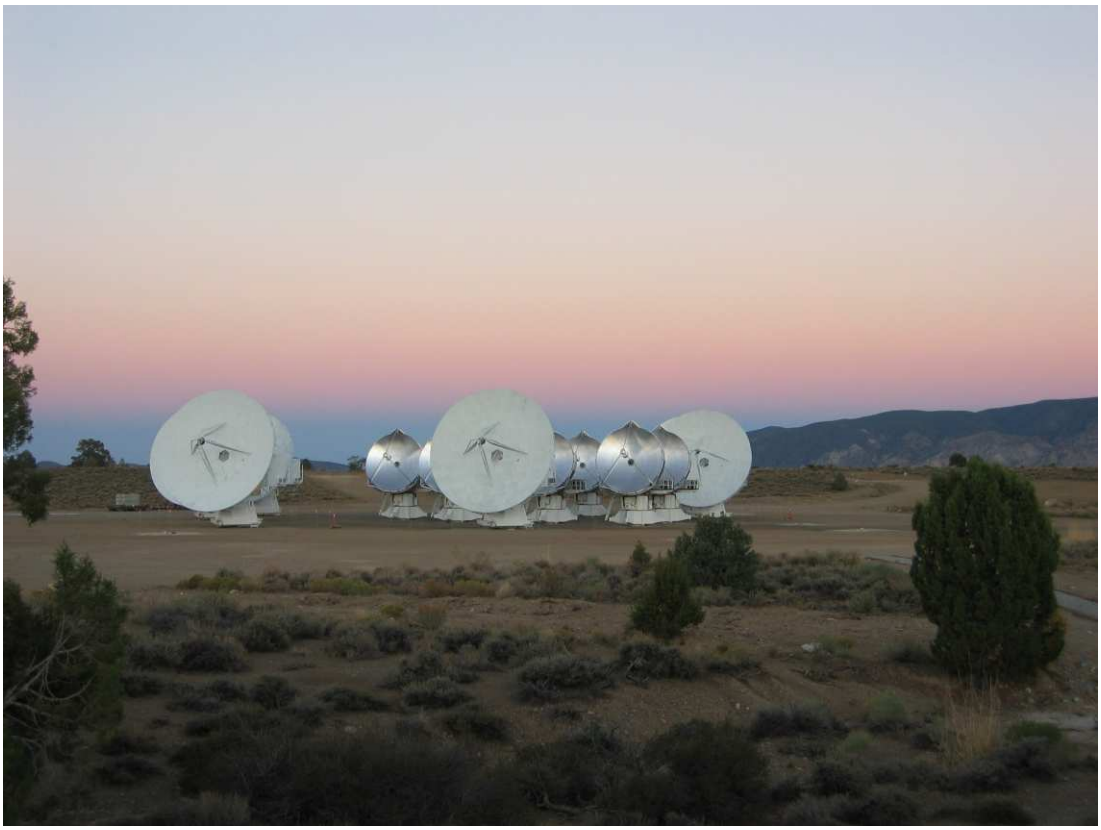

Abstract

In order to probe more optically thin dust than is accessed by SHARCII, I turn to aperture synthesis observations at millimeter wavelengths that provide the potential for resolved imaging of both dust and gas in circumstellar disks. Specifically, the millimeter region contains, in addition to the thermal emission from dust, many strong pure rotational lines that probe the bulk cold gas content at large radii. I have used the Combined Array for Research in Millimeter Astrometry (CARMA) to observe eight transitional disks. CARMA is still a young instrument, with commissioning beginning in 2005 and continuing today for some components, but this array has large potential for improvement in millimeter observational capability. In these preliminary observations I have detected seven disks in the millimeter continuum and one transitional disk, LkHα 330, in the ^{12}CO J=1-0 emission line.

6.1 Introduction

Millimeter interferometers are providing increasingly detailed images of protoplanetary disks. Millimeter dust emission is generally optically thin, allowing estimates of mass distribution and opacity to be made (e.g. Beckwith et al. 1990), and arises primarily from the outer disks, with sizes ranging up to several hundred AU. It has become clear that disk structure is often complex with nonuniform structure visible upon closer examination (e.g. Chapter 3, Corder et al. 2005, Piétu et al. 2006).

Transitional disks are likely candidates for nonuniform resolved structures providing that sufficiently high resolution images can be obtained. Mid-infrared observations, through which transitional disks are usually discovered, probe grains up to tens of AU away from the central star but not the cool outer disk. The apparent evolution of the interior dust leaves intriguing questions about the state of the dust in the outer disk. It is clear from long wavelength Spitzer observations and large millimeter surveys such as Beckwith et al. (1990) and Andre & Montmerle (1994) that such disks often have massive outer disks, but a more detailed analysis of their properties is needed.

Resolved gas images are particularly necessary to determine differences between the dust evolution seen in the SEDs and the more abundant disk gas content. Despite the presence of a gap, most of the transitional disks discussed in this thesis are actively accreting. Rovibrational emission in the CO v=1→0 lines has been detected using Keck/NIRSPEC from the innermost regions for the majority of these sources, but such observations tell us nothing about the gas beyond a few AU (Chapter 4, Rettig et al. 2004, Salyk et al. 2007, Najita et al. 2003). Millimeter wavelengths are rich in low-energy molecular rotational lines, and CO is a particularly stable molecule and thus a good tracer of the bulk gas content, particularly if multiple isotopologues (^{12}CO, ^{13}CO, C^{18}O) are detected. Here, observations of the ground state ^{12}CO J=1-0 (ν=115.271204 GHz) rotational line are used to provide a direct comparison of the cold gas and dust content in trnasitional disks. Resolved gas images can also provide kinematic information which can be used to find disk outer radii, inclination, central stellar mass and, possibly, temperature and density profiles.

The Combined Array for Research in Millimeter Astronomy (CARMA) was used to obtain 3 mm continuum images of seven transitional disks and to search for ^{12}CO J=1-0 emission. One additional disk, UX Tau, was observed at 1 mm and in the ^{12}CO J=2-1 line. CARMA is a heterogeneous interferometer consisting of six 10m and nine 6m antennas. CARMA had first light in 2005 August and these observations were obtained during the shared-risk science period between 2006 October and 2007 May. The C configuration, with baseline lengths ranging between 30 and 350 m, was used

Table 6.1. CARMA 3 mm continuum data

Source	R.A.	Declination	Flux (mJy)	RMS (mJy)	Beam Size
LkHα 330	03:45:48.28	32:24:11.8	9.4	1.07	$2\farcs36$x$1\farcs47$
SSTc2d J033234.1+310056	03:32:34.06	31:00:55.7	3.0	1.07	$2\farcs08$x$1\farcs31$
SSTc2d J032857.0+311622	03:28:57.00	31:16:22.0	3.2	1.07	$2\farcs08$x$1\farcs31$
SSTc2d J034536.9+322557	03:45:36.86	32:25:56.9	–	1.07	$2\farcs07$x$1\farcs31$
SR 21	16:27:10.20	-24:19:16.0	6.63	1.66	$2\farcs77$x$2\farcs44$
DoAr 44	16:31:33.54	-24:27:37.0	23.15	1.07	$2\farcs80$x$2\farcs42$
DoAr 24E	16:26:31.51	-24:19:09.5	22.95	0.91	$2\farcs80$x$2\farcs41$
UX Tau*	04:30:04.0	18:13:49.5	91.1	3.06	$2\farcs76$x$2\farcs22$

*Measured at 1 mm

at 113 GHz providing beam sizes of $\sim 2''$. UX Tau and one track on LkHα 330 were observed in the more compact D configuration. A total of 2 GHz IF bandwidth, including the lower and upper sidebands, was placed in the wideband continuum mode of the CARMA correlator with channel widths of 31 MHz (94 km/s) in each of the two 500 MHz bands. In order to determine the CO gas density, one correlator band was set to a 64 channel 8 MHz (0.3 km/s per channel) spectral line mode to detect ^{12}CO J=1-0 emission, providing sufficient resolution to probe the disk kinematic structure using the line shape. The data were reduced using standard Miriad routines (Sault et al., 1995).

Quasars were used as phase calibrators and were observed every 25 minutes to correct for atmospheric and instrumental phase drift. In the 500 MHz bands, the passband was calculated over a large time interval using both the phase and passband calibrators. Calibrator fluxes were bootstrapped from planet observations taken close in time.

Calibration of the narrow 8 MHz band is more difficult. There is not enough signal in the narrow channels to directly calibrate on even the brighter quasars. Instead, the atmospheric phase solution was transfered from the 500 MHz continuum bands, which leaves a constant in time DC phase offset. This offset was corrected for by combining all available signal from the calibrators in the 8 MHz band. The passband was corrected using a stable noise source which removes all high frequency structure introduced by the correlator.

Table 6.2. Measured disk properties from continuum data

Source	Disk mass ($M_\odot$)	Disk sizes
LkHα 330	0.028	$2\farcs36$x$2\farcs01^+$
SSTc2d J033234.1+310056	0.0078	unresolved
SSTc2d J032857.0+311622	0.0083	unresolved
SSTc2d J034536.9+322557	$<$0.0086	–
SR 21	0.0048	unresolved
DoAr 44	0.017	unresolved
DoAr 24E	0.017	unresolved
UX Tau*	0.0088	$3\farcs2$x$2\farcs8$

+The LkHα 330 disk is resolved only along the minor access of the beam.

*Measured at 1mm

6.2 Dust continuum

Dust continuum emission was detected from 7 of the 8 sources observed, and images are presented in Figures 6.1 to 6.13. The fluxes and RMS noise are in Table 6.1 along with the source position from the literature and the synthesized beam.

6.2.1 Disk masses

Since disks are largely optically thin by 3 mm, disk masses can be calculated from the continuum fluxes (see Chaper 5 for details; symbols used here are as in Chapter 5) such that

$$F_\nu = \frac{2k < T >}{D^2}\frac{\nu^2}{c^2}\kappa_\nu M_D. \tag{6.1}$$

The masses calculated from the CARMA fluxes are listed in Table 6.2.

6.2.2 Resolved imaging

One of the main advantages of imaging disks with an interferometer is that the latter are sensitive to small size scales. However, in the C configuration used for most of these observations, only the LkHα 330 disk is marginally resolved at 3 mm. UX Tau was observed at 1 mm in the D config-

uration and is clearly resolved. According to the stellar positions from Correia et al. (2006), the CARMA-detected disk surrounds UX Tau A, the primary component of the binary+binary system. However, UX Tau D, which lies only 2.″692 south of UX Tau A, is just beyond the extent of the measured disk (see Figure 6.8). DoAr 24E is also part of a binary system, and both components are marked in Figure 6.4 (McCabe et al., 2006).

6.3 CO J=1-0 emission

The CO J=1-0 rotational line traces cold gas in the outer disk. It is commonly seen in Herbig Ae/Be and classical T Tauri disks (Qi et al., 2003). LkHα 330 was the only disk in the transitional sample from which CO 1-0 emission was detected. The emission was resolved with major and minor axes of 4.″2x3.″1 and a position angle of 50°. Deprojecting the observed disk axes assuming a circular disk structure gives an inclination of 42°. Following the calculation outlined in Section 6.3.1, LkHα 330 has a CO column density of 1.42×10^{17} cm^{-2} and a lower limit on the gas disk mass of 4.6×10^{-4} M$_\odot$.

6.3.1 CO column densities

A CO column density and mass can be calculated from the integrated line flux using simple Local Thermodynamic Equilibrium (LTE) approximations. In such calculations the brightness temperature, T_B, is defined as the temperature at which a blackbody function, B_ν, would emit the observed flux such that

$$B_\nu = \frac{2\nu^3/c^2}{exp(h\nu/kT_B)-1}. \tag{6.2}$$

In the Rayleigh-Jeans limit, $h\nu << kT_B$, so this can be approximated as

$$B_\nu = \frac{2\nu^3}{c^2}kT_B. \tag{6.3}$$

The source function, S_ν, is

$$S_\nu = \frac{\int B_\nu d\Omega_{bm}}{\int d\Omega}, \tag{6.4}$$

where Ω is the solid angle subtended. The brightness temperature is thus

$$T_B = \frac{S_\nu c^2}{2k\nu\Delta\Omega_A}. \tag{6.5}$$

The solid angle in square radians is related to the beam in arcseconds such that

$$\Delta\Omega_A = \frac{\theta_a \times \theta_b}{(2\sqrt{2ln2})^2(206265)^2}, \tag{6.6}$$

where θ_a and θ_b are the FWHMs of the beam along the major and minor axes, $2\sqrt{2ln2}$ is the conversion factor for the Gaussian beam from FWHM to integrated angle, and 206265 is the conversion factor from arcseconds to radians. Substituting in the previous expressions, the brightness temperature is equal to

$$T_B = 7.68 \times 10^6 \frac{S_\nu[Jy]}{2k\nu\Delta\Omega_A}. \tag{6.7}$$

The observed intensity is more accurate when corrected for the instrumental efficiency, η, such that the antenna temperature, $T_A^* = \eta T_B$. The integrated antenna temperature relates to the CO column density, N_{CO}, such that

$$\int T_A^* dv = \frac{8 \times 10^- 5\pi^3 c\nu\mu^2 L N_{CO}}{3kQ(T_{ex})}(e^{-E_l/kT_{ex}} - e^{-E_u/kT_{ex}}), \tag{6.8}$$

where μ is the permanent dipole moment, L is the line strength, E_u and E_l are the energies of the upper amd lower states, respectively, and $Q(T_{ex})$ is the partition function at the disk temperature, T_{ex}. The line strength of the CO J=1-0 line has been measured in laboratory spectra, although necessarily at a higher temperature (T_0 = 300 K) than in a circumstellar disk. The integrated intensities, $I_{\rm cat}$, reported in the JPL Molecular Spectroscopy on-line database in units of nm^2 MHz (Pickett et al., 1998) relate to the line strengths such that

$$I_{cat} = \frac{8\pi^3 \times 10^8}{3hc^2}\nu\mu^2 L Q(T_0)(e^{-E_l/kT_0} - e^{-E_u/kT_0}). \tag{6.9}$$

The rotational partition functions, Q(T), are also reported in the JPL catalog for a variety of temperatures. For ^{12}CO(1-0), Q(300 K) is 108.865, and Q(30 K) can be linearly interpolated from the direct summation values tabulated to be 11.186. So,

$$N_{CO} = \frac{k \times 10^{13}}{hc}(\int T_A^* dv)\frac{Q(T_{ex})}{Q(T_0)}\frac{e^{-E_l/kT_0} - e^{-E_u/kT_0}}{e^{-E_l/kT_{ex}} - e^{-E_u/kT_{ex}}}. \tag{6.10}$$

The disk gas mass, M_{H_2}, can then be calculated using the CO column density following the

procedures from Scoville et al. (1986), which essentially multiples the density by a uniform disk

$$M_{H_2} = N_{H_2} \mu_G m_{H_2} \frac{\pi \theta^2}{4} d^2, \tag{6.11}$$

where μ_G is the mean atomic weight of H_2, m_{H_2} is the mass of one H_2 molecule, θ is the angular diameter (FWHM) of a uniform disk source, and d is the distance to the star. The derived H_2 mass depends on the N_{CO}/N_{H_2} ratio, which we assume is 10^{-4}.

6.4 Discussion

We have detected 7 of 8 sources in dust continuum emission and one, LkHα 330, in the CO J=1-0 line. Disk masses were derived assuming that the emission is optically thin and that the disk temperature is 30 K. The derived masses are generally in good agreement with those presented in Chapter 5. The disk around UX Tau is resolved and large with an extent of 224 AU and an inclination of 29°. The disk around LkHα 330 is also marginally resolved in the dust continuum emission, but it is important to note that the size scales probed here are much larger than the putative hole sizes.

LkHα 330 was the only disk in this sample from which CO emission was detected. The two derived disk masses from the dust and gas emission are not in agreement. The masses differ by a factor of 60 with the dust-derived mass being larger. There are several possible causes for the disagreement. The dust calculation assumes a gas-to-dust ratio of 100, while the CO gas calculation assumes an H_2/CO ratio of 10^4, which should be a safe lower bound. However, if the CO J=1,0 emission is optically thick, the derived gas mass will be too low. Observations in more optically thin isotopes of CO are needed to resolve this discrepancy.

The large number of gas non-detections was slightly surprising. LkHα 330 was the only disk with available data from a second, more compact, configuration. The data were all taken during the shared risk period when the system components were being tested and were mostly taken in the daytime when atmospheric phase variation is greater. One possible additional cause for the non-detections in the C configuration observations may be challenges associated with pointing. The gain corrections for most tracks were around 2, which is anomalously high. The gas emission is likely to be more extended than the dust, as in the case of LkHα 330, due to the rapid decrease in dust emissivity as a function of wavelength and radius (Sargent & Beckwith 1987, Qi et al. 2003). Since

pointing errors affect the edges of the beam more than the center, resolved gas emission is more susceptible to degraded flux measurements from pointing errors.

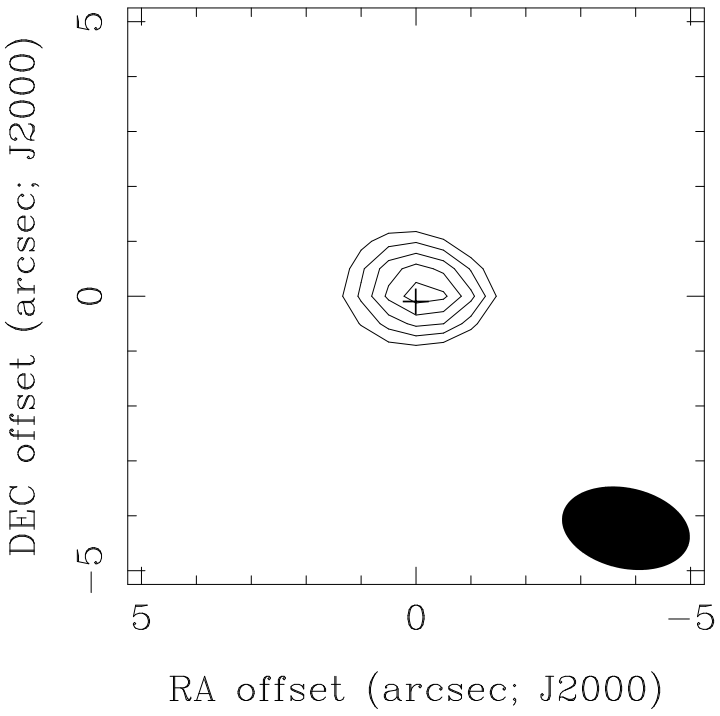

Figure 6.1 CARMA 3mm continuum image of LkHα 330. The cross marks the literature position, also listed in Table 6.1

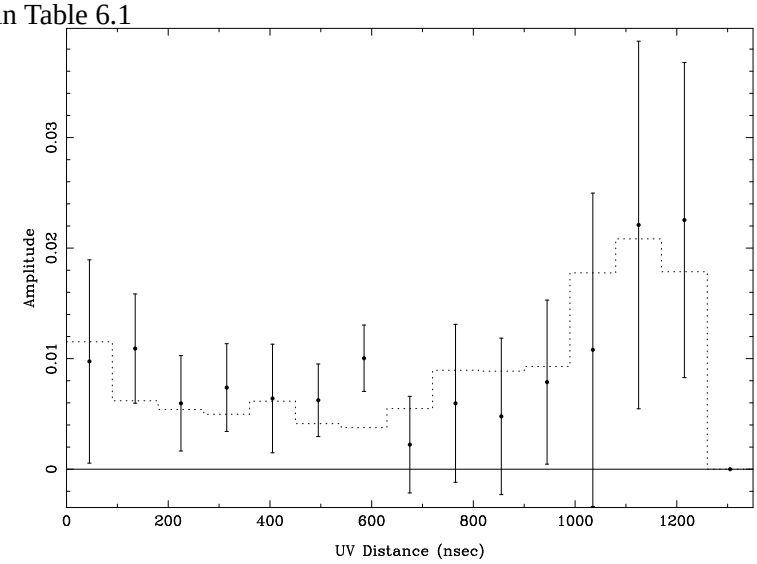

Figure 6.2 CARMA (u,v) plot of LkHα 330. The measured amplitude is plotted against baseline length. The data are binned azimuthally around the central disk position.

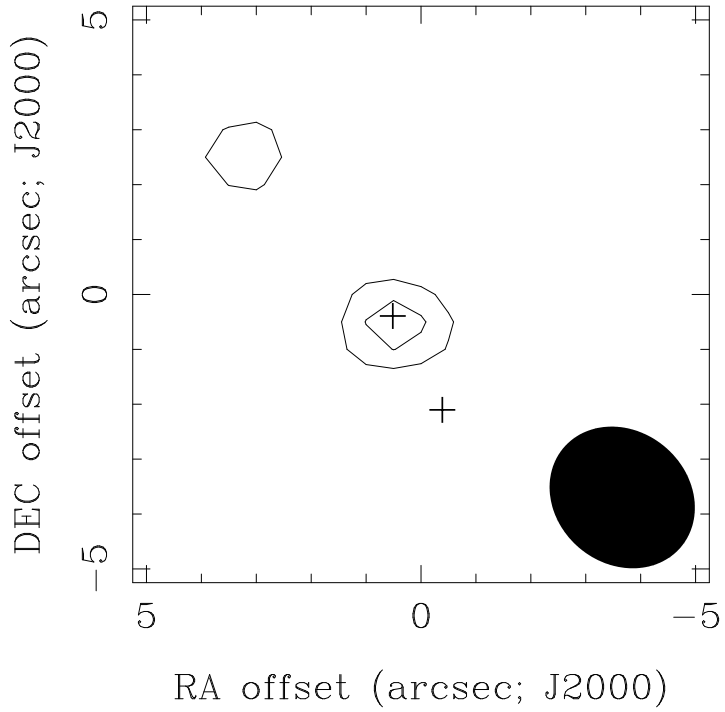

Figure 6.3 CARMA 3 mm continuum image of DoAr 24E. The positions for both binary components are plotted.

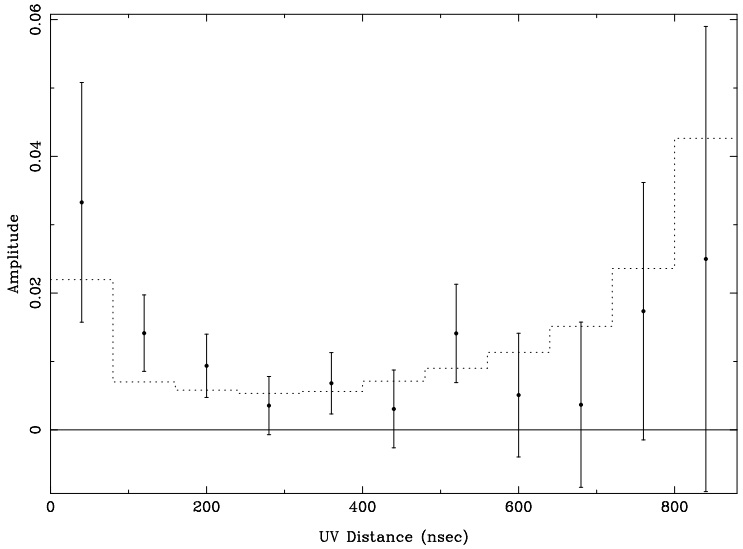

Figure 6.4 CARMA flux versus (u,v) plot of DoAr 24E.

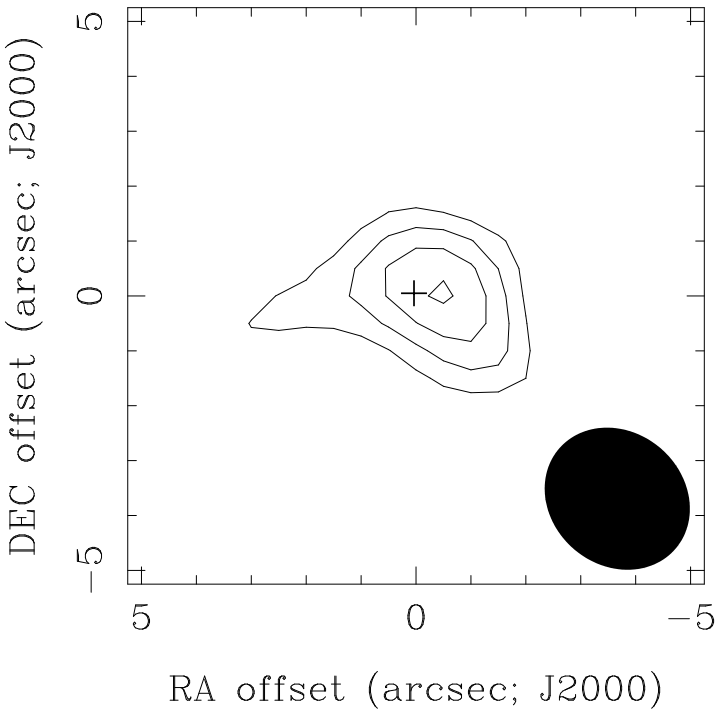

Figure 6.5 CARMA 3mm continuum image of DoAr 44

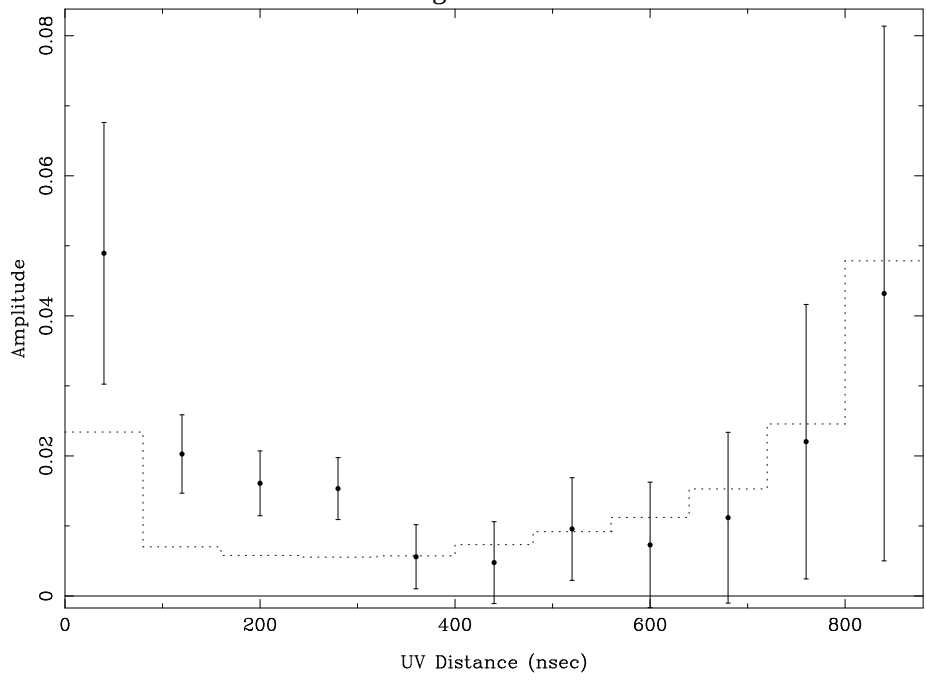

Figure 6.6 CARMA flux versus (u,v) plot of DoAr 44.

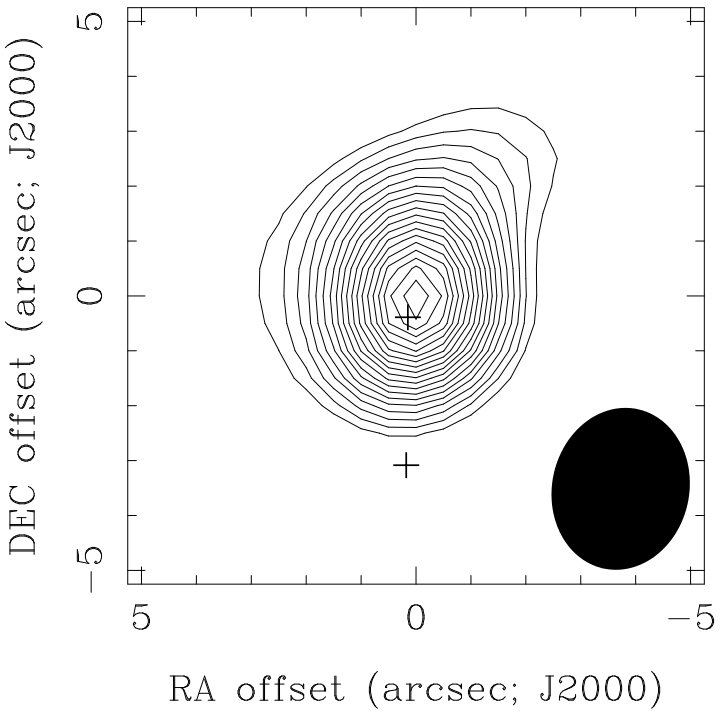

Figure 6.7 CARMA 1 mm continuum image of UX Tau.

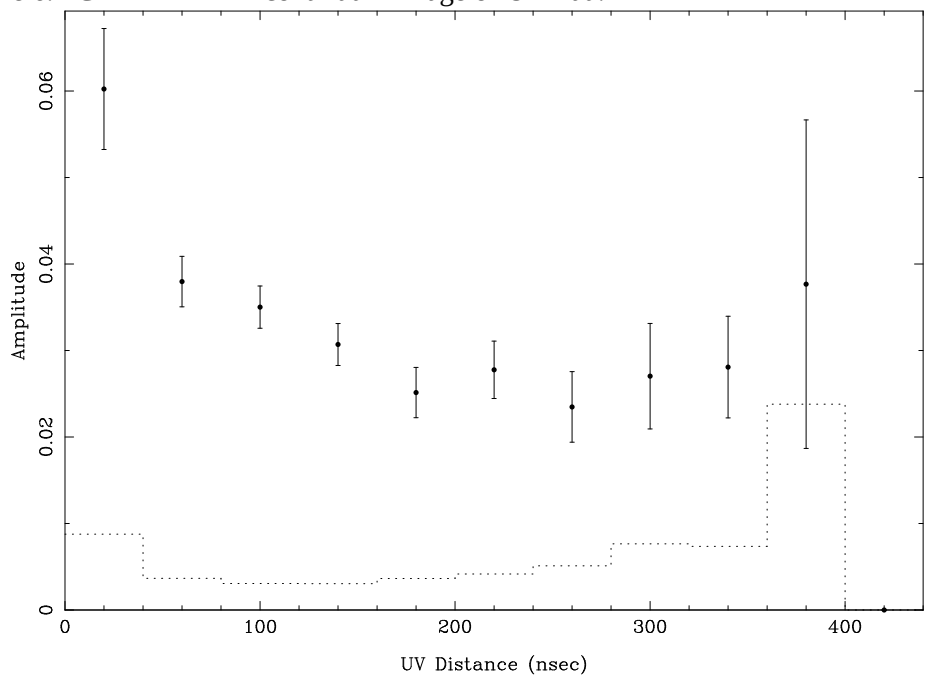

Figure 6.8 CARMA (u,v) plot of UX Tau.

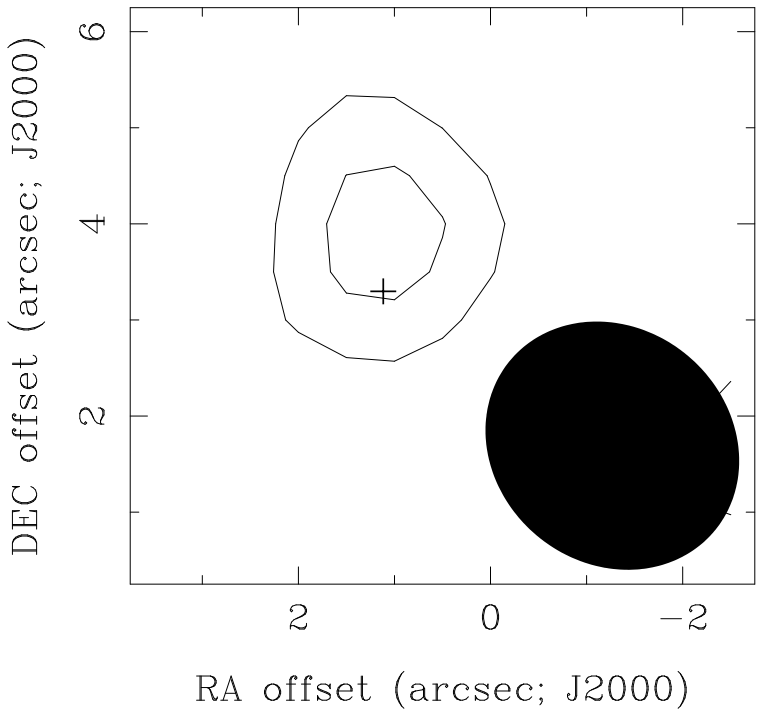

Figure 6.9 CARMA 1 mm continuum image of SR 21.

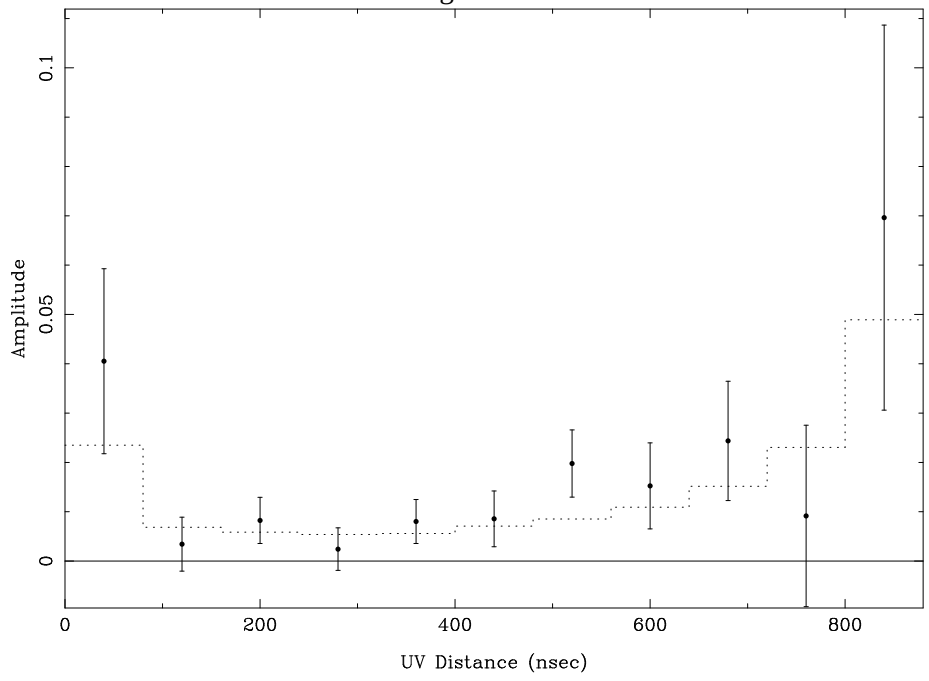

Figure 6.10 CARMA (u,v) plot of SR 21.

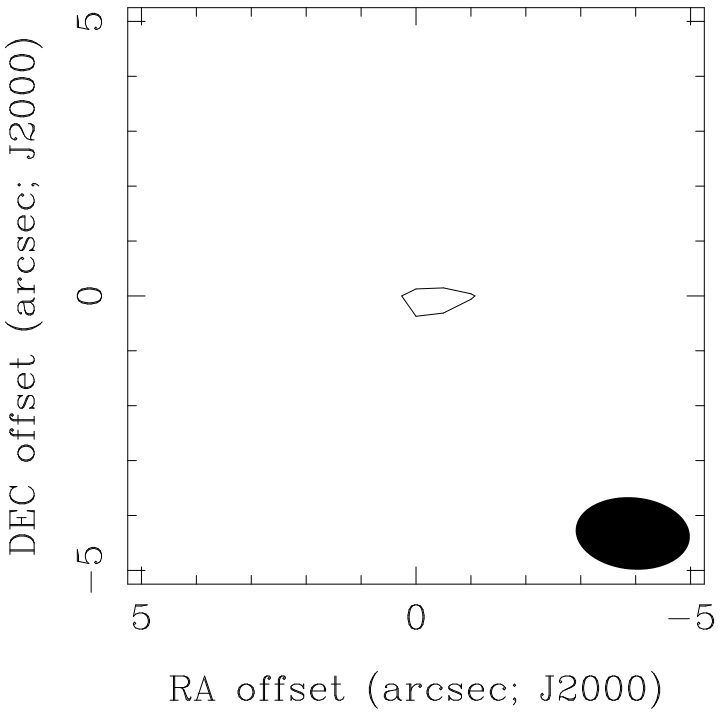

Figure 6.11 CARMA 1 mm continuum image of SSTc2d J033234.1+310056 .

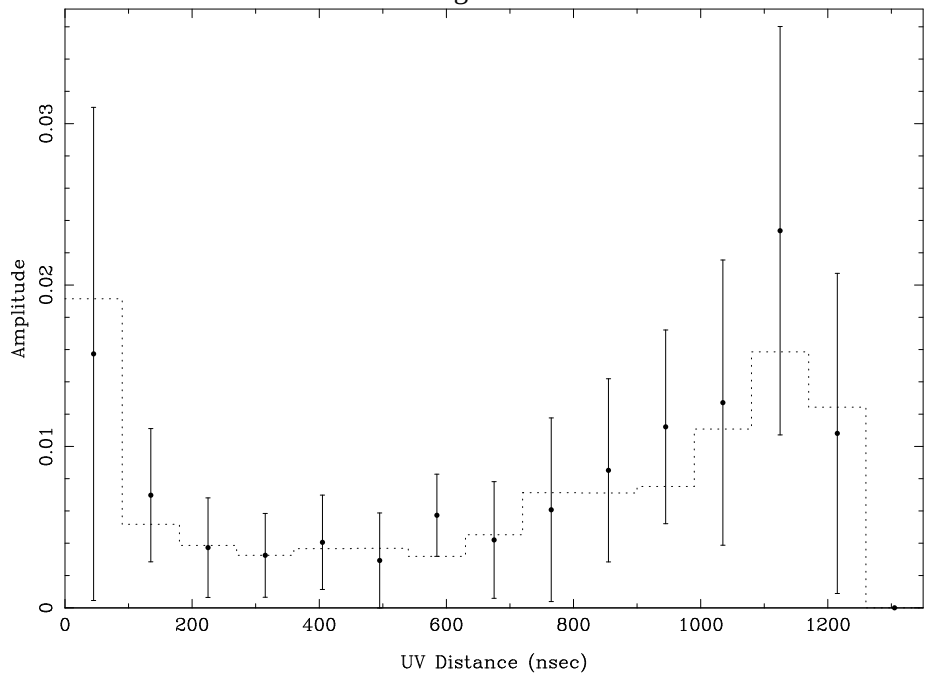

Figure 6.12 CARMA (u,v) plot of SSTc2d J033234.1+310056.

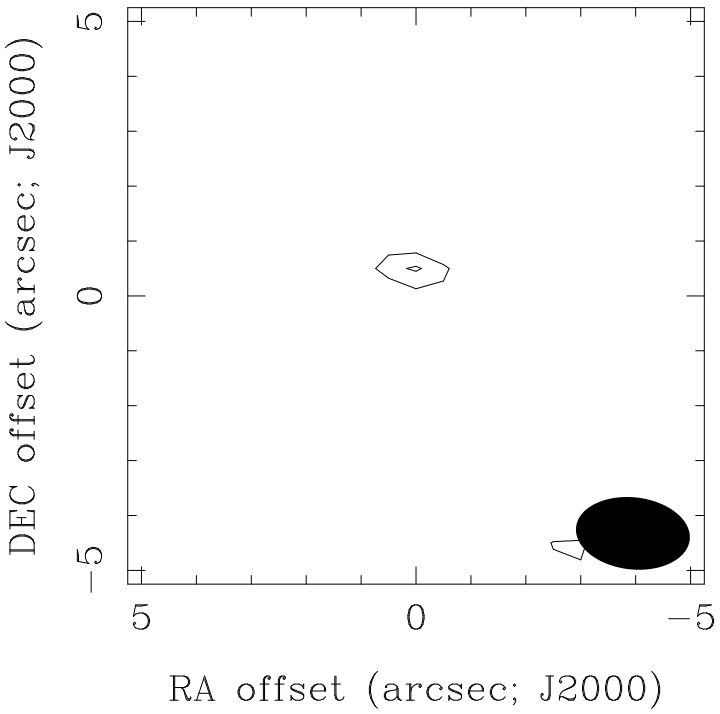

Figure 6.13 CARMA 1 mm continuum image of SSTc2d J032857.0+311622.

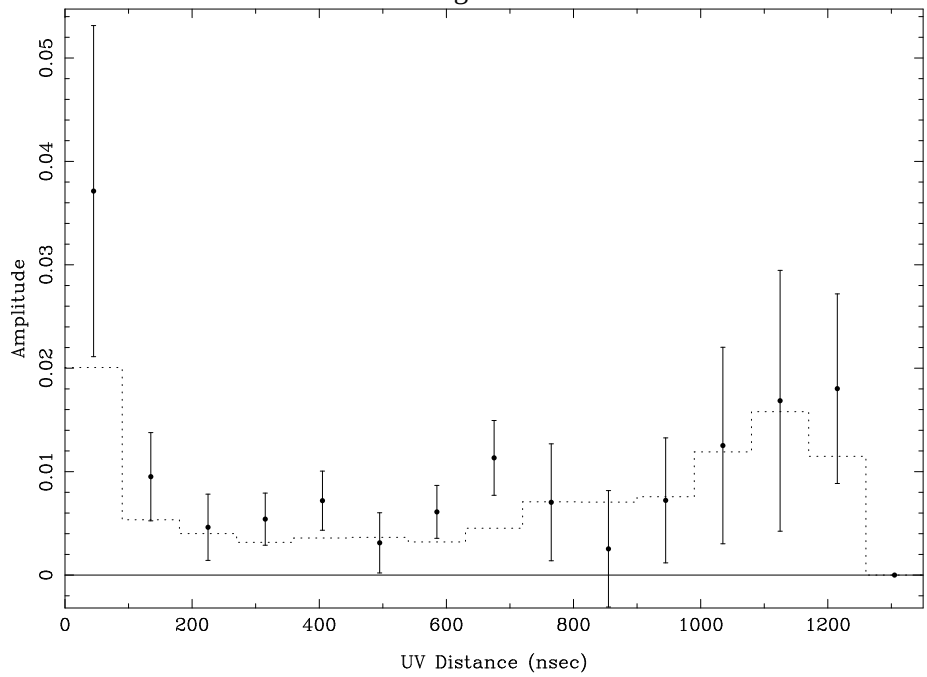

Figure 6.14 CARMA (u,v) plot of SSTc2d J032857.0+311622.

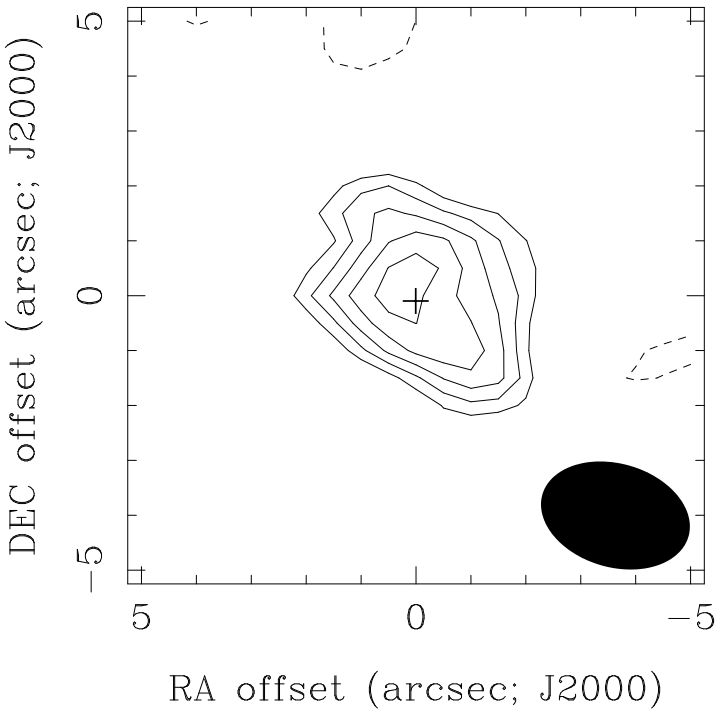

Figure 6.15 CARMA moment 0 map of the CO J=1-0 line from LkHα 330.

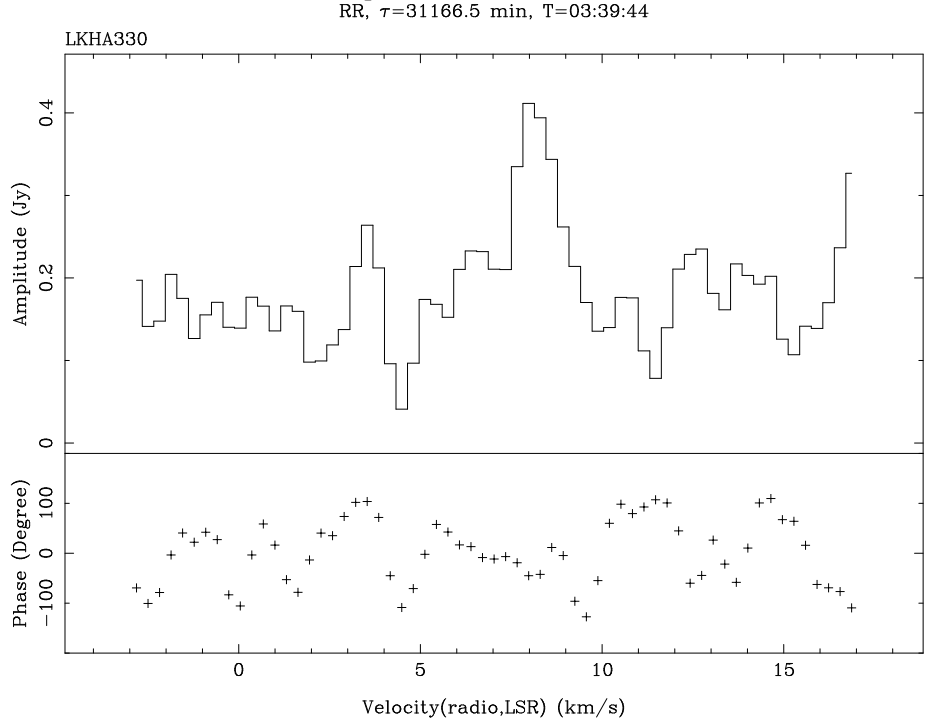

Figure 6.16 CARMA 8 MHz bandwidth spectrum of LkHα 330 with amplitude (top) and phase (bottom) against V_{LSR}.

Chapter 7

Conclusions

7.1 Summary of thesis

Circumstellar disks are ubiquitous around young stars. Over time, the disks dissipate revealing planets that formed hidden from astronomical observation by their natal dust. Since direct detection of young planets at the orbital distances probed by radial velocity surveys is only currently possible for transiting systems, other tracers of potential planet formation must be found. One sign of disk evolution, potentially linked to planet formation, is the opening of a gap or inner hole in the disk. In this thesis, I have identified and characterized a set of disks with inner holes. While it is clear that cold disks are not common, with only $\sim$5% of disks showing signs of inner holes, they provide proof that a least some disks evolve from the inside-out. These cold disks are unusual in that they have large gaps in the inner disk – the detected gaps are equivalent in our solar system to a lack of dust on size scales from inside the Earth's orbit out to Neptune's orbit or even the inner Kuiper belt. However, the central star in the object studied is often still accreting gas and a large outer disk remains, unlike in more evolved systems such as our own.

Using Spitzer, specifically data from the c2d Legacy Project, I identified and characterized four cold disks around F and G stars. A new diagnostic of the 30/13 μm ratio was used to distinguish these disks from the larger c2d sample. All four disks were modeled using a 2-D radiative transfer code with an introduced dust density reduction to simulate a gap. The SEDs fit the data well and gap radii of 20-45 AU were derived. All four disks required a small amount of material inside the gap to match the near-infrared fluxes in excess of the stellar photosphere.

Submillimeter interferometry provides a more direct method of observing inner disk holes with sufficiently long baselines, but only a few cold disks are bright enough to observe with current arrays. I observed three disks visible from the northern hemisphere, those around LkHα 330, HD

135344B and SR 21N, with the Submillimeter Array (SMA) atop Mauna Kea at 340 GHz (880 μm) and resolved the central holes using the most extended interferometer configuration. The direct imaging of the gaps is in good agreement with the transition radii derived from the SEDs. LkHα 330 in particular has a very steep gap edge which seems more consistent with gravitational perturbation rather than a more gradual process such as grain growth and settling. Unfortunately, submillimeter resolved imaging is limited to the largest hole sizes so no constraints can be placed on smaller holes with current instruments using this method.

Cold disks often have gas in the inner 1 AU, as traced by CO M-band emission studied with the NIRSPEC echelle spectrograph at the Keck II telescope. I compared a sample of 10 cold disks with 26 non-transitional disks. Rotational excitation temperatures, column densities and emitting radii were consistently derived using a simple isothermal slab model. CO was detected from 70 % of the cold disks. Disks with CO close to the star are unlikely to have evolved due to photoevaporation, which preferentially affects the gas. Correlations of the derived CO parameters with stellar characteristics were examined. All the disks, including the nontransitional disks, show correlations between emitting area and both stellar luminosity and dust sublimation radius, indicating that the region of CO emission is strongly linked to the dust sublimation radius. For the cold disks, the rotational temperatures are significantly lower, perhaps as a result of probing deeper into the disk than is possible in optically thick disks.

Unresolved submillimeter photometry shows properties of cold disks in agreement with the emerging picture that they represent systems with large central holes. The SED-identified cold disks show significantly steeper submillimeter colors ranging with a mean value of α of 2.37$\pm$0.46 compared to the general disk population that displays α = 2. This likely indicates that the cold disks are optically thin even at 350 and 450 μm, unlike their classical T Tauri star counterparts. In order for the cold disks to show this difference, they must have centrally cleared most $\sim$100 μm sized grains as well as the $\lesssim$10 μm sized grains visible in the mid-infrared through their silicate emission features.

CARMA was used to observe eight cold disks, principally at λ = 2.6 mm. Seven were detected in continuum emission, including two newly identified cold disks from the c2d Spitzer maps. The dust disk around UX Tau A was resolved, and a stellar companion is just beyond the measured extent of the disk. Only one, LkHα 330, was detected in the ^{12}CO J=1-0 rotational transition. In all likelihood, the many non-detections point to instrumental challenges associated with the commissioning phase of this powerful new instrument rather than a lack of cold gas in transitional disks.

The mm-wave CO emission from the LkHα 330 disk was resolved, and the derived inclination of 40° is in good agreement with that from the SMA submillimeter dust continuum observations.

It has become increasingly clear that, while cold disks look similar at a surface glance, different physical processes drive the evolution of different disks. For dust grain growth to be the dominant process, the SMA images show that grains must have reached almost centimeter sizes with limited amounts of small grains produced in the process. Of the disks studied in this thesis, SR 21 has the hole most consistent with formation by dust grain growth. The hole edge is gradual as seen in the SMA data, and the amount of small grains close to the star is small. Also, gas is still present inside the hole.

Photoevaporation remains a possible explanation only for the just under 50% of cold disks without CO v=1→0 emission seen with Keck NIRSPEC. CoKu Tau 4 with its low disk mass and accretion rate is a plausible candidate for a photoevaporated disk. DM Tau, from which CO gas has not been detected but which still has a high accretion rate inconsistent with photoevaporation, remains a mystery.

Companions, either stellar or planetary, remain a possibilty for all the disks. For disks with large holes, any companion must be at large radii to account for the 20-40 AU radii gaps, greatly increasing the likelihood that a larger mass companion would have been detected in previous surveys. LkHα 330 is one of the most promising disks for a gap formed by a planetary or brown dwarf companion due to its steep outer gap edge. However, more exhaustive searches for stellar companions around all these stars are needed. Substantial work, both observationally and theoretically, remains to be done to fully understand these unusual systems but new technology should lead to better understanding of planet formation over the next decade.

7.2 Future work

While CARMA is moving out of its initial commissioning phase, significant improvements remain to be installed within the next year. New receivers with greatly improved sensitivity will particularly aid line work. The new 3 mm receivers, based on SIS mixers developed for the Atacama Large Millimeter Array (ALMA), are currently being deployed, while the new dual polarization 1 mm receivers are under development. The correlator will be expanded to its full 8 GHz lower + upper sideband bandwidth by the fall of 2008. As well as improved continuum sensitivity, this will permit simultaneous observations of multiple molecular lines. New array configurations with baselines

extended to over 2 km will achieve SMA-like resolution but with much better image fidelity due to the larger number of antennas. These improvements will permit studies of asymmetries in cold disks to search for signs of gravitational perturbation. Ultimately, ALMA will be crucial for the future of this field. More cold disks are currently being found through large infrared surveys, but most are significantly fainter than my initial sample and follow-up with today's instruments is not possible. ALMA will have significantly improved sensitivity with its fifty 12 m antennas and nearly routine access to the submillimeter 450/350 μm windows at the Chajnantor site.

As a next step toward characterizing the dust properties in the cold disks discovered in this thesis, I have been granted VLA 7 mm observations of LkHα 330, LkCa 15, SR 21, and HD 135344. The goal is to obtain spatially-resolved 7mm images and hence use these VLA data and our existing mm data to understand the properties of larger grains in these disks. These long wavelength observations have the advantage of probing optically thin dust at all disk radii. As grain growth remains one explanation for the holes, spatially resolved multiwavelength millimeter observations are necessary to understand the physical processes causing the disk evolution. A question of particular interest is whether the asymmetries seen in the 850 μm SMA data will also be present in the 7 mm data.

New high resolution infrared spectrographs are also aiding in characterizing the gas in transitional disks and my postdoc position involves working primarily with CRIRES data. Both TEXES on Gemini and CRIRES on the VLT have spectral resolutions of R=100,000, which significantly improves the use of line profiles to localize the gas. For CRIRES, advances include not only higher spectral resolution but also placing the spectrograph behind a very stable adaptive optics system allowing high precision spectro-astrometry – a technique that permits direct measurement of disk gas emitting location and area.

Spitzer has collected reams of data in its five years in space. Significant work in finding and characterizing cold disks out of large scale mapping projects remains to be done. Future infrared space telescopes, such as the James Webb Space Telescope (JWST), will provide additional information on cold disks, which is largely unaccessible from the ground. Since SED-based searches for disk gaps are distance independent, as long as the star and disk are detectable at a range of wavelengths, JWST can probe the occurrence of cold disks in much more distant star forming regions to see if disk evolution is different in massive star forming clouds like Orion or Carina.

Bibliography

Acke, B., van den Ancker, M. E., & Dullemond, C. P. 2005, A&A, 436, 209

Alcalá, J. M., Covino, E., Franchini, M., Krautter, J., Terranegra, L., & Wichmann, R. 1993, A&A, 272, 225

Alcala, J. M., Krautter, J., Schmitt, J. H. M. M., Covino, E., Wichmann, R., & Mundt, R. 1995, A&AS, 114, 109

Alexander, R. D. & Armitage, P. J. 2007, MNRAS, 375, 500

Alexander, R. D., Clarke, C. J., & Pringle, J. E. 2006, MNRAS, 369, 229

Andre, P. & Montmerle, T. 1994, ApJ, 420, 837

Andrews, S. M. & Williams, J. P. 2005, ApJ, 631, 1134

—. 2007a, ArXiv e-prints, 708

—. 2007b, ApJ, 659, 705

Augereau, J. C., Lagrange, A. M., Mouillet, D., & Ménard, F. 2001, A&A, 365, 78

Aumann, H. H., Beichman, C. A., Gillett, F. C., de Jong, T., Houck, J. R., Low, F. J., Neugebauer, G., Walker, R. G., & Wesselius, P. R. 1984, ApJ, 278, L23

Bary, J. S., Weintraub, D. A., & Kastner, J. H. 2003, ApJ, 586, 1136

Beckwith, S. V. W. 1996, Nature, 383, 139

Beckwith, S. V. W. & Sargent, A. I. 1991, ApJ, 381, 250

Beckwith, S. V. W., Sargent, A. I., Chini, R. S., & Guesten, R. 1990, AJ, 99, 924

Benedict, G. F., McArthur, B. E., Forveille, T., Delfosse, X., Nelan, E., Butler, R. P., Spiesman, W., Marcy, G., Goldman, B., Perrier, C., Jefferys, W. H., & Mayor, M. 2002, ApJ, 581, L115

Benedict, G. F., McArthur, B. E., Gatewood, G., Nelan, E., Cochran, W. D., Hatzes, A., Endl, M., Wittenmyer, R., Baliunas, S. L., Walker, G. A. H., Yang, S., Kürster, M., Els, S., & Paulson, D. B. 2006, AJ, 132, 2206

Bertout, C., Siess, L., & Cabrit, S. 2007, A&A, 473, L21

Bjorkman, J. E. & Wood, K. 2001, ApJ, 554, 615

Blake, G. A. & Boogert, A. C. A. 2004, ApJ, 606, L73

Bodenheimer, P., Hubickyj, O., & Lissauer, J. J. 2000, Icarus, 143, 2

Boogert, A. C. A., Blake, G. A., & Tielens, A. G. G. M. 2002, ApJ, 577, 271

Boss, A. P. 2001, ApJ, 563, 367

Bouwman, J., de Koter, A., Dominik, C., & Waters, L. B. F. M. 2003, A&A, 401, 577

Brittain, S. D., Simon, T., Najita, J. R., & Rettig, T. W. 2007, ApJ, 659, 685

Brown, J. M., Blake, G. A., Dullemond, C. P., Merín, B., Augereau, J. C., Boogert, A. C. A., Evans, II, N. J., Geers, V. C., Lahuis, F., Kessler-Silacci, J. E., Pontoppidan, K. M., & van Dishoeck, E. F. 2007, ApJ, 664, L107

Bryden, G., Różyczka, M., Lin, D. N. C., & Bodenheimer, P. 2000, ApJ, 540, 1091

Calvet, N., D'Alessio, P., Hartmann, L., Wilner, D., Walsh, A., & Sitko, M. 2002, ApJ, 568, 1008

Calvet, N., D'Alessio, P., Watson, D. M., Franco-Hernández, R., Furlan, E., Green, J., Sutter, P. M., Forrest, W. J., Hartmann, L., Uchida, K. I., Keller, L. D., Sargent, B., Najita, J., Herter, T. L., Barry, D. J., & Hall, P. 2005, ApJ, 630, L185

Chiang, E. I. & Goldreich, P. 1997, ApJ, 490, 368

Clarke, C. J., Gendrin, A., & Sotomayor, M. 2001, MNRAS, 328, 485

Cohen, M. & Kuhi, L. V. 1979, ApJS, 41, 743

Corder, S., Eisner, J., & Sargent, A. 2005, ApJ, 622, L133

Correia, S., Zinnecker, H., Ratzka, T., & Sterzik, M. F. 2006, A&A, 459, 909

D'Alessio, P., Calvet, N., & Hartmann, L. 2001, ApJ, 553, 321

D'Alessio, P., Hartmann, L., Calvet, N., Franco-Hernández, R., Forrest, W. J., Sargent, B., Furlan, E., Uchida, K., Green, J. D., Watson, D. M., Chen, C. H., Kemper, F., Sloan, G. C., & Najita, J. 2005, ApJ, 621, 461

Dent, W. R. F., Greaves, J. S., & Coulson, I. M. 2005, MNRAS, 359, 663

Doucet, C., Pantin, E., Lagage, P. O., & Dullemond, C. P. 2006, A&A, 460, 117

Draine, B. T. 2003, ApJ, 598, 1017

—. 2006, ApJ, 636, 1114

Dullemond, C. P. & Dominik, C. 2004, A&A, 417, 159

—. 2005, A&A, 434, 971

Dunkin, S. K., Barlow, M. J., & Ryan, S. G. 1997, MNRAS, 286, 604

Durisen, R. H., Boss, A. P., Mayer, L., Nelson, A. F., Quinn, T., & Rice, W. K. M. 2007, in Protostars and Planets V, ed. B. Reipurth, D. Jewitt, & K. Keil, 607–622

Eisner, J. A., Hillenbrand, L. A., White, R. J., Bloom, J. S., Akeson, R. L., & Blake, C. H. 2007, ArXiv e-prints, 707

Enoch, M. L., Young, K. E., Glenn, J., Evans, II, N. J., Golwala, S., Sargent, A. I., Harvey, P., Aguirre, J., Goldin, A., Haig, D., Huard, T. L., Lange, A., Laurent, G., Maloney, P., Mauskopf, P., Rossinot, P., & Sayers, J. 2006, ApJ, 638, 293

Evans, II, N. J., Allen, L. E., Blake, G. A., Boogert, A. C. A., Bourke, T., Harvey, P. M., Kessler, J. E., Koerner, D. W., Lee, C. W., Mundy, L. G., Myers, P. C., Padgett, D. L., Pontoppidan, K., Sargent, A. I., Stapelfeldt, K. R., van Dishoeck, E. F., Young, C. H., & Young, K. E. 2003, PASP, 115, 965

Fernandez, M. & Eiroa, C. 1996, A&A, 310, 143

Fernandez, M., Ortiz, E., Eiroa, C., & Miranda, L. F. 1995, A&AS, 114, 439

Forrest, W. J., Sargent, B., Furlan, E., D'Alessio, P., Calvet, N., Hartmann, L., Uchida, K. I., Green, J. D., Watson, D. M., Chen, C. H., Kemper, F., Keller, L. D., Sloan, G. C., Herter, T. L., Brandl, B. R., Houck, J. R., Barry, D. J., Hall, P., Morris, P. W., Najita, J., & Myers, P. C. 2004, ApJS, 154, 443

Furlan, E., Hartmann, L., Calvet, N., D'Alessio, P., Franco-Hernández, R., Forrest, W. J., Watson, D. M., Uchida, K. I., Sargent, B., Green, J. D., Keller, L. D., & Herter, T. L. 2006, ApJS, 165, 568

Geers, V. C., Augereau, J.-C., Pontoppidan, K. M., Dullemond, C. P., Visser, R., Kessler-Silacci, J. E., Evans, II, N. J., van Dishoeck, E. F., Blake, G. A., Boogert, A. C. A., Brown, J. M., Lahuis, F., & Merín, B. 2006, A&A, 459, 545

Grady, C. A., Woodgate, B. E., Bowers, C. W., Gull, T. R., Sitko, M. L., Carpenter, W. J., Lynch, D. K., Russell, R. W., Perry, R. B., Williger, G. M., Roberge, A., Bouret, J.-C., & Sahu, M. 2005, ApJ, 630, 958

Gregorio-Hetem, J., Lepine, J. R. D., Quast, G. R., Torres, C. A. O., & de La Reza, R. 1992, AJ, 103, 549

Haisch, Jr., K. E., Lada, E. A., & Lada, C. J. 2001, ApJ, 553, L153

Henning, T., Pfau, W., Zinnecker, H., & Prusti, T. 1993, A&A, 276, 129

Henning, T. & Stognienko, R. 1996, A&A, 311, 291

Herczeg, G. J., Linsky, J. L., Walter, F. M., Gahm, G. F., & Johns-Krull, C. M. 2006, ApJS, 165, 256

Hildebrand, R. H. 1983, QJRAS, 24, 267

Hillenbrand, L. A. 2006, in STScI Symposium Series, Vol. 19, A Decade of Discovery: Planets Around Other Stars, ed. M. Livio

Houck, J. R., Roellig, T. L., van Cleve, J., Forrest, W. J., Herter, T., Lawrence, C. R., Matthews, K., Reitsema, H. J., Soifer, B. T., Watson, D. M., Weedman, D., Huisjen, M., Troeltzsch, J., Barry, D. J., Bernard-Salas, J., Blacken, C. E., Brandl, B. R., Charmandaris, V., Devost, D., Gull, G. E., Hall, P., Henderson, C. P., Higdon, S. J. U., Pirger, B. E., Schoenwald, J., Sloan, G. C., Uchida,

K. I., Appleton, P. N., Armus, L., Burgdorf, M. J., Fajardo-Acosta, S. B., Grillmair, C. J., Ingalls, J. G., Morris, P. W., & Teplitz, H. I. 2004, ApJS, 154, 18

Hughes, A. M., Wilner, D. J., Calvet, N., D'Alessio, P., Claussen, M. J., & Hogerheijde, M. R. 2007, ApJ, 664, 536

Jensen, E. L. N., Mathieu, R. D., Donar, A. X., & Dullighan, A. 2004, ApJ, 600, 789

Kenyon, S. J. & Bromley, B. C. 2004, AJ, 127, 513

Kessler-Silacci, J., Augereau, J.-C., Dullemond, C. P., Geers, V., Lahuis, F., Evans, II, N. J., van Dishoeck, E. F., Blake, G. A., Boogert, A. C. A., Brown, J., Jørgensen, J. K., Knez, C., & Pontoppidan, K. M. 2006, ApJ, 639, 275

Koerner, D. W., Sargent, A. I., & Beckwith, S. V. W. 1993, Icarus, 106, 2

Lada, C. J., Muench, A. A., Luhman, K. L., Allen, L., Hartmann, L., Megeath, T., Myers, P., Fazio, G., Wood, K., Muzerolle, J., Rieke, G., Siegler, N., & Young, E. 2006, AJ, 131, 1574

Lada, C. J. & Wilking, B. A. 1984, ApJ, 287, 610

Lahuis, F. 2006, Data Legacy of the "Cores to Disks" Spectroscopy Program

Lahuis, F., van Dishoeck, E. F., Blake, G. A., Evans, II, N. J., Kessler-Silacci, J. E., & Pontoppidan, K. M. 2007, ApJ, 665, 492

Liffman, K. 2003, Publications of the Astronomical Society of Australia, 20, 337

Lin, D. N. C., Bodenheimer, P., & Richardson, D. C. 1996, Nature, 380, 606

Lin, D. N. C. & Papaloizou, J. 1986, ApJ, 307, 395

Malfait, K., Bogaert, E., & Waelkens, C. 1998, A&A, 331, 211

Mannings, V. & Emerson, J. P. 1994, MNRAS, 267, 361

Marcy, G., Butler, R. P., Fischer, D., Vogt, S., Wright, J. T., Tinney, C. G., & Jones, H. R. A. 2005, Progress of Theoretical Physics Supplement, 158, 24

Marsh, K. A. & Mahoney, M. J. 1992, ApJ, 395, L115

Martin, E. L., Montmerle, T., Gregorio-Hetem, J., & Casanova, S. 1998, MNRAS, 300, 733

Mathis, J. S., Rumpl, W., & Nordsieck, K. H. 1977, ApJ, 217, 425

Matsumura, S. & Pudritz, R. E. 2005, ApJ, 618, L137

McArthur, B. E., Endl, M., Cochran, W. D., Benedict, G. F., Fischer, D. A., Marcy, G. W., Butler, R. P., Naef, D., Mayor, M., Queloz, D., Udry, S., & Harrison, T. E. 2004, ApJ, 614, L81

McCabe, C., Ghez, A. M., Prato, L., Duchêne, G., Fisher, R. S., & Telesco, C. 2006, ApJ, 636, 932

McLean, I. S., Becklin, E. E., Bendiksen, O., Brims, G., Canfield, J., Figer, D. F., Graham, J. R., Hare, J., Lacayanga, F., Larkin, J. E., Larson, S. B., Levenson, N., Magnone, N., Teplitz, H., & Wong, W. 1998, in Presented at the Society of Photo-Optical Instrumentation Engineers (SPIE) Conference, Vol. 3354, Proc. SPIE Vol. 3354, p. 566-578, Infrared Astronomical Instrumentation, Albert M. Fowler; Ed., ed. A. M. Fowler, 566–578

Mundy, L. G., Looney, L. W., & Welch, W. J. 2000, Protostars and Planets IV, 355

Najita, J., Carr, J. S., & Mathieu, R. D. 2003, ApJ, 589, 931

Najita, J. R., Strom, S. E., & Muzerolle, J. 2007, MNRAS, 378, 369

Osterloh, M. & Beckwith, S. V. W. 1995, ApJ, 439, 288

Pascucci, I., Wolf, S., Steinacker, J., Dullemond, C. P., Henning, T., Niccolini, G., Woitke, P., & Lopez, B. 2004, A&A, 417, 793

Pickett, H. M., Poynter, I. R. L., Cohen, E. A., Delitsky, M. L., Pearson, J. C., & Muller, H. S. P. 1998, Journal of Quantitative Spectroscopy and Radiative Transfer, 60, 883

Piétu, V., Dutrey, A., Guilloteau, S., Chapillon, E., & Pety, J. 2006, A&A, 460, L43

Pollack, J. B., Hollenbach, D., Beckwith, S., Simonelli, D. P., Roush, T., & Fong, W. 1994, ApJ, 421, 615

Pollack, J. B., Hubickyj, O., Bodenheimer, P., Lissauer, J. J., Podolak, M., & Greenzweig, Y. 1996, Icarus, 124, 62

Prato, L., Greene, T. P., & Simon, M. 2003, ApJ, 584, 853

Qi, C., Kessler, J. E., Koerner, D. W., Sargent, A. I., & Blake, G. A. 2003, ApJ, 597, 986

Rafikov, R. R. 2004, AJ, 128, 1348

Rettig, T. W., Haywood, J., Simon, T., Brittain, S. D., & Gibb, E. 2004, ApJ, 616, L163

Rice, W. K. M., Armitage, P. J., Wood, K., & Lodato, G. 2006, MNRAS, 373, 1619

Richter, M. J., Jaffe, D. T., Blake, G. A., & Lacy, J. H. 2002, ApJ, 572, L161

Rieke, G. H., Su, K. Y. L., Stansberry, J. A., Trilling, D., Bryden, G., Muzerolle, J., White, B., Gorlova, N., Young, E. T., Beichman, C. A., Stapelfeldt, K. R., & Hines, D. C. 2005, ApJ, 620, 1010

Robitaille, T. P., Whitney, B. A., Indebetouw, R., & Wood, K. 2007, ApJS, 169, 328

Rodmann, J., Henning, T., Chandler, C. J., Mundy, L. G., & Wilner, D. J. 2006, A&A, 446, 211

Rothman, L. S., Jacquemart, D., Barbe, A., Benner, D. C., Birk, M., Brown, L. R., Carleer, M. R., Chackerian, C., Chance, K., Coudert, L. H., Dana, V., Devi, V. M., Flaud, J. M., Gamache, R. R., Goldman, A., Hartmann, J. M., Jucks, K. W., Maki, A. G., Mandin, J. Y., Massie, S. T., Orphal, J., Perrin, A., Rinsland, C. P., Smith, M. A. H., Tennyson, J., Tolchenov, R. N., Toth, R. A., Vander Auwera, J., Varanasi, P., & Wagner, G. 2005, Journal of Quantitative Spectroscopy and Radiative Transfer, 96, 139

Sako, S., Yamashita, T., Kataza, H., Miyata, T., Okamoto, Y. K., Honda, M., Fujiyoshi, T., & Onaka, T. 2005, ApJ, 620, 347

Salyk, C., Blake, G. A., Boogert, A. C. A., & Brown, J. M. 2007, ApJ, 655, L105

Sargent, A. I. & Beckwith, S. 1987, ApJ, 323, 294

Sault, R. J., Teuben, P. J., & Wright, M. C. H. 1995, in Astronomical Society of the Pacific Conference Series, Vol. 77, Astronomical Data Analysis Software and Systems IV, ed. R. A. Shaw, H. E. Payne, & J. J. E. Hayes, 433–+

Scoville, N. Z., Sargent, A. I., Sanders, D. B., Claussen, M. J., Masson, C. R., Lo, K. Y., & Phillips, T. G. 1986, ApJ, 303, 416

Siess, L., Dufour, E., & Forestini, M. 2000, A&A, 358, 593

Strom, K. M., Strom, S. E., Edwards, S., Cabrit, S., & Skrutskie, M. F. 1989, AJ, 97, 1451

Strom, S. E., Strom, K. A., & Carrasco, L. 1974, PASP, 86, 798

Takeuchi, T., Clarke, C. J., & Lin, D. N. C. 2005, ApJ, 627, 286

Tanaka, H., Himeno, Y., & Ida, S. 2005, ApJ, 625, 414

Thi, W. F., van Dishoeck, E. F., Blake, G. A., van Zadelhoff, G. J., Horn, J., Becklin, E. E., Mannings, V., Sargent, A. I., van den Ancker, M. E., Natta, A., & Kessler, J. 2001, ApJ, 561, 1074

Throop, H. B. & Bally, J. 2005, ApJ, 623, L149

Udalski, A., Paczynski, B., Zebrun, K., Szymanski, M., Kubiak, M., Soszynski, I., Szewczyk, O., Wyrzykowski, L., & Pietrzynski, G. 2002, Acta Astronomica, 52, 1

Udry, S. & Santos, N. C. 2007, ARA&A, 45, 397

van den Ancker, M. E., The, P. S., Tjin A Djie, H. R. E., Catala, C., de Winter, D., Blondel, P. F. C., & Waters, L. B. F. M. 1997, A&A, 324, L33

Varnière, P., Blackman, E. G., Frank, A., & Quillen, A. C. 2006, ApJ, 640, 1110

Waelkens, C., Bogaert, E., & Waters, L. B. F. M. 1994, in ASP Conf. Ser. 62: The Nature and Evolutionary Status of Herbig Ae/Be Stars, ed. P. S. The, M. R. Perez, & E. P. J. van den Heuvel, 405

Walker, M. F. 1972, ApJ, 175, 89

Weidenschilling, S. J. 1977, Ap&SS, 51, 153

White, R. J. & Ghez, A. M. 2001, ApJ, 556, 265

Whittet, D. C. B., Prusti, T., Franco, G. A. P., Gerakines, P. A., Kilkenny, D., Larson, K. A., & Wesselius, P. R. 1997, A&A, 327, 1194

Wichmann, R., Bastian, U., Krautter, J., Jankovics, I., & Rucinski, S. M. 1998, MNRAS, 301, L39+

Wright, E. L. 1987, ApJ, 320, 818

Zuckerman, B. & Song, I. 2004, ARA&A, 42, 685